UNIVERSITY OF SOUTHERN QUEENSLAND
AUSTRALIA

ACTIVE CONTROL OF FLOW SEPARATION USING COMPRESSED AIR EGRESS AND INGRESS FOR LOW-SPEED WIND TURBINE BLADES

A Thesis submitted by

Nazar Muneam Mahmood Aldabash

BSc, MSc

For the award of

Doctor of Philosophy

2020

ABSTRACT

Wind energy is one of the most promising alternative energy sources for the continuously increasing demand for worlds' energy consumption. In recent decades, there has been a steady and growing demand for energy, which has led to a shift to renewable resources. During many decades the wind turbine design, in particular, wind turbine blade design has been intensively researched to extract maximum possible energy from the wider range of wind flows. However, there have been many unresolved problems in the performance of small wind turbine blades due to insufficient energy generation at low-velocity wind regimes. Therefore, this project will investigate methods to improve the performance of small horizontal axis wind turbines (sHAWT) operating in low wind speed sites.

The primary cause for the reduction in energy generation at low wind velocity regimes was identified as the flow separation. In this project, suction and blowing techniques were used as active flow controls (AFC) to reduce flow separation in order to overcome the effect of an adverse pressure gradient (APG) and thus improve aerofoil performance. The data for a sHAWT with a 10 m diameter and a capacity of 25 kW were adopted. Two types of aerofoils were used, S823 and S822 aerofoils. Lift and drag coefficients were obtained with/without AFC technology. The range of tested angles of attack was between 0 and 21° and therefore considered suitable for predicting turbine performance. Suction speeds were changed to improve aerofoil performance, with -5 and -35 m/s suction speeds determined for low (less than 9°) and high (at least 9°) angles of attack respectively.

The research concluded that the deterioration of aerodynamic properties occurs at an AoA of 18°. It was also found that applying suction at 18% of the chord length on the upper surface gave good results at all angles of attack. The use of a boundary layer suction method delays the flow separation from the upper surface of the blade's aerofoil and even prevents separation for all but the highest angles of attack. The purpose of this method is to reduce the momentum flow in the high-pressure areas of the suction surface of the aerofoil. Although the use of such technologies may improve the performance of wind turbines, many challenges (such as design, maintenance and

construction costs) must be met to reduce or mitigate the occurrence of separation in the boundary layer.

Moreover, the research found that the enhanced sHAWT operated very efficiently at a rotational speed of 60 and 110 rpm with lower/ higher wind speeds than 9 m/s respectively. The rates of improvement were variable with each wind speed, so the average rate of improvement was 15% as a result of using the early suction (S1) technique. The research also demonstrated that the annual energy production for a site with an average annual wind speed of 6 m/s is 22% higher compared to the selected standard wind turbines.

CERTIFICATION OF THESIS

This thesis is entirely the work of Nazar Muneam Mahmood Aldabash except where otherwise acknowledged. The work is original and has not previously been submitted for any other award, except where acknowledged.

Principal Supervisor: Assoc Prof Jayantha Epaarachchi

Associate Supervisor: Assoc Prof Andrew Wandel

Associate Supervisor: Professor Peter Schubel

Student and supervisors signatures of endorsement are held at the University.

ACKNOWLEDGEMENT

IN THE NAME OF ALLAH, THE MOST BENEFICENT, THE MOST MERCIFUL

First and foremost, I would like to thank Allah for his blessing, kindness and for giving me good health, courage, knowledge and strength to finish my doctorate.

I should like to thank the many people who made this thesis possible. I would like to express my sincere thanks and gratitude to my principal supervisor, Associate Professor Jayantha Epaarachchi. For his continued support and encouragement during my PhD journey, Dr Jay has been a father-like figure and advisor to me. His support extended beyond my academic endeavours. He helped me to overcome many difficulties and problems during the research journey.

I would also like to extend my sincere appreciation and gratitude to my Associate supervisor, Associate Professor Andrew Wandel. He helped me through his valuable feedback and comments. Dr Andrew has extended my thinking in many directions while at the same time helping me to stay on, or at least near to, the path of my thesis journey. I am also grateful to him for giving me the opportunity to work on this research project which has helped me to broaden my knowledge and develop new skills.

Thanks also to my Associate supervisor, Professor Peter Schubel (the executive director of the institute for advanced engineering and space sciences (IAESS) and director of the centre for future materials (CFM)) for his encouragement and thoughtful opinions on my study issues. I extend my thanks for his valuable comments and suggestions towards the experimental part of my study.

I would like to recognize the encouragement given by my teachers, friends, and colleagues: Professor Julio Soria (Monash University), Professor Talal Yusaf, Dr Shahab Abdulla, Professor Abdul Salam Darwish (University of Bolton), Dr Ikhlase M. Fayed (University of Technology), Dr Rajab Abousnina, Dr Ahmed Razzaq Hasan Al-Manea, Dr Bilal Hamid Abdul-Jabbar, Dr Raed N. Al-Rbaihat, Dr Sartip

The commitment of four years allowed me to extend myself professionally and personally. It involved a serious commitment that allowed me to deal with complex issues and to journey towards a new adventure.

TABLE OF CONTENTS

LIST OF FIGURES

LIST OF TABLES

NOTATION, GREEK SYMBOLS, ACRONYMS, AND ABBREVIATIONS

Notation

E_o Annual Energy Production (kWh)

A_{rotor} Area of the rotor blade (m^2)

C_L Lift coefficient

C_D Drag coefficient

V_r Rated wind speed

C_p Power coefficient

V_1 Available wind speeds

P_w Available wind power (kW)

D Rotor diameter (m)

P_T Actual wind power (kW)

R the radius of the WT rotor (m)

N Number of blade rotation (rpm)

F_A Axial force

a	Axial speed induction factor
a'	Tangential speed interference factor
B	Number of rotor blades
W	Relative wind speed
x/c	The ratio of position in the direction of the chord to the chord length
P	Power of wind turbine
P_r	Rated power
CP	Pressure coefficient-
C_w	Scale factor
K_w	Shape factor
B1	Blowing process at slot number one
B3	Blowing process at slot number three
B2	Blowing process at slot number two
S1	Suction process at slot number one
S2	Suction process at slot number two
S3	Suction process at slot number three

C   Chord length

V_o Cut off wind speed

V_i Cut-in wind speed

C_{LD} Design lift coefficient

m_r Local torque coefficient

C_T Momentum coefficient

P_t Stagnation or total pressure in pitot tube technology

P_s Static pressure in pitot tube technology

Re_θ the momentum-thickness equation

C_f the skin friction coefficient

Greek symbols

λ Tip speed ratio

ρ Air density (kg/m^3)

Ω rotor angular velocity (rad/s)

α Angle of attack

α_{opt} The optimum angle of attack

η_p Prandtl relation

ε Rate of dissipation of turbulence

ϕ Relative flow angle deg.

α_0 Zero lift angle of attack

ϕ_d Design relative angle

υ Kinematic viscosity

μ Dynamic viscosity

λ_{rd} Local design tip speed ratio

σ Local solidity

λr Local tip speed ratio

k Turbulent kinetic energy

λ Tip speed ratio

ω specific dissipation rate

γ the intermittency factor

Acronyms & Abbreviations

CFD   Computational fluid dynamics

HAWT   Horizontal axis wind turbine

VAWT   Vertical axis wind turbine

sHAWT   Small Horizontal axis wind turbine

WT   Wind turbine

rpm   Revolution per minute

APG   Adverse pressure gradient

NREL   National Renewable Energy Laboratory

BET   Blade element theory

BEM   blade element momentum

TSR   Tip speed ratio

NACA   National Advisory Committee for Aeronautics

NASA   National Aeronautics and Space Administration

AoA   Angle of attack (°)

Re   Reynolds number

PIV	Particle image velocimetry
MEMS	Micro Electro Mechanical System
LSB	Laminar separation bubble
SST	Shear Stress Transport
RNG	Renormalization Group
IDDES	Improved Delayed Detached Eddy Simulation
FW-H	Ffowcs Williams and Hawkings
sWT	Small wind turbine
IR	Infrared thermography
ZMF	zero-mass-flux
LE	Leading-edge
TE	Trailing edge
TES	trailing-edge separation
RANS	Reynolds-Averaged Navier-Stokes
URANS	Unsteady Reynolds-Averaged Navier – Stokes
GA	Genetic Algorithm

ANSYS	An acronym to analysis system
BLT	Boundary layer transition
BOM	Bureau of meteorology
CF	Capacity factor
SERI	Solar Energy Research Institute
SA	Spalart-Allmaras model
VAC	Volts (electrical pressure) of alternating current (AC)
P_t	Stagnation or total pressure in pitot tube technology
P_s	Static pressure in pitot tube technology
F_T	Tangential force
C_A	Thrust coefficient
Q	Torque [n]
C_q	Torque coefficient
k	Turbulent kinetic energy
V_1	Undisturbed or available wind speed
T-S	Tollmien-Schlichting

DNS   Direct Numerical Simulation

LES   Large Eddy Simulation

PSE   parabolized stability equations

SP   flow separation point

CHAPTER 1: INTRODUCTION

1.1 Background

The use of traditional, fossil fuel resources such as coal and natural gas, has contributed to the advancement of human civilization, helping the world to grow and prosper. Despite this, there is an ongoing and growing concern about the negative environmental impact of using these traditional resources solely. The use of coal and fossil fuels has contributed significantly to the global emission of carbon dioxide and greenhouse gas (Darwish et al., 2019). Reducing the use of these traditional energies and moving towards renewable sources of energy has become imperative, especially in developing countries (Cheng and Zhu, 2014). Wind energy is clean and environmentally friendly. In addition to reducing the use of traditional energy sources, it has also developed very rapidly in recent decades (Walker, 2015). Although their growth may cause potential environmental impacts as a result of building and operating wind turbines, wind energy is low in cost compared to other conventional energy sources (Maeda and Watts, 2019) and may become a more significant source of energy shortly (Guidolin and Alpcan, 2019); (Bahrami et al., 2019). The idea of extracting energy from the wind is one of the oldest strategies, which has been used throughout the ages (Sørensen, 2011). Wind power is the fastest-growing energy in the world (Flavin, 1999). Additionally, wind power production grew to 651 GW in 2019 (GWEC, 2019) (Figure 1-1).

In Australia, sustainable energy generation has been facilitated by a set of measures that will help scientists develop new technologies through the use of renewable energy resources. Li et al. (2020) noted that the Australian government had set a massive target of 27% of Australia's renewable electrical power needs being met by the year 2030. Moreover, 6% of Australian electricity generation is currently produced from wind energy, while 86.3% is derived from fossil energy sources (especially coal), which is a significant contributor to the nation's emissions of greenhouse gases.

Historic development of total installations (onshore and offshore)

- Onshore
- Offshore

CAGR +12%

CAGR +17%

CAGR +26%

	2001	2002	2003	2004	2005	2006	2007	2008	2009	2010	2011	2012	2013	2014	2015	2016	2017	2018	2019
Total	24	31	39	48	59	74	94	121	159	198	238	283	319	370	433	488	540	591	651
Offshore	0	0	-1	-1	-1	-1	1	1	2	3	4	5	7	8	12	14	19	23	29
Onshore	24	31	39	47	58	73	93	119	157	195	234	278	312	362	421	473	522	568	621

Share of offshore ~1%   ~2%   3%   4.5%

Detailed data sheet available in GWEC's Members Area

Source: GWEC Market Intelligence, March 2020

Figure 1-1: Wind Energy growth in recent decades (GWEC, 2019)

Wind is generated due to the difference in pressure between two regions as these areas are heated at different rates by solar radiation. Wind energy systems are usually found in remote or rural areas. Wind energy increases with increasing height and increases in open areas without obstacles.

1.2 Wind energy benefits and challenges

Wind energy is clean energy which does not require fuel. That is, wind energy does not lead to environmental pollution, as is the case with traditional coal-fired sources. It does not produce toxic waste as nuclear plants do. In terms of cost, it is cheaper to produce than solar technology.

On the one hand, a half-meter wind turbine blade can be used to charge a battery, or power lighting or telecommunications equipment remotely. On the other hand, large scale wind turbines may generate up to 15-20 MW, as shown in Figure 1-4 and are used in electrical power generation. (Busby, 2012).

2

However, the challenges facing wind-derived energy are enormous, as building a wind farm requires considerable capital. Moreover, if wind energy conversion systems are established in remote areas, this may require the transmission of electrical energy over vast distances, which results in the loss of some energy. Wind farms may need to be accessible by road to allow access by maintenance trucks and cranes. Despite all these challenges, the use of small turbines in the low-speed areas may solve many of these problems. (Busby, 2012).

1.3 Low wind speed sites and small wind turbine

In order to generate more energy, a larger scale wind turbine is required. In the last decade, a large wind turbine was developed which could generate up to 7 MW. However, small wind energy conversion systems are only able to generate power of 30-300 kW. (Darwish et al., 2019). Small wind energy conversion systems are suitable for low wind speed sites, but their performance is usually low due to the occurrence of the phenomenon of laminar separation bubble on wind turbine blades (Singh and Ahmed, 2013). In areas of low wind speed, appropriate blades must be produced to work more efficiently, in order to improve performance. (Ali, 2014).

1.4 Wind turbine category

Wind turbines are classified into several categories, as shown in Figure 1-2. They can also be categorized according to their axes into either vertical axis wind turbines (VAWT) or horizontal axis wind turbines (HAWT) (Figure 1-3). In horizontal axis wind turbines, the axis of rotation is parallel to the surface of the earth and the direction of airflow through it. As for the vertical axis wind turbines, they are structured perpendicular to the surface of the earth and the direction of airflow through them. There are two types of Horizontal axis turbines-upwind & downwind. Each has twisted blades along their length, attached to one side of the rotor hub.

Conversely, in the vertical type, the blades are connected to the rotational axis on both sides. The power system in the horizontal type is at the top of the turbine tower, while in the vertical type, it is at ground level. HAWT allows its blade to be rotated in the

direction of the wind, whereas in the vertical type (VAWT) this is not the case because it receives wind from any direction. In the horizontal type, the rotor may be located either in front of the tower or behind it. Vertical type turbines, however, do not exhibit this feature.

HAWT and VAWT can be categorized according to their rotational speed, into either slow or fast running wind turbines. Low-speed turbines offer several advantages over their high-speed counterparts, including low rotational speeds, the capacity to use a large number of blades (12-24 blades is not unusual), which therefore cover a large proportion of the windswept surface area, a diameter range of between 5-8 metres and relatively high starting torques. The disadvantage of these turbines is that they generate low power because the mean wind speed (according to reliable weather data for that locality) ranges from between 3-7 m/s. in addition to the weight of the rotors being heavy. Therefore, it is challenging to create turbines of this type with diameters exceeding 10 m/s. This type is commonly used to pump water. As for fast running wind turbines, the number of blades utilized is limited to 2-4 blades. They are lighter yet generate equivalent amounts of mechanical Power.

Figure 1-4 shows the increase in wind turbine sizes during the period from 1980 to 2020. Wind turbines can be categorized not only by size but also by their aerodynamic function, in other words, the blade's ability to create lift or drag, regardless of whether the power transformer catches its power from the aerodynamic drag or whether it can utilize the aerodynamic lift as shown in Figure 1-3 and Figure 1-5.
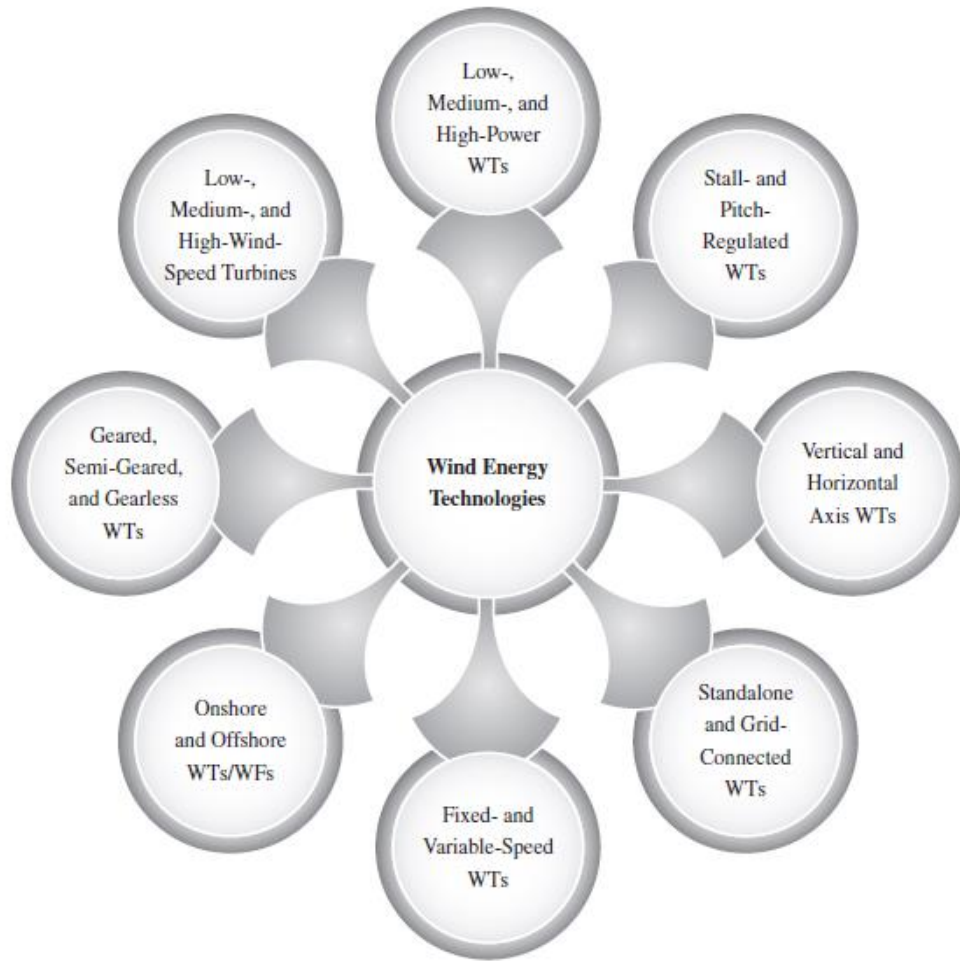
Figure 1-2: Wind energy categories (Yaramasu, 2016)
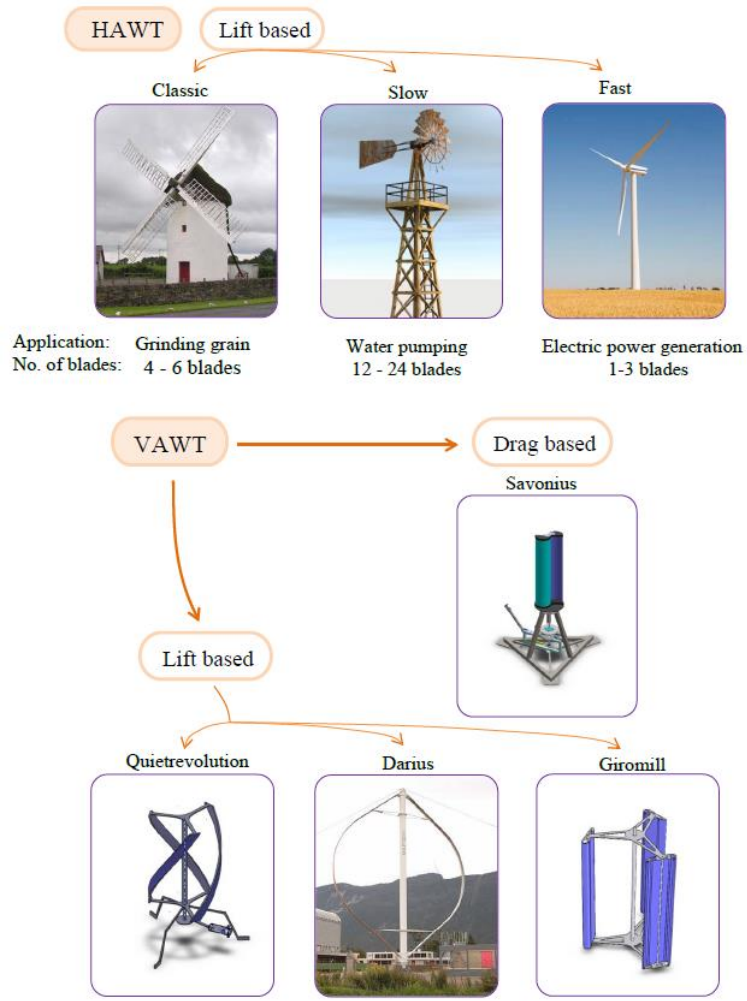
Figure 1-3: Types of wind turbine (Shkara, 2014)
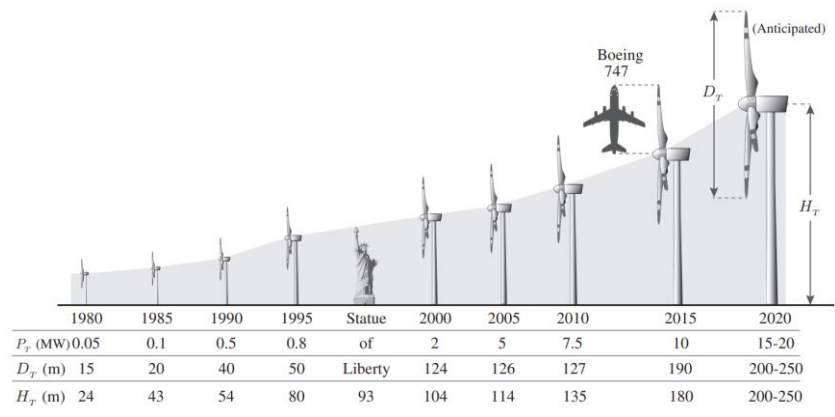
Figure 1-4: Evolution in wind turbine size (P_T, rated turbine output power; D_T, turbine rotor diameter; H_T , hub height) (Yaramasu, 2016)
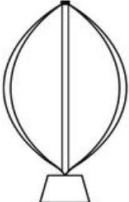
Figure 1-5: Classification of a wind turbine according to the force type of the blade
(Yan, 2020)

1.5 HAWT components

The major part of the wind turbine is the rotor, which is consisting of a hub with blades. Most horizontal axis wind turbines consist of three blades. Wind energy increases with the diameter of the turbine, as the rotor sweep area (A_{rotor}) increases. The full rotor assembly (Figure 1-61-2) is located at the top of the wind turbine and its direction changes according to the wind direction through the wind direction sensors. In other words, a sensor in the HAWT tail provides information to the wind turbine system to make it rotates in the wind direction using the yaw system. At high speeds, the turbines stop to prevent damages to the blades. The higher the wind speed, the more energy is generated because the power generated is proportional to the cube of the wind speed. In the event of an emergency, maintenance engineers obtain immediate information from the control systems responsible for monitoring operating conditions, such as rotor speed, blade angle and power output. The sensor network for the computer provides accurate data every ten minutes for each parameter, as a vital back-up system. (Busby, 2012).
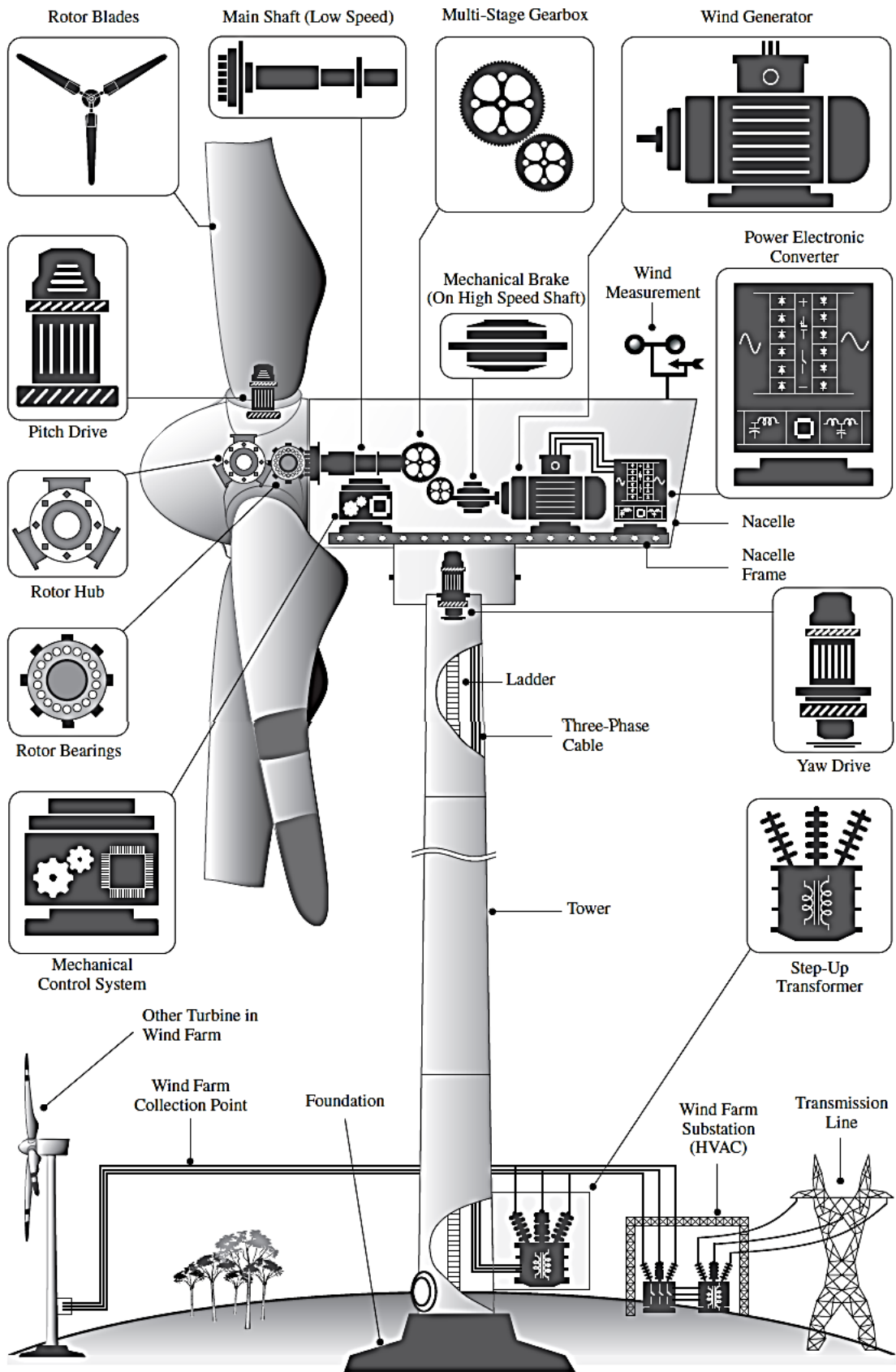
Figure 1-6: Schematic of wind turbine components (Yaramasu, 2016)

The horizontal axis wind turbine consists of several parts. The rotor hub is installed on the main shift known as the low-speed shaft. The blades transfer the kinetic energy into mechanical energy through the drive group, consisting of shafts, bearings, and gearbox. This mechanical energy is then converted into electrical energy by the generator, before being directed to the electrical network via a power converter system. Other systems are not involved in the energy conversion process but remain of great importance to the proper and effective operation of each turbine. These systems are wind speed sensors, power distribution cables, heat dissipation and lightning protection systems. Back-up power systems are also installed to operate the control systems, pitch drive and brakes. (Bin et al., 2011).

1.6 Wind Turbine Theory

The primary function of the wind turbine rotor is the exploitation of kinetic energy from the wind (Murty, 2017). The process of producing mechanical energy after its conversion from kinetic energy is achieved within an air tube that passes through the swept area of the wind turbine rotor (Sun et al., 2016). When a mass of air passes through the wind turbine rotor, which is like an air tube Figure 1-7, the area of the air tube expands, causing an increase in pressure to its maximum value accompanied by a decrease in wind velocity as it approaches the turbine rotor. In this process, a portion of the kinetic energy will be converted into latent power. Immediately behind the rotor, the pressure of the air mass that passes through the turbine will drop to its lowest value (below atmospheric pressure). Directly behind the wind turbine, there is still an amount of kinetic energy that will turn into potential energy to restore air pressure to atmospheric pressure. At this point, the wind speed will reach its lowest level, and then the wind will regain its original state. Under ideal conditions, the maximum mechanical power able to be extracted is the difference between the power differentials before and after the turbine, respectively. The mechanical turbine power cannot exceed 0.593 (Betz limit) (Vennell, 2013) of wind power. This factor is called the Betz coefficient. In actual conditions, the turbine can extract 35-40 per cent of the wind power, a good indicator when considering aerodynamic problems (Johnson, 2006).
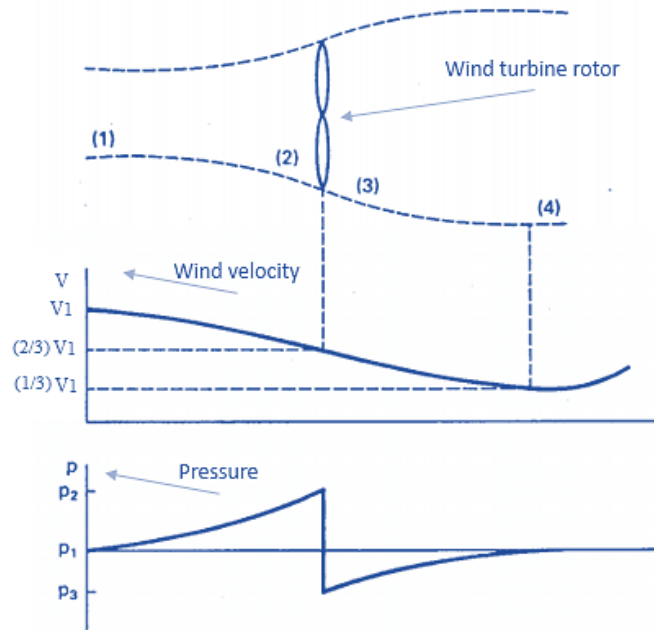
Figure 1-7: Circular tube of air flowing passing over an ideal wind turbine.

(Johnson, 2006)

1.7 Wind turbine performance C_p

Wind power performance (power coefficient) is of great importance in the design and operating conditions of HAWT (Dai et al., 2016). The power coefficient is suitable for measuring wind turbine power and is the most crucial factor that must be taken into account to improve energy. In other words, the power coefficient is an essential factor to take into consideration to optimize wind turbine power and hence, energy production (E_o). Furthermore, it can be defined as the ratio of wind turbine power to wind power (Mahmood, 2011). The relationship between wind turbine performance, wind power, and wind turbine power can be clarified as follows. Maximum wind turbine performance (C_p) occurs only at a certain tip speed ratio (λ), while it decreases at other values of λ, as shown in Figure 1-8. Also, it can be seen in Figure 1-9-a, that the maximum power coefficient occurs at specific wind turbine rotational speeds for each available wind speed. Furthermore, the optimum performance of the wind turbine requires the controller to achieve the maximum possible power from the turbine for all available wind speeds, as shown in Figure 1-9-b. But in this case, the wind speed

should be less than the rated wind speed V_r. The rated wind speed is the wind speed at which the highest wind turbine power is achieved (Mahmood, 2011).
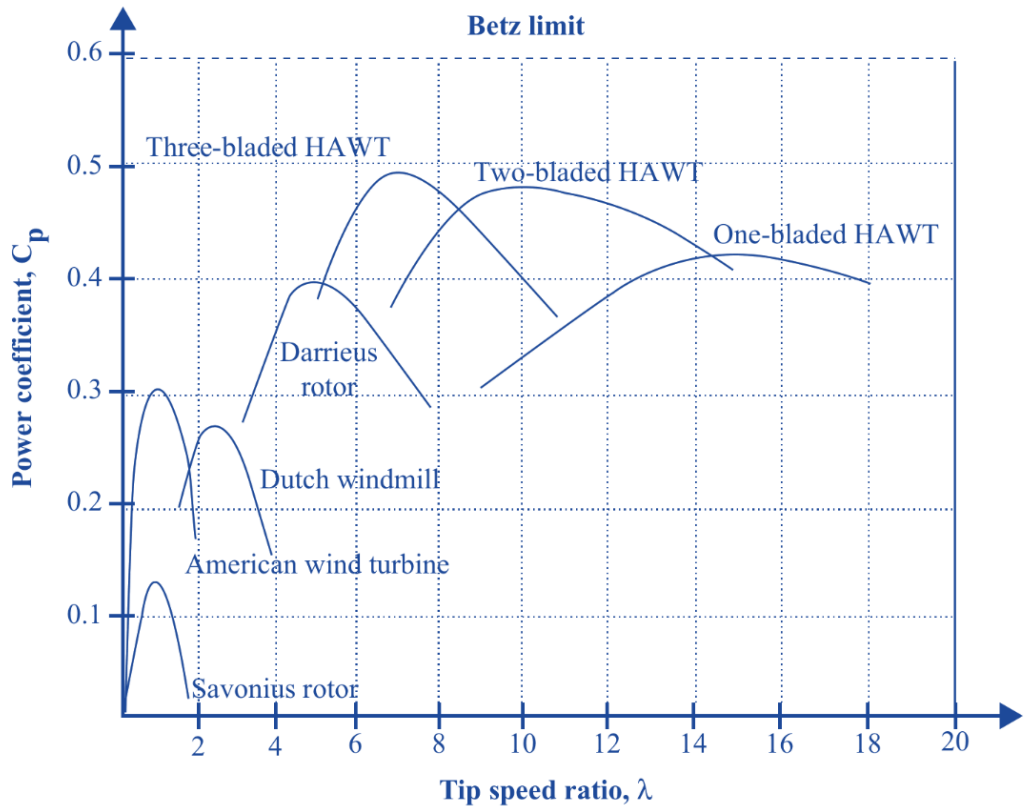
Figure 1-8: wind turbine efficiencies (power coefficient C_p) (Abraham and Plourde, 2014)
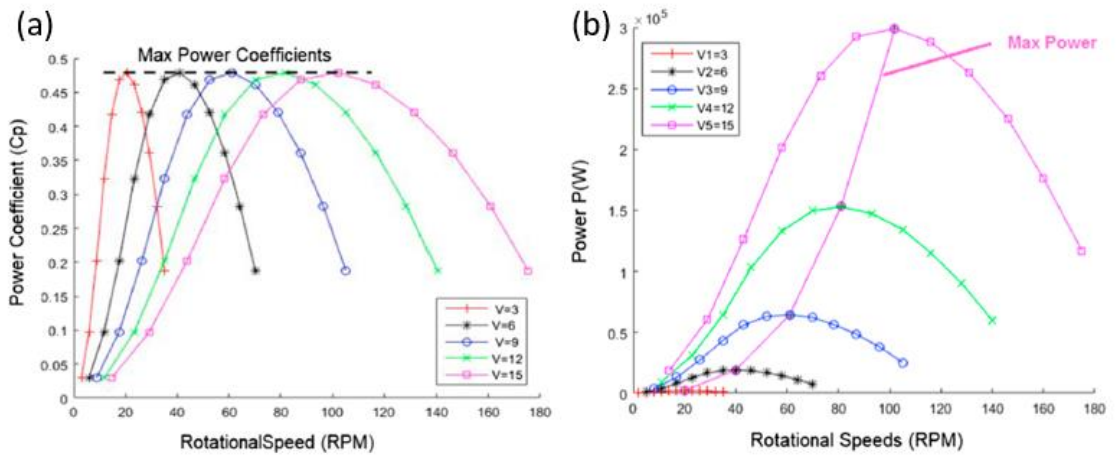
Figure 1-9: Power coefficient (C_p) and Power at different rotational speeds (RPM) and available wind speeds (V_1) (Darwish et al., 2019)

Wind power should continue to increase with increasing wind speeds. It is a function of three parameters, the air density, the surface sweep by the rotor A_{rotor} , and the upstream wind speed V_1. So the wind power P_w can be defined as (Naama et al., 2019):

$$P_w = \frac{1}{2} \rho . A_{rotor} . V_1^3 \qquad \ldots\ldots\ldots\ldots \quad 1\text{-}1$$

Where : $A_{rotor} = \pi . R^2$ (Sedaghat et al., 2017)

The extracted power from wind energy via wind turbine can be defined from the power coefficient formula:

$$C_p = \frac{P_T}{P_w} \qquad \ldots\ldots\ldots\ldots \quad 1\text{-}2$$

Where P_T : the actual wind turbine power; and P_w : the available wind power.

Power coefficient is a function of tip speed ratio. Tip speed ratio can be defined as the ratio of rotor velocity to available wind speed, which can mathematically be defined as (Mahmood, 2011):

$$\lambda = \frac{R . \Omega}{V_1} = \frac{R}{V_1} \frac{2\pi N}{60} \qquad \ldots\ldots\ldots\ldots\ldots\ldots \quad 1\text{-}3$$

Where: R and D are the rotor radius, and Ω is blade angular velocity (rad/s), N is the number of blade rotation (rpm).

Most wind turbines operate with constant wind speeds except when starting and stopping. Wind turbines start at a cut-in wind speed and stop at a cut-off wind speed. They are required to operate at design tip speed ratio (Natarajan, 2014) before rated wind speed. They also should operate at constant power for all wind speeds in excess of rated wind speed. The behaviour of the wind turbine power curve is illustrated in Figure 1-10.
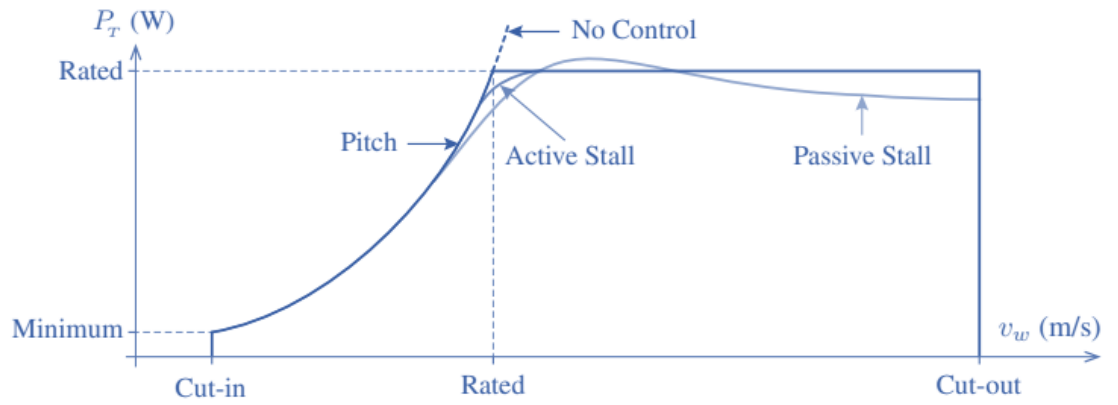
Figure 1-10: Power curve of a commercial wind turbine (Yaramasu, 2016)

Beyond the rated wind speed, a variable pitch wind turbine is required to ensure rated power. In order to ensure that the wind turbine power remains constant, the pitch angle should increase and power coefficient decrease, as shown in Figure 1-11.
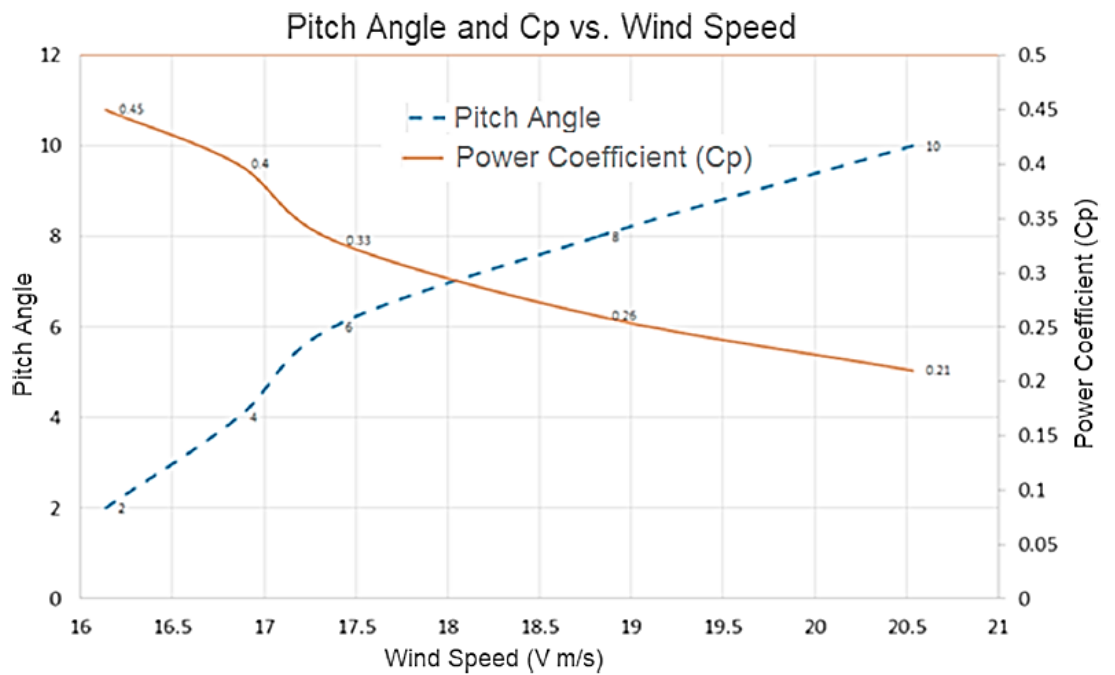
Figure 1-11: Power coefficient (C_p) and pitch angle variations versus wind speeds

(Darwish et al., 2019)

1.8 Significance of the Research

Most types of wind turbines have been designed to operate in regions of high wind speeds. The operation of such turbines in low-speed areas would lose a lot of the energy available in such areas. In order to utilize this energy, sophisticated techniques are required to improve the performance of these turbines to match available wind energy in those sites. There has been a substantial amount of research work on the improvement of wind turbine blade efficiency. However, not all the causes that reduce energy production have been appropriately addressed. In particular, the active flow control of the adverse pressure gradient (APG) boundary layer, which is the major cause of low energy production, has not been investigated to avoid flow separation and improve the wind turbine performance at low Reynolds number locations. This research will investigate the cause for flow separation and the remedial actions to mitigate the flow separation. Furthermore, this research intends to investigate efficient aerofoils for small wind turbines by experimental methods and computational fluid dynamic (CFD) simulations. The innovative outcomes of this research will result in a method to mitigate flow separation and produce improved aerofoils for wind turbines operating at low wind speed regimes.

1.9 Research Objectives

This project aims to improve the annual wind energy production by using small wind turbines which operate in low wind speed regions. The specific objectives are to

- Design and manufacture the selected aerofoils (S822 and S823 aerofoils), which have a maximum lift coefficient and are suitable for selected small horizontal axis wind turbines (sHAWT)

- Conduct experimental tests of the aerofoil's upper and lower surfaces to determine the flow behaviour and gain knowledge of the pressure distribution.

- Verify CFD simulations by conducting necessary tests to ensure numerical errors are minimized.

- Analyse and validate simulations by conducting the necessary experimental tests to ensure that the results simulate reality.

- Conduct an investigation (using simulation) of boundary layer separation and effect of the adverse pressure gradient (APG), with/without AFC techniques.

- Explore methods to optimise the aerodynamic characteristics of the selected aerofoils.

- Develop a Matlab code to predict wind turbine performance before and after improvements to the selected aerofoils and hence, predict wind energy production for low wind speed sites in Australia.

1.10 Thesis structure

An investigation into flow separation and improving wind energy production was implemented using active flow control techniques (i.e. suction and blowing) in this research. Wind turbine performance improvements depend on flow separation delay, so it is necessary to know when and how the separation state occurs and how it can be mitigated.

In Chapter 1, general information about the necessity for renewable energy was presented. It was subsequently illustrated how wind power works, including an evaluation of the different types of rotors used. Then, current wind turbine challenges were presented and explained, and the performance of wind turbines and some related variables were briefly described. Finally, the research objectives and thesis structure were illustrated.

Chapter 2 included the definition of aerofoil components and a general description of the aerodynamics of the blades. Then a literature review of flow separation, active flow control, and optimization wind turbine performance was implemented. Finally, the literature discussion and research gap were revealed. Furthermore, in Chapter 3, selected aerofoils suitable for small and horizontal axial wind turbines were designed and manufactured in addition to determining the locations of active flow control systems for some of these. In Chapter 4, the selected aerofoils were designed using

computational fluid dynamics (CFD), using suction and blowing techniques for the NREL S822 aerofoil identified, but without such technologies for the NREL S823 aerofoil. Then, ANSYS software was used to perform an analysis to verify the simulations by performing the necessary tests to ensure that numerical errors were minimized. Lift and drag coefficients (C_L and C_D) were extracted in these tests.

In Chapter 5, an analysis was conducted to validate the simulations by conducting the necessary tests to ensure that the results obtained from the CFD operations simulate reality, i.e. the results of the experimental tests. An analytical investigation was also carried out on the effect of boundary layer separation and APG on the aerodynamic properties of the selected aerofoils (NREL S822 & NREL S823). Moreover, in this chapter, active control techniques (suction and blowing) for delayed separation of the boundary layer were investigated analytically. As for the penultimate chapter (Chapter 6), from the proposed group of techniques, the best techniques for flow separation control were investigated, using suction and blowing techniques. Besides, Matlab Code was developed to predict wind turbine performance and forecast annual wind energy production for low-speed regions within Australia. Three varying scenarios were chosen for the selected turbine: Case 1: the proposed wind turbine without any modifications; Case 2: the proposed turbine with aerofoils (S822 and S823) but without the application of AFC technologies; and finally Case 3: the proposed wind turbine with aerofoils and the application of optimization techniques. The ultimate aim of this research is to improve the annual wind energy production for specific regions in Australia with low wind speed by using relatively small turbines with a rotor diameter of not greater than 10 meters. Furthermore and in conclusion, suggestions and recommendations for future applications of this work were summarized in Chapter 7.

CHAPTER 2: LITERATURE REVIEW

2.1 Introduction

At low Reynolds numbers, the performance of small-sized wind turbines is relatively poor, due to the inefficient aerodynamic characteristics of the wind turbine blade at low wind regimes. The aerodynamic characteristics represented by lift and drag coefficients are improved by delaying the flow separation, which causes a reduction in power generation from the upper surface of the aerofoil. In order to achieve this, flow separation control techniques must be employed. Active and passive flow control actuators can mitigate or even suppress flow separation by delaying the stall angle and increasing lift, whilst decreasing drag across all angles of attack. These effects create an improvement in the efficiency of the aerofoil. This chapter consists of six sections. In addition to this brief introduction, three main topics will be covered: The first topic is devoted to the problem of flow separation, which occurs as a result of increasing the angle of attack and the resulting adverse pressure gradient (APG), which leads to a decrease in the performance of the wind turbine; The second axis relates to possible solutions which could be utilized to delay the separation and overcome this adverse pressure; The third axis discusses studies relating to improving the performance of the wind turbine and maximizing the annual energy production.

2.2 Aerodynamic characteristics of Wind turbine blade's aerofoil

Before going into specific details of each of the above axes, it is necessary to provide some definitions about the variables related to the blade and an aerofoil profile.

2.2.1 Geometric parameters of the blade's aerofoil

Initially, it is necessary to know the geometric parameters of an aerofoil. An aerofoil consists of the following components, as shown in Figure 2-1: the leading-edge, which

is the forward point of the mean line; the trailing edge which is the final point of the camber line; the mean line (Camber line), which is a line connecting the leading edge to the trailing edge (representing the midway of the distance between the upper and lower surfaces for its entire length); the chord line (C) which is a straight line connecting the leading edge and trailing edge; the thickness; and the camber (which is the maximum distance between the camber line and chord line).
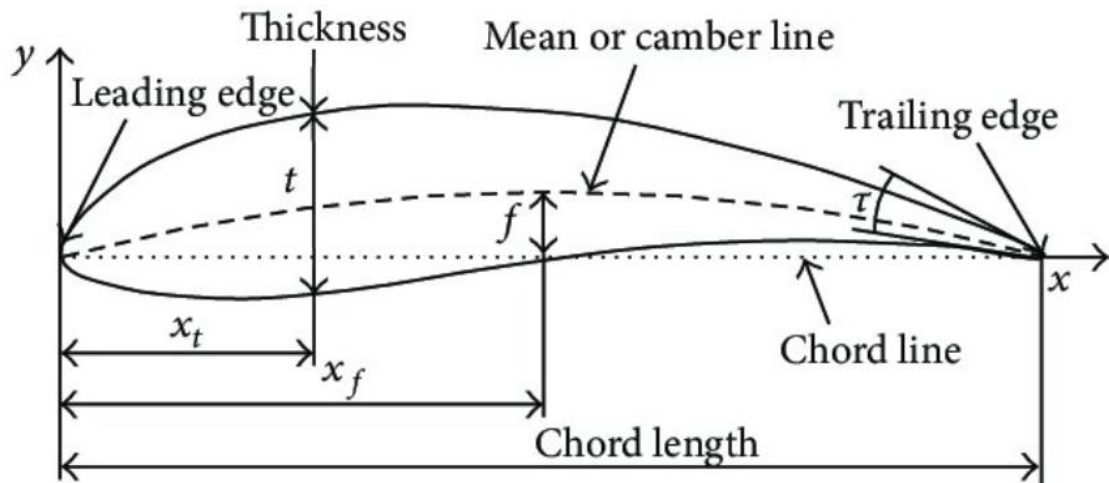
Figure 2-1: The geometric parameter of the blade's aerofoil (Liang et al., 2014)

2.2.2 The stall phenomenon

The stall is a phenomenon which occurs when the angle of attack exceeds the critical angle of attack (which provides the maximum lift). Stalling can be described as the effect of a strong APG, which causes separation (Corten, 2001) and hence, the formation of reversed flow which produces eddies, which lead to reduced lift and increased drag.

2.2.3 NREL Aerofoil Families for HAWTs

In 1948, the National Renewable Energy Laboratory (NREL) along with the former Solar Energy Research Institute (SERI) at Delft University, designed seven aerofoil families (Table 2-1) for horizontal axis wind turbines (HAWT) via the Eppler Aerofoil Design and Analysis Code. These families consist of 23 aerofoils, which have a

maximum lift coefficient, and are suitable for many sizes of wind turbines blade. The reason for designing such sophisticated aerofoils was to eliminate the laminar separation bubbles (Shkara, 2014) and address the need to control the state of the stall, variable pitch and variable rotational velocity of horizontal axes wind turbines (Tangier and Somers, 1995). According to Tangier and Somers (1995), Cao (2011), the NREL's S-Series aerofoils can be classified into "thin" (11% to 15% of the chord line) and "thick" (16% to 21% of the chord line) aerofoils. Thick aerofoils are suitable for stall-regulated wind turbines, whereas thin aerofoils are suitable for a variable-pitch wind turbine. Furthermore, aerofoils with large thicknesses are suitable for sections near to the blade's root for structural and dynamic considerations. However, aerofoils with greater than 26% thickness have undesirable aerodynamic characteristics (Buhl, 2012).

Table 2-1: Aerofoil types for the NREL S-series aerofoil families suitable for HAWT. (Tangier and Somers, 1995)

Blade Length (m)	Generator Size (kW)	Thickness Category	Aerofoil Family (root------------------------------------tip)			
1 -5	2-20	Thick		S823		S822
5-10	20-150	Thin		S804	S801	S803
5-10	20-150	Thin	S808	S807	S805A	S806A
5-10	20-150	Thick		S821	S819	S820
10-15	150-400	Thick	S815	S814	S809	S810
10-15	150-400	Thick	S815	S814	S812	S813
15-25	400-1000	Thick		S818	S816	S817

2.2.4 Reynolds number

Viscosity is a significant factor in aerodynamic performance when operating at low wind speeds. The lift and drag forces are affected by the viscosity, which causes flow separation. Reynolds number can be defined as the dimensionless quantity of the ratio of the forces of inertia to the forces of viscosity (Chen et al., 2017). The most useful form for wind turbines is:

$$Re = \frac{\rho W C}{\mu} \qquad \dots\dots\dots\dots\dots\text{ 2-1}$$

Where: ρ is fluid density; W is the relative flow velocity; C is blade chord, and μ is dynamic viscosity.

2.3 Flow Separation

When the airflow passes through the blade's aerofoil, the boundary layer of the flow will remain connected along the upper surface of the aerofoil (from the leading edge to the trailing edge), at low attack angles. As the angle of attack increases, the circulation increases, the flow curvature increases at the leading edge, and suction become higher at the leading edge near the stagnation point. Correspondingly, the velocity outside the thin boundary layer becomes very high, leading to high viscous shear stresses, which in turn converts the kinetic energy in the boundary layer to heat. Here the boundary layer loses its kinetic energy bit by bit until it reaches a certain state and attack angle, at which it cannot flow continuously, and the boundary layer separates from the surface. At that point, shear stress becomes equal to zero. The APG will accelerate the flow towards the leading edge and generate a reverse flow (Corten, 2001).

In two-dimensional flow, two types of separation can be noted as in Figure 2-2: leading-edge separation (LES); and trailing edge separation (TES). The LES which occurs on a thin camber aerofoil section with a round nose can be divided into short bubble LES and long bubble LES. In contrast, the TES occurs on a thick camber aerofoil section with a round nose. As the name suggests, in short bubble LES

20

situations, a short bubble will be formed on the leading edge. Therefore, when the angle of attack surpasses a specific value, the bubble will burst to cause a sudden decrease in lift coefficient (Figure 2-3) and an increase in the drag coefficient.

Conversely, in long bubble LES situations, when the angle of attack increases, the bubble grows towards the trailing edge. This occurs in low Reynolds number (less than 500,000). Lift coefficient decreases gradually with this type of separation. However, in TES situations, the separation occurs in the trailing edge region. So, when the angle of attack increases, the flow separation moves forward towards the leading edge. This type of separation occurs in thick or cambered aerofoils (15% -35% thickness, according to Corten, 2001) and is the most common scenario regarding wind turbine blades.

When the flow velocity increases, flow separation may occur, which forms a short laminar separation bubble (LSB). However, the LSB may explode at high angles of attack, causing either a long bubble or a separate boundary layer (Marxen and Henningson, 2011). Either way, the lift decreases and the drag increases. At high angles of attack, with increasing lift, an increase in drag occurs. The optimum operation is when the glide ratio (the ratio of lift to drag) is at its maximum.
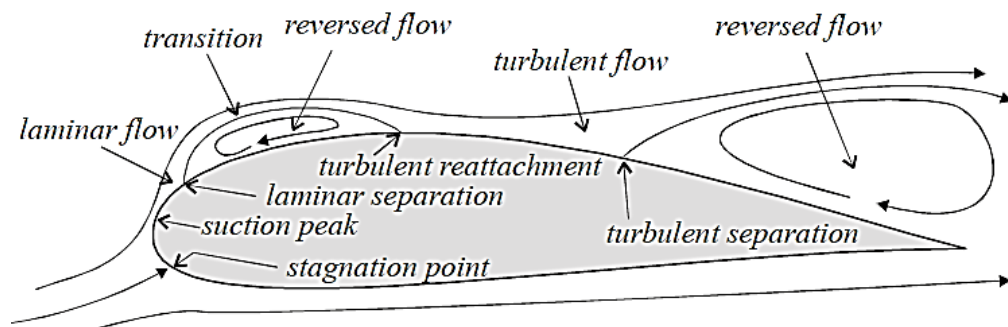
Figure 2-2: Flow regimes within separation above aerofoil (Corten, 2001)
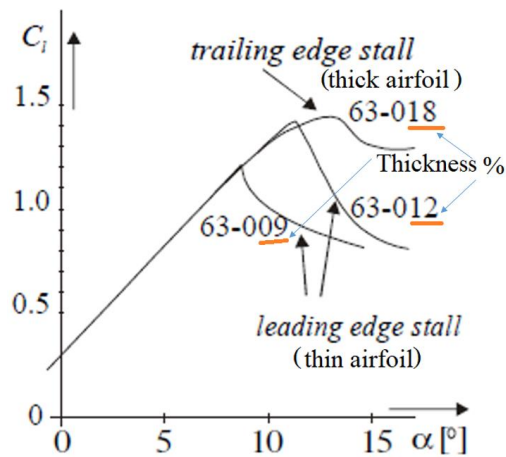
Figure 2-3: The lift –AoA(α) leading to LES and TES (Corten, 2001)

The interrelation between flow separation parameters can be explained in Figure 2-4. According to (Jahanmiri, 2010), when the boundary layer turns from laminar flow to turbulent, its separation resistance improves, and accordingly, the lift will increase. The laminar boundary layer (LBL) can overcome a small reverse pressure gradient without separation. However, when the LBL is separated, free shear stress will be formed, and the flow will turn turbulent at moderate Reynolds number.

In order to fully understand, examine and demonstrate LSB, the transition to turbulent, followed by reattachment to the trailing edge region is an essential factor which designers and researchers must grasp. At low Reynolds numbers, the APG on the suction surface of aerofoils can cause the laminar boundary layer to separate, thus changing to turbulence and after that reattaching to the surface at a downstream area, prompting the development of an LSB. LSB is a specific type of separation that occurs in the leading edge of thin aerofoil sections with a round nose and low camber. This kind of separation occurs at low Reynolds number, i.e. less than 500,000 (Wood, 2011); (Shah et al., 2015).
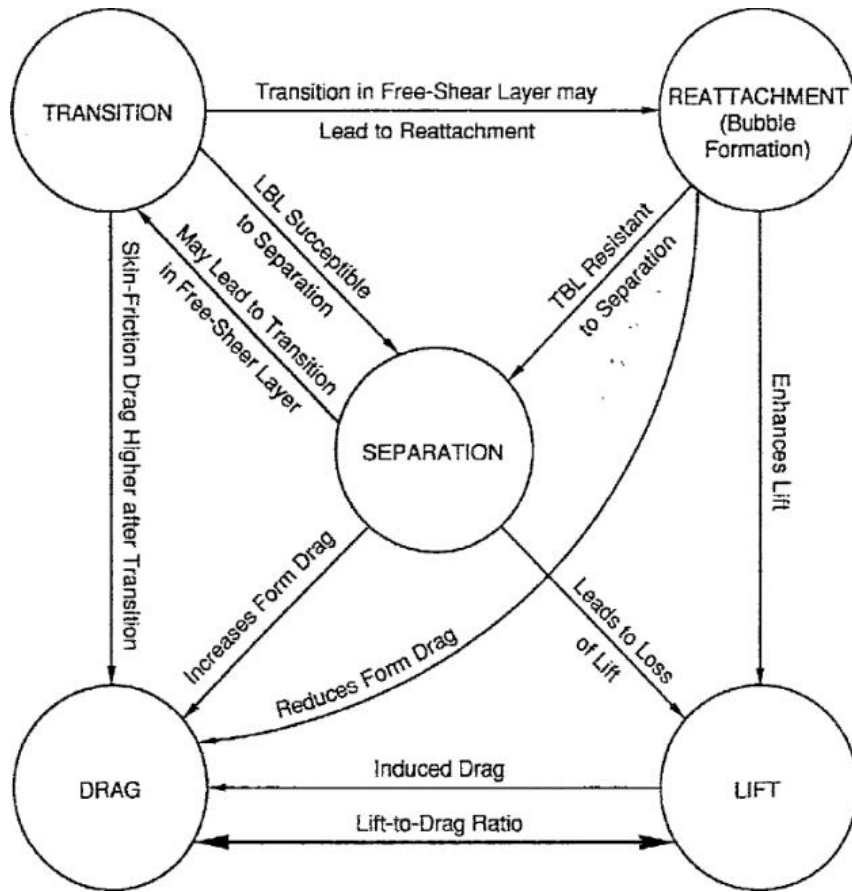
Figure 2-4: The interrelation between flow separation parameters (Jahanmiri, 2010)

A study (Lei et al., 2013) was done on the symmetrical aerofoil (aerofoil SD8020) under low Reynolds number conditions, to investigate trailing-edge separation (TES). The unsteady Reynolds-averaged Navier-Stokes (URANS) was used for the solution. Through the corresponding analysis, it was observed that the laminar bubble burst, creating two types of large scale vortex on the surfaces of the aileron-namely primary and secondary vortices. The movement of the secondary eddies, which are more potent than the primary eddies in terms of the intensity of their shedding, fluctuates the lift coefficient.

2.3.1 Adverse pressure gradient (APG)

Flow separation is caused by the APG, as shown in Figure 2-5. When the angle of attack increases, this leads to slower flow due to the decrease in kinetic energy within the boundary layer. If the pressure gradient is less than zero, this means that the flow

inside the boundary layer will still overcome friction and shear stress will be greater than zero. On the other hand, when the pressure gradient is equal to zero, the shear stress will also be zero, and slipping will not occur, at which point separation will occur, and here the coefficient of friction at the wall will be zero. However, when the pressure gradient is higher than zero, this generates an adverse pressure gradient (APG), forcing the flow to go in the opposite direction, and where the separation process takes place where the kinetic energy of the fluid cannot overcome the APG (Schlichting, 2017); (Howarth, 1960).
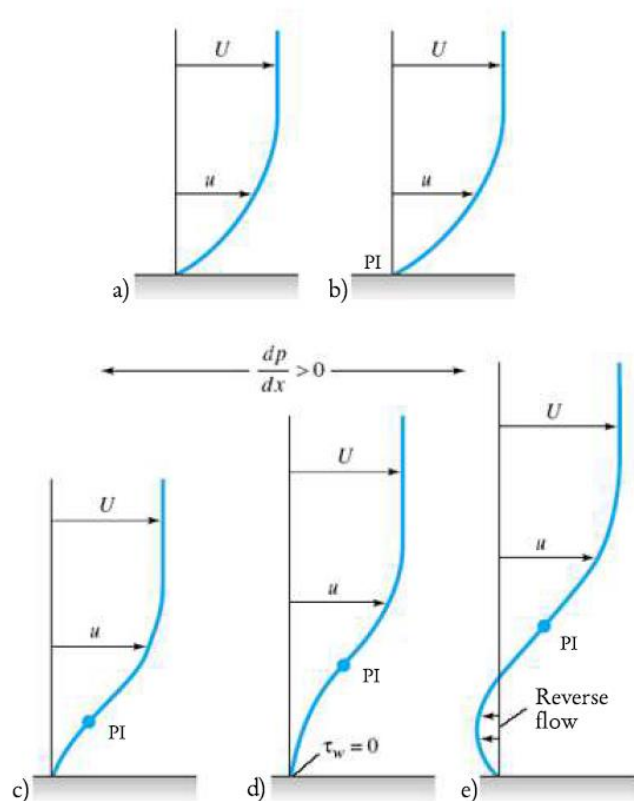
Figure 2-5: Flow separation and APG (Serdar Genç et al., 2012)

Hansen et al. (2014) clarified that on the suction surface (upper surface) of the aerofoil, the APG causes the boundary layer of flow to separate, transforming to a turbulent state, before reattaching to the aerofoil surface, and hence, forming the LSB for low Reynolds number ranges of between 70,000 to 200,000. Increasing the angle of attack increases the bubble size towards the trailing edge of the aerofoil due to an increase in the APG, which has higher inertial forces. A slow circulation may occur in the LSB region, causing reversed flow (Serdar Genç et al., 2012). Furthermore, Yarusevych et

al. (2003), Yarusevych et al. (2007) experimentally investigated the boundary layer and wake development of a NACA0025 aerofoil at various angles of attack $(0°, 5°, and\ 10°)$, at low Reynolds numbers. It was noted that a laminar boundary layer separation occurred over ~50% of the aerofoil's suction surface. Therefore, the boundary layer control separation played a significant role (Ricci et al., 2007). Moreover, Zifeng et al. (2007)) studied the behaviour of flow separation transition for a low Reynolds number aerofoil (GA(W)-1) using the Particle image velocimetry (PIV) technique. The results revealed that when the angle of attack is precisely 7º, the boundary layer might stay attached to surface despite slight effects of the adverse pressure gradient (APG). The transition from laminar to turbulent and later to reattachment with the aerofoil suction surface can be achieved by using active flow control (AFC) techniques.

It is worth noting that the stall reduces the aerodynamic performance of the aerofoil. In other words, an increase in drag coefficient and a decrease in lift coefficient decreases the glide ratio. Therefore this phenomenon contributes to wind turbine performance reduction.

Additionally, Genç et al. (2012) studied the effect of angle of attack experimentally, from $(-12°\ to\ 20°)$ at low Reynolds number $(0.5 \times 10^5\ to\ 3.0 \times 10^5)$, on aerodynamics of a NACA2415 aerofoil. Experimental results revealed a movement in separation and transition points toward the leading edge during an increase in the angle of attack regardless of Reynolds number. However, stall characteristics altered as a result of increasing Reynolds numbers. Besides, at low Re, an unexpected stall would occur. The study also concluded that the fluctuations in the stall angle were due to viscosity impacts, which reduce with decreasing Reynolds number, and hence, a long bubble would be created as a result of a short bubble burst at higher angles of attack.

Shah et al. (2015) simulated the performance of the UBD5494 aerofoil at low Reynolds numbers of $6.0 \times 10^4, 1.0 \times 10^5, 2.0 \times 10^5$ and 3.0×10^5 using the transition $\gamma - Re_\theta$ model. It was found that there was a movement in the LSB towards the leading edge at the point where the angle of attack expands, and this, in turn, would lead to flow turbulence and stall, because of the LSB bursting after its expansion. It was likewise demonstrated that the size of the LSB increases with decreasing Reynolds

number and its movement towards the leading edge is slow. The UBD -5494 aerofoil improves lift-to-drag ratio, and the stall characteristics result in better performance for small wind turbine rotors.

In other research, a laminar flow separation was investigated on a $0.7\ x10^5$ low Reynolds number, NASA (GA (W)-1) aerofoil. PIV was used to reveal flow behaviour around the aerofoil. Results showed that, at high APG, the flow with LSB might separate from the aerofoil suction surface. An unsteady Kelvin–Helmholtz vortex was generated to form a flow transition from laminar to turbulent. At an angle of attack (AoA) of 12°, a reattachment occurred along the upper surface to form a turbulent boundary layer. A turbulent boundary layer is more energized to overcome the APG compared with a laminar boundary layer. It was found that, by increasing the angle of attack, the LSB moved towards the leading edge, the length of the laminar portion of the LSB became longer than the turbulent portion, and there was a dramatic increase in drag coefficient with a corresponding decrease in lift coefficient. It was also discovered that an aerofoil stall occurred when an explosion in LSB occurred (Hu and Yang, 2008). Furthermore, Diwan and Ramesh (2007) stated that to achieve a good understanding of LSB's structure, the height, length, shape of the bubble as global properties should be taken into account. While the Reynolds number declines, the length of the bubble decreases at a greater rate than the height.

2.4 Active and passive flow control techniques

In previous decades, passive flow control devices, such as vortex generators, were widely used. However, they were operating under specific conditions, in such a way that they were unable to respond to the various changes that occurred in the devices. Nevertheless, these methods required the non-consumption of external energy (Sedighi et al., 2020). As a result, attention was given to active control systems, especially those operating in a low number of Reynolds (Asada et al., 2015). Active flow control (AFC) is a procedure which is used to enhance the aerodynamic characteristics of a wind turbine blade using an external energy input and an active flow control system (Maldonado and Gupta, 2017). Researchers also focused on the fields of aircraft and gas turbines by considering the benefits of the use of active flow

control methods (Johnson and Dam, 2008). Three years ago, Aubrun et al. (2017) stated that the trend towards using active flow control in wind energy operating systems had become imperative.

At present, the production of wind energy using wind turbines is considered one of the most important renewable energy sources in the world. So research has been directed towards effective control methods to improve the performance of wind turbines. Many of the techniques used rely in principle on maximizing the ratio of lift-to-drag and delaying the stall phenomenon. AFC methods, which include continuous blowing or suction processes, have evolved to enhance the aerodynamic characteristics of the aerofoil profile. The central role of active flow control is controlling blade loads and aero-elastic reaction. AFC techniques can be classified into four categories (Johnson and Dam, 2008), as shown in Table 2-2. Devices can be classified as Geometric (G) or fluidic devices (F). Geometric devices perform a mechanical movement on a portion of the aerofoil surface, whereas in contrast, fluidic devices change the behaviour of the airflow by adding or removing air from the flow passing through the aerofoil. Some devices include both features, such as synthetic jets, and this is classified as (G/F). Other devices are not subject to the two (G or F) states, such as plasma actuators, which generate power under the influence of an electric field that affects flow behaviour. The second column describes the positioning of the device as being near the leading edge (LE), near the middle of the blade chord (MC), or close to the trailing edge (TE). The third category relates to the lift curve and is classified into two categories. The first works to shift the entire lift curve upward, and so is called increased lift (I). Alternatively, by moving the lift curve downwards, we arrive at decreased lift (D), by changing aerofoil camber. Many devices work in both cases, in which case this is classified as increased /decreased lift curve (I/D). The final category in this column extends the lift curve to delay the occurrence of the stall phenomenon, to be at a higher angle of attack, and here it is called delay stall (DS). The fourth category is characterized by a steady flow condition (S), such as a 'trailing edge flap system', or unsteady flow condition (U), such as a 'pulsed vortex generating jet' which changes the flow state with time. Some devices are described by both cases together and therefore labelled as (S/U).

Table 2-2: Classification chart for AFC techniques (Johnson and Dam, 2008).

	Devices	Geometric (G) / Fluidic (F) / Plasma (P)	Leading Edge (LE) / Trailing Edge (TE) / Mid-Chord (MC)	Inc. Lift (I) / Dec. Lift (D) / Delay Stall (DS)	Steady (S) / Unsteady (U)
1	Traditional Trailing-Edge Flaps	G	TE	I / D	S / U
2	Nontraditional Trailing-Edge Flaps	G	TE	I / D	S / U
3	Microtabs	G	TE	I / D	S / U
4	Miniature Trailing-Edge Effectors	G	TE	I / D	S / U
5	Microflaps	G	TE	I / D	S / U
6	Active Stall Strips	G	LE	D	S
7	Vortex Generators	G	LE	DS	S
8	Blowing and Suction	F	LE / TE	DS	S / U
9	Circulation Control	F	TE	I / D	S
10	Plasma Actuators	P	LE	DS	S
11	Vortex Generator Jets	F	LE	DS	S / U
12	High-Frequency Micro Vortex Generators	G	LE	DS	U
13	Synthetic Jets	G / F	LE	DS	U
14	Active Flexible Wall	G	LE	DS	U
15	Shape Change Airfoil	G	MC	I	S / U

The aerodynamic research focuses on boundary layer transition and LSB, which contribute to the reduction of wind turbine performance (Serdar Genç et al., 2012) (Koca et al., 2018). Constant speeds can be achieved by using active or passive flow control techniques (Johnson and Dam, 2008). These techniques can be illustrated in Figure 2-6. In the current study, the emphasis was placed on blowing and suction techniques which are listed as the eighth AFC technique (Table 2-2). In order to determine where these methods will be most effective, the boundary layer transition, LSB, and adverse pressure gradient (APG) should be investigated carefully.
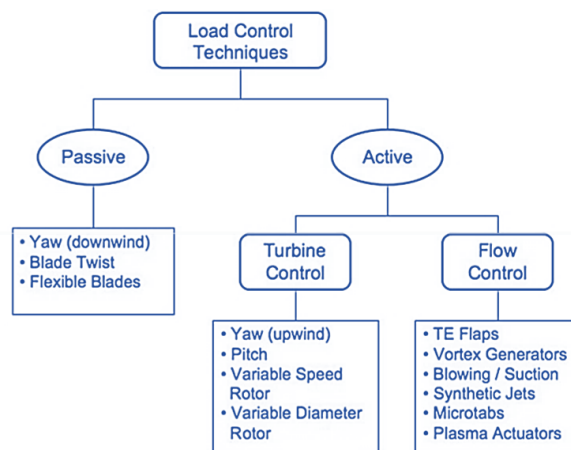
Figure 2-6: The active and passive flow control techniques for wind turbines (Johnson and Dam, 2008)

2.4.1 Plasma actuators and vortex generators techniques

Gross and Fasel (2017), studied boundary layer separation over the NREL S822 aerofoil at Reynolds number of 100,000 using flip-flop jets, pulsed vortex generator jets, and plasma techniques. They found that using active flow control mitigated the unbalanced loads, and hence improved turbine lift.

Further investigation was conducted by Yarusevych and Kotsonis (2016) using a surface-mounted Dielectric Barrier Discharge plasma actuator with the aid of Time-resolved two-component PIV. They investigated the impact of local active flow control experimentally, over a NACA0012 aerofoil at low Reynolds number, on the stability and transition in a LSB. Results showed that using this technique resulted in a reduction in the size of the LSB. Mainly when excitation is applied at the frequency matching the fundamental frequency, the act of reducing the size of the separation bubble would be very obvious. Also, the same technique was used by (Feng et al., 2015), who discovered that the Plasma actuator, when set over the pressure side of the aerofoil close to the trailing edge, led to the creation of a more energetic vortex, which in turn produced a quasi-steady recirculation region, and reduced the velocity. However, when the recirculation was positioned over suction side of the aerofoil to increase velocity, it was found that this would lead to an increase in lift coefficient.

2.4.2 Synthetic jets technique

Maldonado et al. (2010) investigated the possibility of improving aerodynamic characteristics during stall conditions by utilizing synthetic jet actuators to upgrade a small blade wind turbine at low wind speeds. Two areas were measured on the upper surface of the blade. One of these was located near the tip, and the other was close to the root. The PIV technique was utilized to quantify the passage of the airflow over the blade.

Khuder and Itimad (2015) used the same technique and studied the separation flow over a NACA0015 aerofoil. By placing the actuator near leading edge on the upper surface with angles of attack ranging (0º-15º) and with a Reynolds number equal to

4.55×10^5, they demonstrated that by using the synthetic jets technique, the flow over the aerofoil could either entirely or partially be reattached. The researchers also proved that their methodology led to an improvement in maximum lift and delay of flow separation over the aerofoil.

You and Moin (2008) investigated a turbulent flow separation theoretically by using the synthetic jets technique over an aerofoil NACA0015 based on a Reynolds number of 896,000. Their results were validated against experimental data. It was found that there were qualitative and quantitative agreements for controlled and uncontrolled states. Results showed that the synthetic jet technique effectively delays flow separation and improves lift coefficient.

Lengani et al. (2011) investigated the LSB and boundary layer development when subjected to APG, on a flat plate with and without using a synthetic jet technique at low Reynolds number. Results revealed that during the blowing phase, there was a high momentum flow and the synthetic jet technique produced mitigation in the laminar bubble size. However, the boundary layer was reattached to the plate during the suction phase procedure, and, consequently, the separation was delayed.

2.4.3 Acoustic excitement technique

Fayed (2007) and Fayed et al. (2009), empirically studied the effect of internal acoustic excitement on the leading edge, separated boundary layer and the aerodynamic performance of NACA23015 aerofoil. Two positional locations were specified on the aerofoil, 11.5% and 6% of blade chord from the leading edge at the Reynolds number of 3.3×10^5. The frequency range used was 50-400 Hz, and angles of attack 0°, 3°, 6°, 9°, and 12°. The test was conducted using a suction open type subsonic wind tunnel and a smoke wind tunnel. The researchers concluded that this technique is promising and effective in improving the aerodynamic characteristics by generating a suction peak at the leading edge on the upper surface of the aerofoil, causing momentum transfer and thus an increase in the ratio of lift-to-drag, especially when installing the technique in the position of the flow separation point.

Genç et al. (2016) studied the effects of the previous method over a NACA2415 aerofoil at angles of attack of $(0°–25°)$ and at Reynolds range $50,000 - 200,000,$ using force and pressure measurements. In addition, the PIV technique, hot-wire anemometry and smoke flow was used for visualization. The results are summarised in Table 2-3. It was concluded that acoustic disturbance was significantly reduced at low Re. Also, the effect of acoustic control decreased with an increase in Re. Therefore, the acoustic excitation had to increase with the increase of Re. Finally, the researchers claimed that the acoustic excitation reduced the formation of vortices and forced the flow to attach to the aerofoil suction surface.

Table 2-3: The summarised results for the above study

Re × 1000	Frequency (Hz)	α_{stall} delay (º)	Lift ($\uparrow^+$)	Drag ($\downarrow_-$)	L/D ($\uparrow^+$)
50	certain range	12 → 16	30%	50%	6 → 9
75	700	13 → 17	14%	34%	20%
100	1200	15 → 17	-	-	8%
150	1800	15	-	-	5%
200	-	No effect	-	-	-

Ricci et al. (2007) investigated the technique above on LSB, using a thin aerofoil and angles of attack between $2°$ and $8°,$ and frequency range of $200 - 800$ Hz, at low Reynolds number $(60,000)$ with and without an acoustic excitation actuator. A quantitative Infrared (IR) thermography method was employed to determine the positions of separation, transition and reattachment points. It was concluded that the sinusoidal sound wave at a specific frequency reduced the LSB dimension, causing reconnection to the upper surface of the aerofoil. Also, it was mentioned that it was

not possible to determine a specific value from the given frequencies that convert the flow from laminar to turbulent before the separation occurred.

2.4.4 Zero-mass-flux (ZMF) piezo fluidic actuator

Stalnov et al. (2010) examined the possibility of using active flow control (AFC) methods in place of passive flow control in order to enhance the performance of wind turbines. They did this using a zero-mass-flux (ZMF) piezo fluidic actuator to control boundary layer separation for thick aerofoils. They proved that ZMF actuators were better than passive vortex generators, at delaying boundary layer separation. The reason for this is that ZMF fluidic actuators can be used to control flow separation for a wide range of Reynolds numbers. The results proved that AFC would give double the highest lift at low Reynolds numbers and reduce the turbine cut-in wind speed. It was also revealed that AFC operates to postpone the stall point and reduce the drag even for polluted blades. Zero-net-mass-flux oscillatory jets or synthetic jets demonstrated good feasibility for industrial applications and effectiveness in controlling flow separation.

2.4.5 suction and blowing techniques

The final techniques to be discussed here are suction and blowing techniques. In these methods, there is a delay in the stall point. These techniques work by adding or subtracting momentum from the boundary layer. These processes mitigate the APG impact, and hence delay the flow separation occurrence towards the leading edge of the aerofoil profile. One of the notions attached to blowing and suction is circulation control which leads to increased lift coefficient in an aerofoil, and subsequently, moving the rear stagnation point to the pressure side of the aerofoil (Johnson and Dam, 2008).

Genç et al. (2011) investigated the performance of transition and turbulence flow at low Reynolds numbers. Their experimental work included using hot-wire anemometry to reveal the LSB for a NACA2415 aerofoil, using an angle of attack of 8° and a Reynolds number of 200,000, and numerical simulation using a K-K_L-w model. The

results showed that the LSB is not completely removed through a single blowing or suction technique, but is either delayed towards the trailing edge or reduced. The researchers also established that by utilizing larger amounts of suction and smaller amounts of blowing, the aerodynamic characteristics of the aerofoil were improved by eliminating the LSB depending on the location of active flow control.

Jalal et al. (2010) studied the separation control on the aerofoil model numerically, using a NACA2412 aerofoil, with the jet blowing at different angles of attack ($0° - 30°$) up and beyond the stall angle and at Reynolds numbers ranging from 3.4×10^5 to 1.7×10^6. The study was conducted according to Reynolds-average Navier-Stocks equations. A revised k-ω model was also proposed for the solution. The effect of blowing slot location and its velocity on the performance of the aerofoil was studied. The results indicated that when blowing at $x/c = 0.3$, with a blowing speed of twice the inlet velocity, blowing technique achieved its optimal efficiency in terms of controlling the separation of the flow. An experimental study of the above variables was conducted, and the results were consistent.

Jawad et al. (2014) used the same technique and obtained similar results but with a NACA4415 aerofoil at angles of attack of $5°, 10°$, and $15°$. For large separation regions, the jet blowing was insufficient to reduce the flow separation. It was found that CFD simulation was an efficient and accurate way to predict the control of flow separation using jet blowing technology. The results showed that by using this technique, there was a significant increase in lift even with a zero attack angle, which in turn would delete the vortex shedding which might occur near to the trailing edge of the blade's aerofoil. It also noted that a vast separation was not entirely controllable using the blowing technique.

Müller-Vahl (2015) used a constant blowing technique over a NACA0018 wind turbine blade, for a specified range of Reynolds numbers (125000 – 375000). Slots placed both near the leading edge and in the middle of the aerofoil were examined to monitor flow behaviour. The experimental results revealed that, at the leading edge slot location, the stall phenomenon is delayed for high momentum blowing, and hence, this increases the lift for a wide range of angles of attack. Nevertheless, when the momentum coefficient was low, there was a loss in lift and increase in drag. Also, the

study stated that blowing in the middle of the aerofoil produced a significant effect, and the trailing edge flow separation was suppressed for angles of attack before the stall. Finally, they demonstrated that blowing near to the leading edge was more effective than in the middle of the aerofoil chord.

According to (Dumitrache et al., 2014), trailing edge blowing is an alternative type of AFC technique used to investigate a high-lift configuration. Results showed that a delay in flow separation occurred, leading to an increase in flow circulation, and hence, a greater lift was generated.

On the other hand, Chawla et al. (2014) investigated a constant suction technique for controlling boundary layer separation over NACA0012 and S814 aerofoils at low Reynolds numbers, ranging from $(1 \times 10^4 \text{ to } 1 \times 10^5)$, for small HAWT. They concluded that the air was sucked from the upper surface in multiple places, and therefore, depending on the increase in lift coefficient, the most effective slitting sites could be determined, as shown in Figure 2-7. The suction system was implemented using a vacuum pump and a Venturi tube to measure and maintain a steady suction flow rate. Also, a wool tuft visualization was used to monitor suction effects. The efficiency of the aerofoil was shown to increase with increased lift and lower drag.

(a) NACA 0012 with suction slit at $x/c = 0.36$ (b) S 814 with suction slit at $x/c = 0.24$
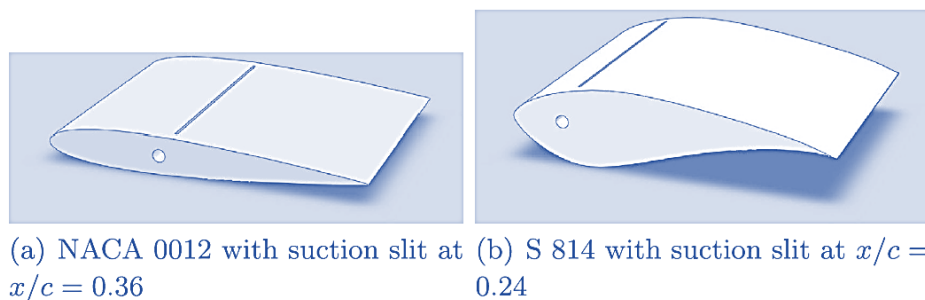
Figure 2-7: NACA0012 and S814 with suction slit at $x/c = 0.36$ and 0.24 respectively (Chawla et al., 2014)

Blowing and suction as active flow controls were computationally utilized to investigate the LSB for a NACA2415 aerofoil at Reynolds number of $2x10^5$ and an angle of attack of 8°. The researchers demonstrated that, in the previous studies, a jet slot with a width of 2.5% of the chord length was placed on the upper surface of the aerofoil to be investigated using a developed k-k$_L$-ω and k-ω SST transition model

which could be compared with experimental work to predict the LSB. According to (Serdar Genç and Kaynak, 2009), it can be stated that the aerofoil performance improves in two cases, the first is when the ratio of suction speed to the inlet speed is the highest possible, and the second is when the ratio of blowing speed to the inlet velocity is the lowest possible. However, the first case (highest suction speed/inlet speed) yields better results than the second case (lowest blowing speed/inlet speed). Therefore the optimum case can be achieved with high-speed suction or with low speed blowing.

2.5 Wind turbine performance and energy production

In order to improve wind turbine power output, due to losses in aerodynamic characteristics of the wind turbine aerofoil section, the structural behaviour of the wind turbine blade and inefficiency caused by its mechanical systems needs to be addressed. A study by Johnson and Dam, (2008) showed adverse effects due to the LSB which occurs at low Reynolds number in the leading edge of the aerofoil. Two essential methods to eliminate this problem and enhance wind turbine performance are blowing and suction techniques. A high momentum of air can be added to the boundary layer in the blowing technique, while low air momentum can be achieved using the suction technique (Johnson and Dam, 2008).

Ricci et al. (2011) investigated the possibility of enhancing the performance of a 10 kW small wind turbine through mitigating LSB at low Reynolds numbers by using a Micro Electro Mechanical System (MEMS). In the study, the LSB transition type and turbulent reattachment point's location were revealed utilizing the infrared thermography method. The researchers stated that lift increases by a ratio of 50% at Reynolds number of $1x10^5$, and this obviously led to improvements in wind turbine performance.

Ram et al. (2013) investigated the optimization of USPT2 aerofoil at low Reynolds number by using a Genetic Algorithm (GA) for a small wind turbine. The purpose was to create a rough insensitive aerofoil in the wind turbine blade's tip against dusting,

which leads to a reduction in the performance of the aerofoil. The results showed that the optimum performance of the aerofoil occurs at angles of attack between 4° and 10°. Also, it was proven that this particular aerofoil is suitable for small wind turbines.

Ali (2014) investigated the optimal performance of a small wind turbine blade used in built-up areas to improve the wind turbine power generation using winglets at the tip of the blade. The results revealed that there was an enhancement in the aerodynamic performance of the wind turbine, hence improving its power output.

Lanzafame and Messina (2009) developed a new layout for a small wind turbine (sWT) using only two parts, each non-twisted with variable chord lines along the blade, to improve performance and reduce cost. Some losses were revealed due to vortices appearing on the tips of each part, but these losses can be tackled using winglets. It was concluded that by using this layout, there was a power output gain for all ranges of wind speed between cut-in to cut-off.

In another experimental study, a simulation was conducted on two types of horizontal axis wind turbine blades, one of which was designed according to the theory of blade element momentum (with twisted angles), the other blade being a non-twist angles type with a constant chord length along the rotor blade. This study aimed to investigate the performance of the wind turbine in both cases. The outcomes indicated that the wind turbine with a twisted angle performed 50% better than the one without (Lee et al., 2016).

An unstable aerodynamic simulation of wind turbines was carried out in a study by (Cai et al., 2016) which considered the effects of wind shear, tower shadows and yaw regulation using CFD. The results showed that the aerodynamic forces change periodically with the rotation of the blades, as the aerodynamic forces reach their maximum lift when the blade reaches the highest position and vice versa. The results also showed that the yaw system affects the output of the aerodynamic loads, where the loads are the highest in the areas facing the wind, and lowest in the wind direction areas. The researchers determined that such studies may contribute to solving aerodynamic problems and optimal designs for enhancing future wind energy.

An experimental and computational study was conducted on small wind turbines to predict and improve their aero-acoustic and aerodynamic performance. An acoustic camera was used to conduct aero-acoustic measurements for wind turbine power output. Improved Delayed Detached Eddy Simulation (IDDES), as well as aeroacoustics using the Ffowcs Williams and Hawkings (FW-H) method, and an unsteady 3D analysis were used in the computational analysis. Procedures were analysed and optimized for many aerofoil profiles of turbine blades. The turbulence model, Navier-Stokes equations, and the continuity equation were used in the solutions. In this study, simulations were validated by the experiment. Moreover, results demonstrated that the proposed semi-three-dimensional improvements were successful in improving the aerodynamic and acoustic performance of small-scale wind turbines. (Benim et al., 2018).

An experimental simulation study was performed on two Aerofoils, NACA0012 and NACA2412. In the simulation system, three models were used: the Spalart-Allmaras, the k-epsilon (RNG), and the $k - \omega$ shear stress transport (SST). All of these models were consistent with experimental results at angles of attack from -5 to 5º. The parameters of blade engineering, represented by the blade chord and the twisting angle of the blade, were calculated. Lift-to-drag ratio was dependent on determining the optimal case. The study's goal was to establish the optimal blade design for horizontal axis wind turbines for different Reynolds numbers to improve their performance. Based on BEM theory, researchers found that the change of the aerofoil type (like NACA2412 or NACA0012) affects the performance of the wind turbine. The research also concluded that the NACA2412 aerofoil achieved the highest performance coefficient compared to its NACA0012 counterpart (Oukassou et al., 2019).

A numerical study was implemented to improve the performance of the V47-660 kW horizontal turbine by using 50mm diameter spherical dimples on the suction side of the blade. The simulation was conducted using the incompressible Shear-Stress Transport turbulent model. The study assessed the effect of the dimples' radius, their location, and quantity on torque, flow separation, power generation and hence overall performance of the wind turbine. The results showed that dimples increase torque and power generation if they are set up correctly. One hundred fifty dimples were used

with a pitch distance of 200 mm with three rows on the suction surface of the blade. The results showed that dimples could improve torque by 16% (Sedighi et al., 2020).

A genetic algorithm to improve the hydrodynamic performance of tidal turbines based on the lift-to-drag ratio was adopted by increasing the blade's chord in the middle and improving pitch angle distribution. This study proved that the leading power generation positions were concentrated in about 75% of the blade's span (that is, at the location of the three-fourths of the blade, starting at the blade root.). The study showed that the power coefficient was improved by 2%, especially for the tip speed ratio (λ) between 4 and 6. (Zhu et al., 2020).

2.6 Summary

The structure of this literature review was summarised in three stages: flow separation (without AFC), flow separation control (with/without AFC), and improving wind turbine performance.

The research reviewed reveals that separation flow could be mitigated or suppressed, and the stall angle could be delayed by using active flow control actuators increasing lift curve and decreasing drag curve. These progressions will improve the productivity of the aerofoil. The published research also demonstrated that with an increase in Re, the laminar flow would become turbulent and thus would result in a decrease in the size of LSB. On the other hand, in order to obtain a high resolution for visualizing the behaviour of the flow as it passes across the aerofoil (such as position separation, re-attachment of flow (to the upper surface of the aerofoil), and state of flow transition (from laminar to turbulence)), PIV and IR thermal imaging techniques, as well as smoke technique, were used to visualize flow behaviour when passing over the aerofoil.

Regardless of the above, studies, using AFC methods, have used techniques, using only a single aerofoil position. Other studies may be restricted by using a low range of angles of attack (less than or equal to 10°). The use of aerofoils for horizontal and small-axis wind turbines, such as the NREL S822 and NREL S823 aerofoils, was not widely covered. On the other hand, suction and blowing techniques have not been used together, and the effect of changing their positioning and changing their speed has not

been studied on the performance of the small size wind turbine when operating in areas of low wind speed. Furthermore, the effect of changing the speed of suction and blowing on the performance of the aerofoil was not studied. Finally, the annual energy production for low wind speed sites in Australia was not predicted by using enhanced small horizontal wind turbines.

In the current study, the two following approaches will be implemented: (1) Use blowing and suction techniques together or separately, with or without changing their velocities to delay flow separation; and (2) Use of aerofoils proposed for small wind turbines with a diameter of 10 meters. Both methods will be adopted to improve the performance of small wind turbines and thus improve the annual energy production for low wind speed sites in Australia.

CHAPTER 3: EXPERIMENTAL SETUP

In this Chapter, aspects relating to wind tunnel experiments are discussed. These events include preparations for making models, tools, parts and equipment relevant to the wind tunnel for testing. A series of laboratory experiments were conducted to determine the flow behaviour and gain knowledge of the pressure distribution on the upper and lower surfaces of the aerofoil. The aerodynamic tests were conducted for proposed aerofoils (S822 and S823). The plan for the experimental methodology is illustrated in Figure 3-1. Multiple systems were utilized in the laboratory to conduct such a complex test. The components of each system are detailed separately, indicating how the parts of each system are interconnected.
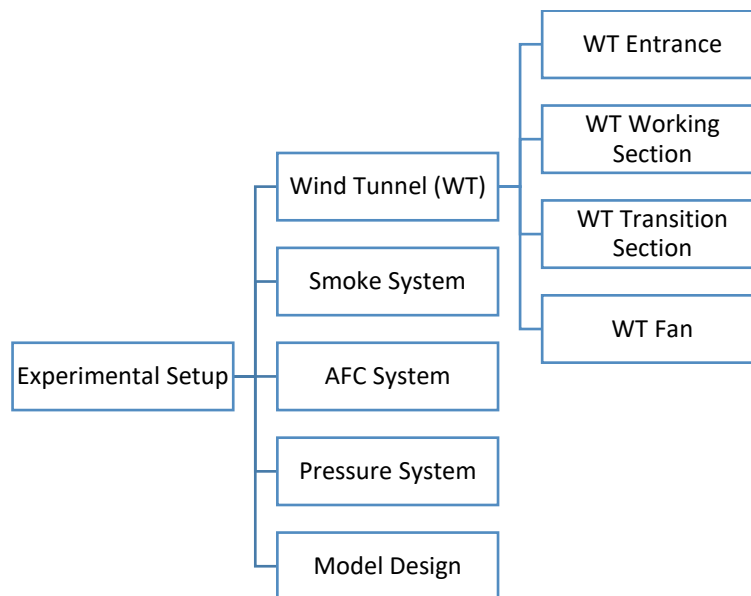
Figure 3-1: Structure of an experimental setup

3.1 Wind Tunnel

In order to simulate the effect of airflow over and around aerodynamic objects, a wind tunnel is required. A wind tunnel is a specialized tool used to conduct experiments and undertake research on the effect of air movement on objects, either by pulling or pumping air into and out of the wind tunnel. The wind turbine blade model, which is manufactured considering similarity laws, is an example of an object which can be

tested to examine aerodynamic behaviour. On an actual wind turbine, the wind turbine blade moves in the air, whereas in the wind tunnel, the air moves around the wind turbine blade, which is static. There are several types of wind tunnels, including supersonic and subsonic. A wind tunnel can also be open or closed (Figure 3-2).

In the open type, the air is either pulled or pushed through, and this is the more common configuration since energy consumption is not an essential factor.

Conversely, a closed wind tunnel is one in which air is circulated inside a closed loop where the flow quality is largely controlled (Calautit et al. (2014). The primary dimensionless variable when conducting tests in low-speed wind tunnels is the Reynolds number (Cattafesta et al. (2010). The model used within the wind tunnel test section needs to be small enough to fit inside. Therefore the similarity analysis of the model must be considered (Cermak (2003). In the subsonic wind tunnel, the density of the air is almost constant.
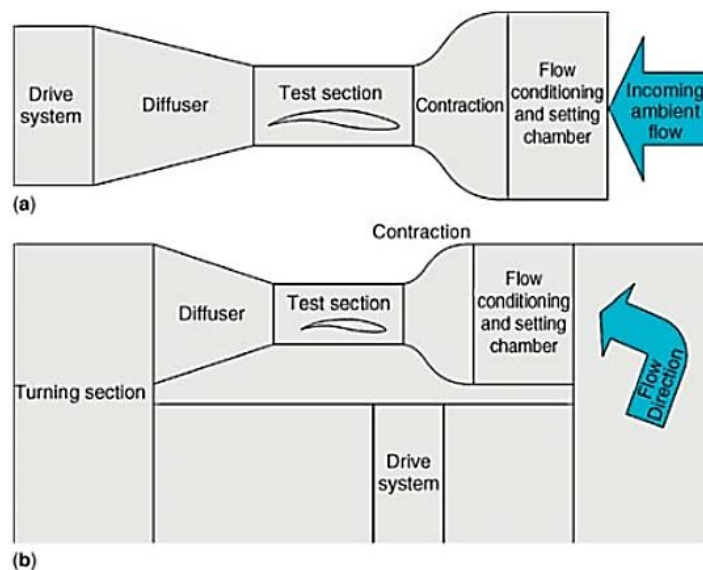
Figure 3-2: Schematic of open (a) & closed (b) circuit wind tunnels (Cattafesta et al., 2010)

In this project, the flow separation around models of wind turbine blade aerofoils was investigated using a subsonic open type wind tunnel at the University of Southern Queensland (Figure 3-3). The wind tunnel in this project consisted of four parts: the entrance; test section; transition section; and fan.
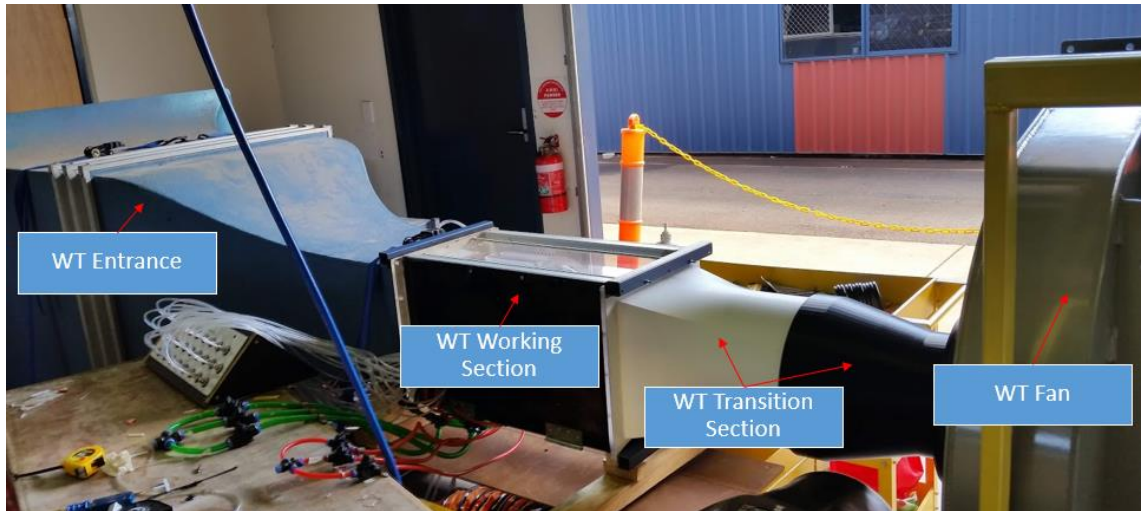
Figure 3-3: The wind tunnel used in these experimental tests

3.1.1 Wind tunnel entrance

The entrance to the chamber includes three mesh-wire sections (Figure 3-4) to reduce the speed of the irregular axial wind tunnel. On the other hand, within the contraction section, the cross-section is reduced, which accelerates the airflow and decreases the static pressure at the test section by 0.156 kPa at an axial wind tunnel velocity of 15.8 m/s.

Figure 3-4: Three mesh-wire sections in WT entrance section

3.1.2 Test section

Following the entrance is the test section or working section, where models (e.g. an aerofoil) should be tested. Figure 3-5-a and Figure 3-5-b illustrates the designed and manufactured working sections, respectively. Perspex was used to manufacture the wind tunnel test chamber, to produce internal dimensions of 300 mm x 300 mm x 600 mm. In order to change the aerofoil's angle of attack, a circular opening with a diameter of 170 mm was placed on each side, located at a horizontal distance of 225 mm from the WT entrance and a vertical distance of 150 mm from the upper surface. In order to measure air velocity through the working section using an anemometer, a 5 mm diameter hole was positioned in the middle of the upper surface close to the inlet. Also, two holes were placed in the upper surface of the test section to check the static pressure inside. The test section and all other components of the wind tunnel were checked to ensure they were level.
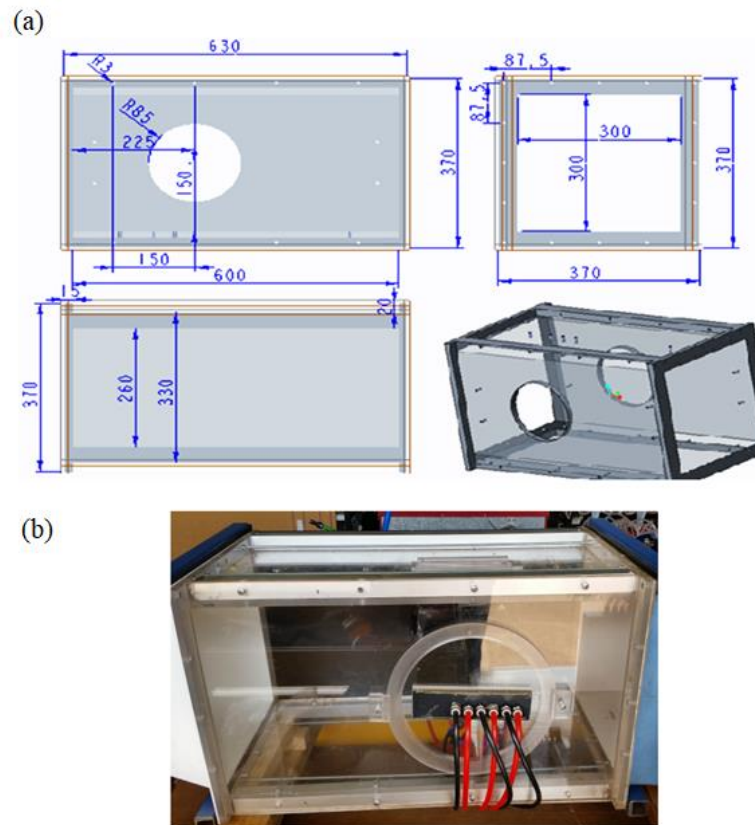
Figure 3-5: (a) The schematics of the wind tunnel working section; (b) its constructed form (All dimensions are in mm)

3.1.3 Transition section

The wind tunnel was modified by designing an alternative exit section as the third part of the system. This section is known as the transition section and was manufactured after being designed using Creo software. The transition section consists of two pieces (Figure 3-6), part (a) connected to the working section and part (b) connected to the fan. Both parts were produced using a 3D printer.
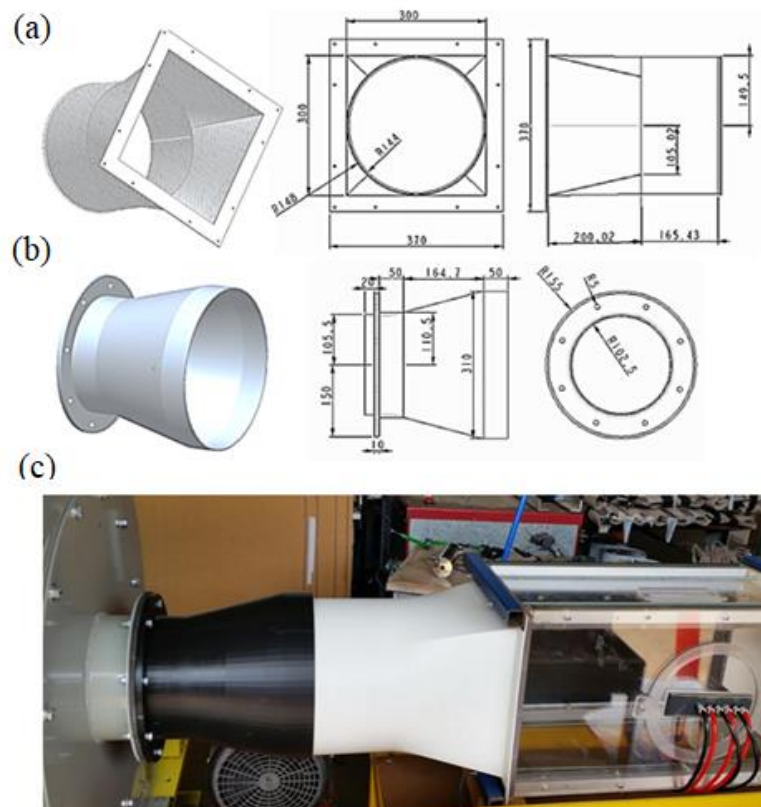
Figure 3-6: (a) & (b) Design parts of a wind tunnel transition section; (c) their manufactured parts (All dimensions are in mm)

3.1.4 Low-speed wind-tunnel fan

The wind tunnel fan used in this project is shown in Figure 3-7. The fan was set up to provide a maximum speed of 15.8 m/s at the commencement of the test section. Potential maximum speeds were limited by the flow separation using the smoke system: at high speeds, it is challenging to observe flow behaviour inside the wind

tunnel because the smoke dissipates quickly. The fan outlet is directed towards the laboratory outlet in an attempt to eliminate smoke build-up, which could cause obvious work, health and safety hazards. The planned centrifugal wind tunnel fan is illustrated in the same figure, and its specifications are listed in Appendix A-1.
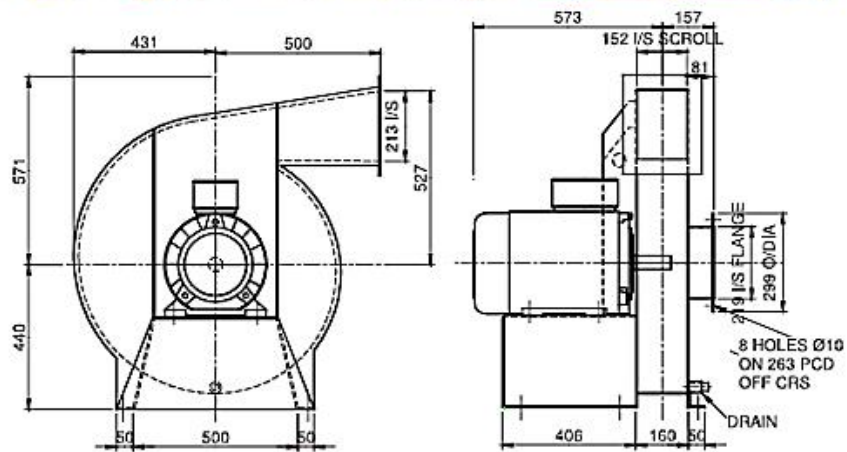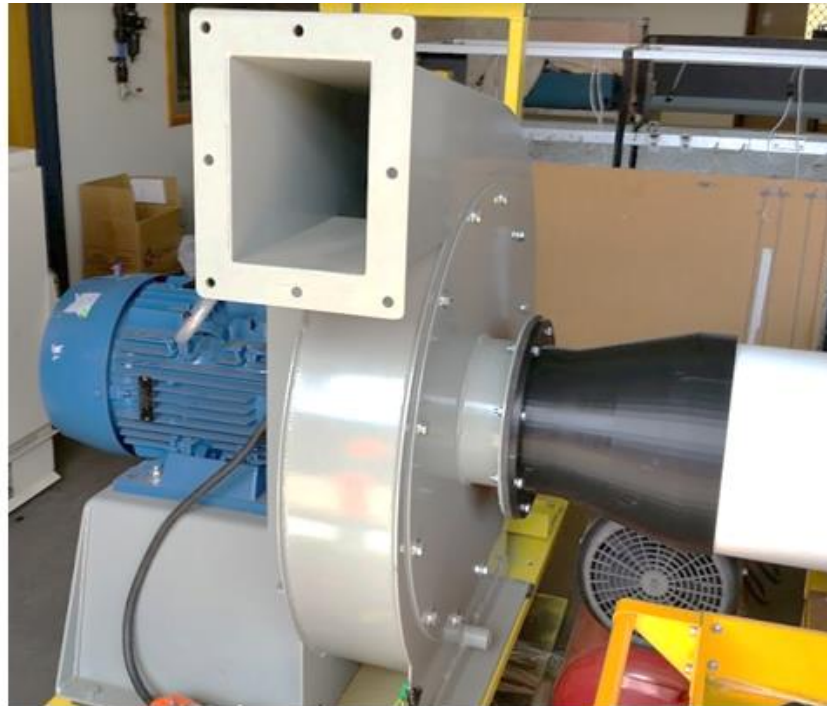
Figure 3-7: Pictorial view of the fan connected to the wind tunnel exit (All dimensions are in mm)

3.2 Smoke System

Smoke technology plays an essential role in detecting the behaviour of eddy formation and separation of flow within the wind tunnel. The smoke system components (Figure 3-8) consist of the following items: smoke generator; air compressor; a voltage of 110-120 VAC; liquid propylene glycol; power transformer; and the smoke wand.

The most important item is the smoke generator (The AEROLAB Smoke Generator V1) that requires compressed air at a pressure of 150 psi. Therefore, a 2HP, 50L air compressor was used for this purpose, which requires a voltage of 110-120 VAC, so that a power transformer became essential to convert the power from domestic power (240VAC) to system power (110VAC). Moreover, the liquid used in the smoke generator is liquid propylene glycol, as recommended by the manufacturer. Furthermore, all smoke generated will exit from the smoke wand located towards the wind tunnel entrance. More information about this system can be found in Appendix A-2.

Figure 3-8: The components of the smoke system

The smoke system was initially tested inside the wind tunnel, without aerofoil models and subsequently tested with aerofoil models. In the former case, it was found that the smoke streams were oscillating, sometimes rising up and at other times descending. In order to eliminate these occurrences, the smoke level was adjusted to hit the leading edge. Moreover, In order to reduce flow turbulence, a paper honeycomb was used (Figure 3-9) consisting of pieces of aluminium 100 mm long and 20 mm wide. The use of aluminium instead of paper was solely due to the heat in the smoke and obvious potential risk of fire. Oscillation was reduced somewhat but not to a satisfactory level. Additionally, the use of aluminium tubes, 100 mm long and 12 mm in diameter, which placed in the paths of smoke, as shown in Figure 3-9, helped to stabilize the smoke.

One critical operating requirement was to incorporate a safe smoke exhaust system. Therefore, a hose 300 mm in diameter and 5 m in length (Figure 3-10) connected to the fan outlet, was used to expel smoke out of the laboratory.
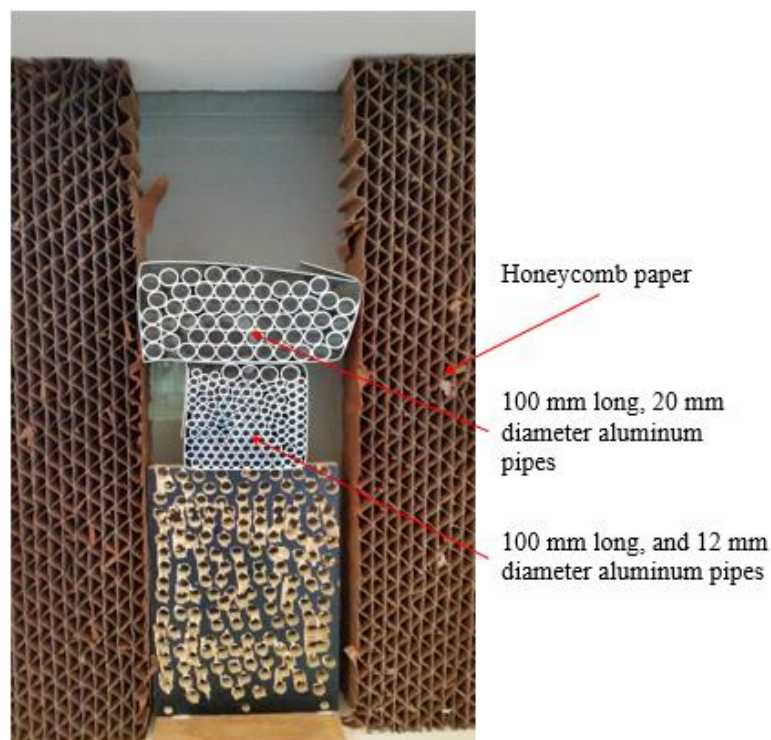
Figure 3-9: Use honeycomb paper and small aluminium pipes to reduce the ripple of smoke.

Figure 3-10: The wind tunnel's smoke exhaust system

Additional instruments were built into the smoke system (Figure 3-11). In order to calculate the viscosity of the air, the laboratory temperature needed to be checked. So, a hydrometer (Figure 3-11a) was used to read the temperature of the location where the test was performed. At the same time, a high-speed camera (Figure 3-11b) was used to capture the smoke streaklines formed during the flow separation. Furthermore, to ensure the accurate visualisation of the flow, sunlight barriers (Figure 3-11c), and external light (Figure 3-11d) were used. When the smoke wand moves slightly up or down, it may affect the direction of the smoke circulating the aerofoil. Therefore, the deviation of the smoke may present a false perception. This way, the smoke wand was set in a position where smoke always hit the front of the model (Figure 3-11e).
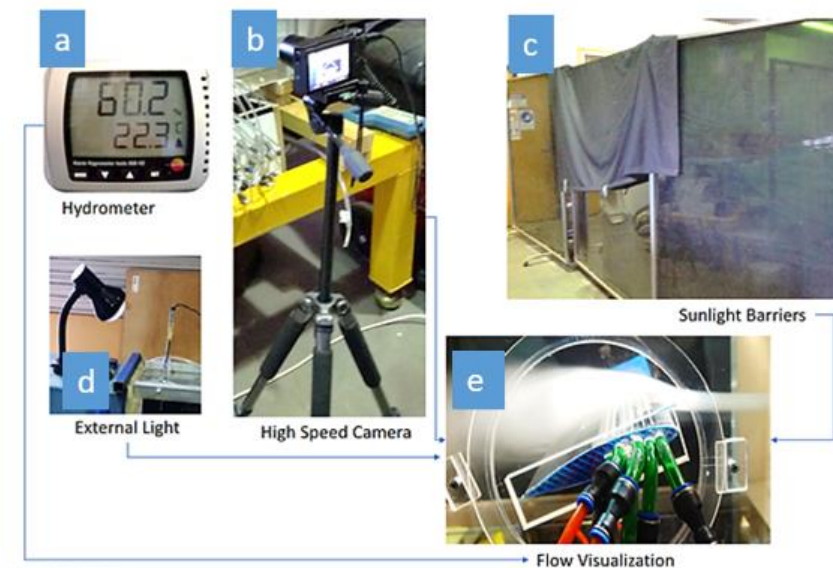
Figure 3-11: Equipment used in the flow visualisation process

3.3 Active flow control techniques: Suction & Blowing system

In order to control flow separation, two active flow control techniques were used. These methods are blowing technique, in which momentum is added to the boundary layer to overcome the reverse pressure gradient, and suction technique, in which an amount of momentum is removed from the boundary layer to reduce the intensity of the reverse pressure gradient. The first component in this system was the air compressor (Figure 3-12a) that provides the system with compressed air via a 12 mm OD x 8 mm ID tube. The compressed air was connected to both suction and blowing systems using 12 mm Tee fittings (Figure 3-12b). In both systems, a flow control valve (Figure 3-12c) was connected to control the mass flow rate. In the suction system, a Venturi Vacuum generator (Figure 3-12d) was used to create a vacuum from the air compressor. Then the flow velocity was measured using a static pitot tube (Figure 3-12e).

Furthermore, in order to ensure the validity of this process, a calibration point was implemented using a Venturi meter, Omega flow meter, and Pitot - static tube (Figure 3-12e). This means the three devices were connected in series on the same flow stream. Their readings were recorded and compared (refer to Appendix A-3). A digital manometer (Figure 3-12f) was used to measure the pressure difference between the stagnation pressure and static pressure. After that, the suction and blowing sections were attached to two separate equal push-in fittings (Figure 3-12g). This is to ensure that the flow will separate into three branches in each technique, with an equal flow rate. These branches will extend to blowing and suction slots, on both sides of the model (Figure 3-13), through a ball valve (h) that is used to control which slot(s) should be opened or closed.
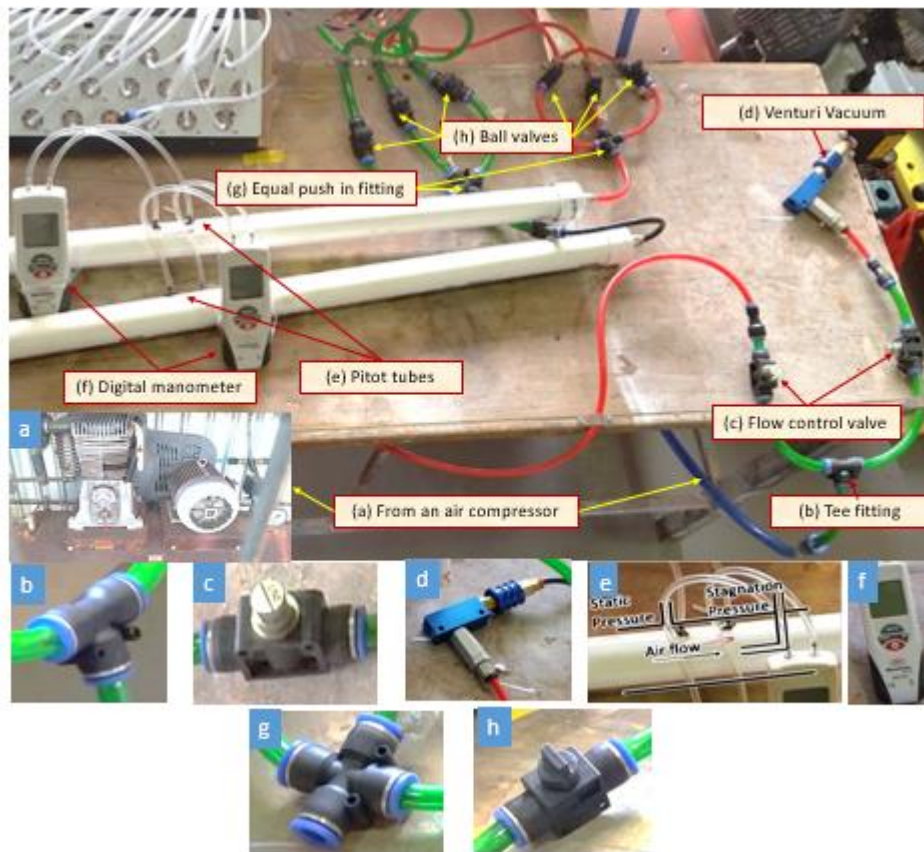
Figure 3-12: The various components of a blowing and suction system and how they interconnect
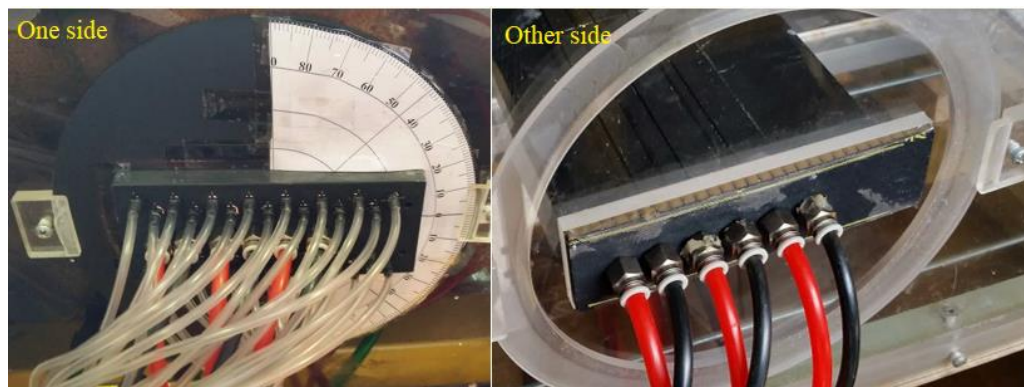
Figure 3-13: The test section with models from both sides

3.4 The pressure measurement system

Figure 3-14 shows the equipment which was used to measure the various pressures in the model. The multi-tube manometer was used to measure the head pressure. The pressure tappings in the model were connected to the flexible tubes using a set of double joiner 5 mm screws. The tubes were then connected to a manifold plate to transfer later to large-diameter pipes connected to a multi-tube manometer. This multi-tube manometer has 36 tubes (each 600 mm in height) divided into two parts. The pressure openings of the left-hand side of the manometer were used for the upper surface of the aerofoil model. At the same time, the pressure openings of the right-hand side were used for the lower surface. Points 1 to 15 were designated as pressure distribution points for the upper surface. The remaining points were designated for the lower surface. Specific points were connected directly to the manometer without firstly being connected to the manifold plate. This was because the manifold plate only consisted of 25 points, and there were 30 points measured.
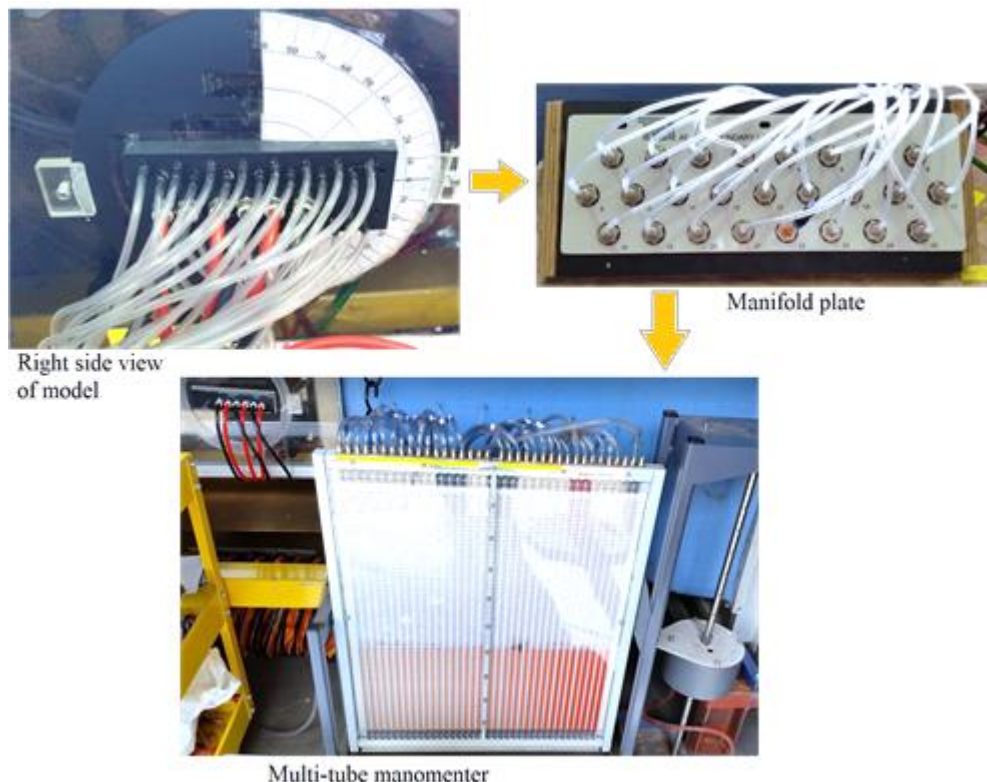
Figure 3-14: The connection equipment for the pressure system used in this project

3.5 Aerofoil profile models design and manufacturing

As mentioned previously, the NREL S822 and NREL S823 aerofoils were selected in this project. These models were each manufactured with ABS material on a UP Box 3D printer (the models were printed with six external layers and 50% infill). Both models spanned the full width of the test section, and their dimensions were a 170 mm chord with a 300 mm span.

According to Schubel and Crossley (2012), the wind turbine blade can be divided into three areas (Figure 3-15), the blade root, the mid-span, and the tip blade. In the last two areas, the lift-to-drag ratio should be maximised. So, the tests were carried out for S822 aerofoil with AFC, while for S823 aerofoil, operations were performed without AFC (Figure 3-16).
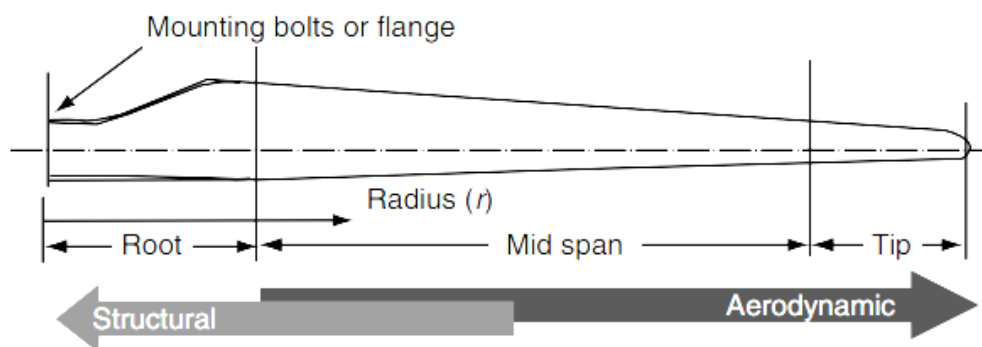
Figure 3-15: The blade regions (Schubel and Crossley, 2012)
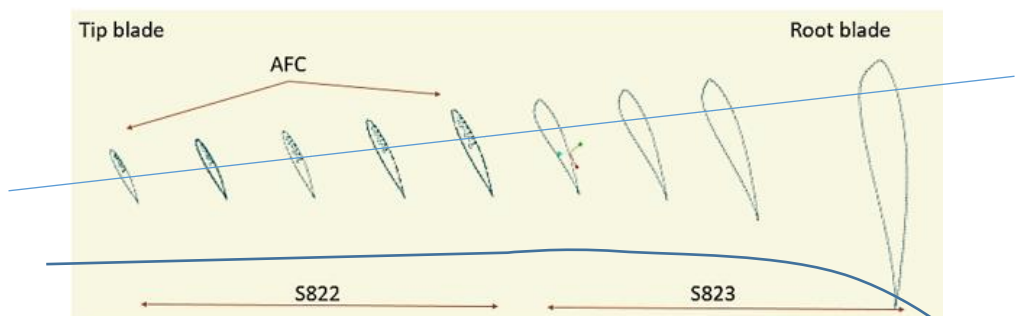
Figure 3-16: The distribution of selected aerofoils on the base of Table 2-1 in chapter 2

Using the suction technique, with three slots, 1 mm wide were incorporated while using the blowing technique, three slots, 0.5 mm wide were incorporated, as shown in Figure 3– 17. Suction process slots were designed perpendicular (90º) to the tangent line of the upper surface of the profile model. However, blowing slots were designed to be angled at 30º with the aerofoil tangent. The reason for this was to provide some momentum in the direction of the main flow.

Blowing method is denoted by 'B' and suction by 'S'. Slots were numbered sequentially; for instance, the number '1' was taken to be the first slot nearest to the leading edge. Holes of 8 mm diameter were used to connect the slots to both sides of the model.

In both techniques, the flow separation may or may not be mitigated, depending on several factors: (1) the position of the slot(s); (2) The method of using slots in the operations of blowing and sucking (i.e. how many slots should be used in each process); and (3) blowing and suction velocities through the slots. Subsequently, this will affect the performance of the blade and hence ultimately the performance of the wind turbine itself.
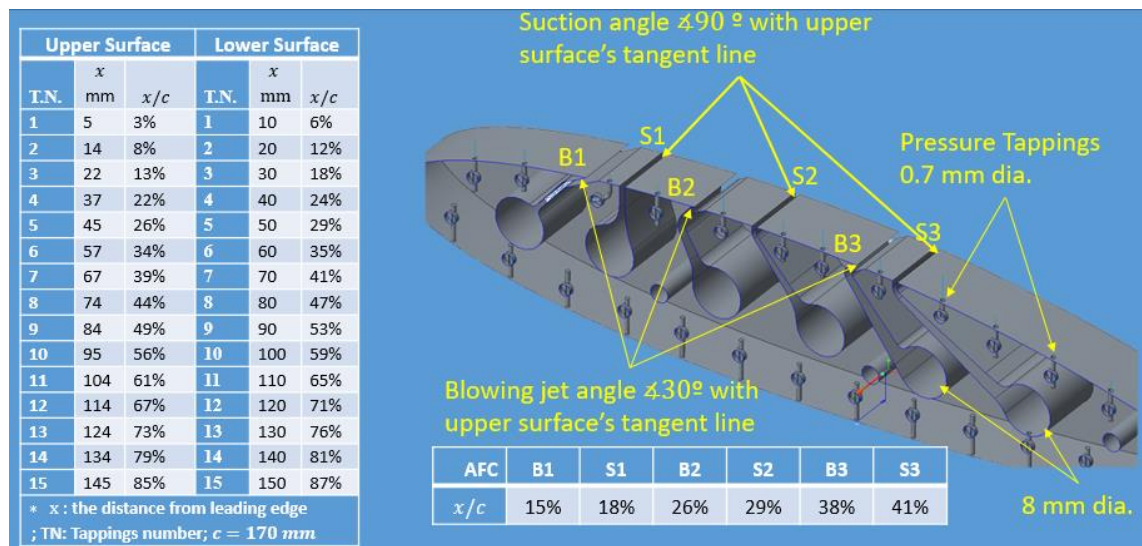
Figure 3-17: The NREL S822 aerofoil model: blowing (B) and suction (S) slots, with pressure tappings designs.

53

The static pressure across the aerofoil profile was measured through 0.7 mm diameter holes, acting as pressure tappings, in the centre of the model's span. Fifteen holes were placed on the upper surface and 15 on the lower surface of the model. The distances of pressure tappings from the leading-edge are listed in (Figure 3-17). Therefore, to facilitate construction, the pressure tapping on the upper surface were located in different positions to those on the lower surface. Holes with a diameter of 0.7 mm were connected vertically to meet with tubes with a diameter of 2 mm and then extend horizontally along the span. The designs of the proposed aerofoil models used in this project are illustrated in Figure 3-18.
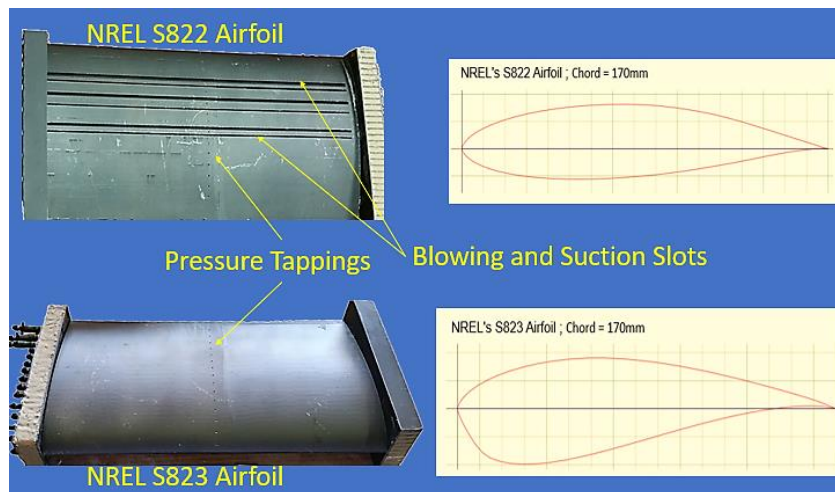
Figure 3-18: The NREL S822 and S823 aerofoil models.

3.6 Summary

The practical settings required for the experimental tests are explained in this chapter. The prototypes and some parts of the wind tunnel were designed by using Creo Parametric6.0.0.0 and then manufactured by a 3D printing machine. The models manufactured are aerofoils of S822, S823 and the slots required for suction and blowing operations are made only on S822 aerofoil model.

The experimental section of the wind tunnel was made of Perspex material, making it convenient to fit the prototype and make it able to rotate inside the working area during the experiments. Blowing and suction system, the pressure system, and the smoke system have been configured, calibrated and connected to form the integrated system prepared for the test.

CHAPTER 4: AEROFOILS SIMULATION SETUP BY CFD

4.1 Introduction

Recent progress in computers has made it easy to predict fluid behaviour and the effects of pressure and velocity on fluid flow. Computational fluid dynamics (CFD) is an ideal way to understand the real events of fluid flow. It is also considered an appropriate tool for detecting possibilities for improving the performance of a wind turbine, so CFD is a preferable option to conducting multiple practical experiments to achieve the best performance and this, in turn, reduces both cost and time. No matter what type of software is utilised in the simulation, the underlying processes are identical.

The purpose of this chapter is to verify the simulations using 'ANSYS FLUENT 2020 R1 ACADEMIC' by performing the necessary tests to ensure that numerical errors are minimised. Two aerofoil profiles (NRELS822 and NRELS823) were selected to be simulated in the simulation setup. The simulation setup structure was planned, as illustrated in Figure 4-1.
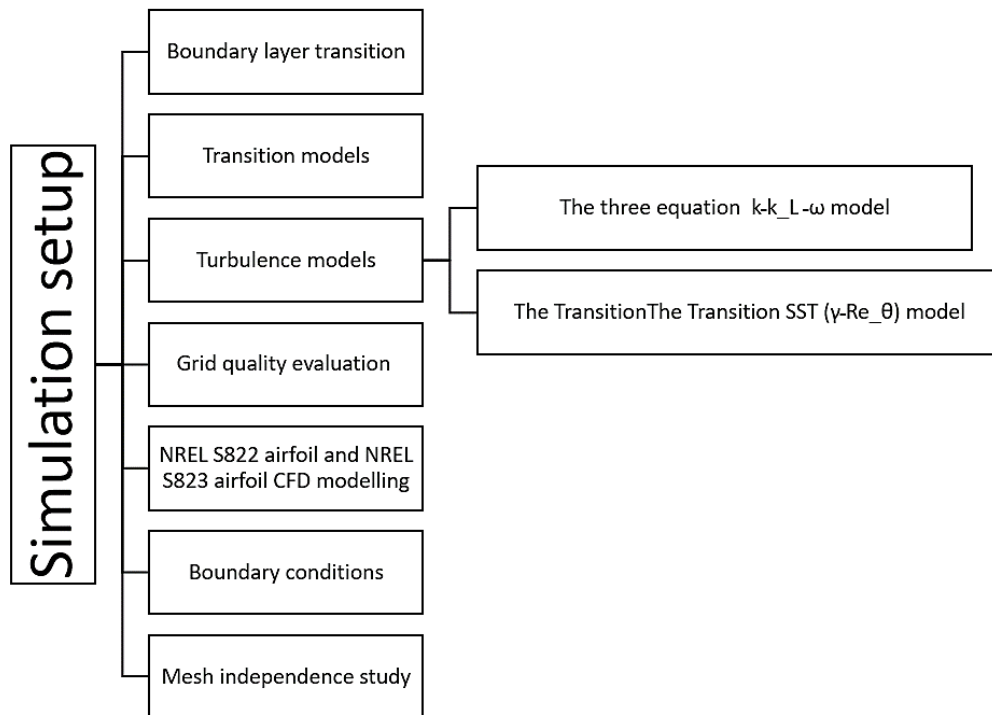
Figure 4-1: The process of the simulation setup

4.2 Boundary layer transition

According to Sheng (2017, p. 1-8), the transition of the boundary layer is described in several varying modes, including natural transition; separation induced transition; bypass transition; and reverse transition. The transition across flat surfaces is considered a natural transition if the surface is smooth, and the intensity of free-stream turbulence is less than 1%. The natural transition is characterised by generating two-dimensional waves called Tollmien-Schlichting (T-S) waves. If the intensity of free-stream turbulence is greater than 1%, the T-S waves can be bypassed, and in this case, the transition is called Bypass Transition. In incompressible flow simulation, the turbulence intensity is taken to be 5% (Ali (2014). The transition caused by the effect of the reverse pressure gradient, which results in a laminar separation bubble (LSB) formation at the leading edge, is called the separation-induced transition. When an acceleration of flow occurs either at the leading edge (at the upper surface of the aerofoil), or the trailing edge (at the lower surface of the aerofoil), Reverse Transition occurs in which the turbulent flow turns into a laminar flow.

However, there are flow-related parameters that affect the transition process. Those are free-stream turbulence, pressure gradient, and the roughness of the surface. These parameters have helped scientists develop theories and models for the transition. The first parameter identified is free-stream turbulence, which affects all transition modes, for example, at higher levels of turbulence, bypass transmission occurs, which affects the transitions which occur due to flow separation. In addition, in certain circumstances, it determines whether the LSB state explodes or reattaches to the surface again as turbulent flow. The second parameter identified is the pressure gradient, which may influence the state of the onset of the transition or the flow separation process. A positive pressure gradient results in transition delay, while the reverse gradient expedites flow separation to occur. The third parameter relates to surface roughness. In the case of smooth surfaces, the natural transition occurs, while bypass transition may be expected to occur when the surface roughness is high.

4.3 Transition models

Laminar-Turbulent Transition assisted greatly with Low Reynolds' predictions. LSB and its effect on the occurrence of the stall were investigated through the transitions processes (Serdar Genç and Kaynak, 2009). Sheng (2017, p. 9-20) classified transition modelling methods into three groups: The first group is based on stability theory for the natural transition prediction; the second group is based on Reynolds-averaged Navier–Stokes equations (RANS) for bypass and separation-induced transition predictions; The third group consists of two methods, Large Eddy Simulation (LES) and Direct Numerical Simulation (DNS), which are each capable of providing detailed transient results to different levels of accuracy.

In those methods based on stability theory (first group), anticipating the start of Natural Transition occurs in low Free-Stream Turbulence conditions. This category consists of the e^N method and the parabolized stability equations (PSE). Most unstable disturbances are represented by the total growth factor (N). With local parallel flows, the e^N method is based on the theory of linear stability. Furthermore, the growth of the disturbance amplitude is calculated from the neutral point of the boundary layer to the position of transition. The use of the e^N method includes three stages: for a given

geometry, finding the laminar velocity and temperature profiles, at various stream-wise areas, is considered as the initial step. The subsequent advance is to determine the local growth rates of the most unstable waves among all velocity profiles. The last advance is to calculate the transition onset position dependent on the local growth rates incorporated along each streamline. However, surface roughness-induced and bypass transition are not predicted by the e^N method, due to the hypothesis of local parallel flow, which is considered a significant problem concerning this method.

Based on stream-wise distance, the PSE method calculates the mean flow, wave numbers and amplitude functions in order to predict the transition onset location. Moreover, the development of disturbance waves (both linear and nonlinear) can be solved by PSE. However, in three-dimensional (3D) flow, since the direction of flow is not always aligned with the surface of the body, it will be challenging to perform flow calculations using PSE because it is necessary to evaluate the growth of the turbulence amplitude along the streamlines. More detailed information about transition models can be found in (Malalasekera, 2007).

4.4 Turbulence models

Recently, modern prediction models have been developed which simulate the transition from laminar to turbulent flow at low Reynolds numbers, by using URANS and RANS based on CFD code, and on the other hand by using empirical correlation-based methods. Serdar Genç et al. (2012) claimed that two-dimensional models showed success in predicting transitions but that the wall damping terms limited their usefulness. Nevertheless, a brief description of the two models was listed as follows:

4.4.1 The three equation k-k_L-ω model

The standard k-ω model was extended to the three-equation k-k_L-ω model (Wilcox, 2006) and Serdar Genç et al. (2012). The aim of this development (in the k-k_L-ω model) was to predict the transition onset and its length. So, in addition to k-ω transport equations (the turbulent kinetic energy k and

specific dissipation rate ω), it (k-k_L-ω model) solves the transport equation of laminar kinetic energy (k_L). The equation of k_L was used to predict pre-transition processes within the boundary layer that occur as a result of the low-frequency and large-scale velocity fluctuations. Furthermore, it takes into account the natural and bypass transitions. In other words, the turbulent energy near the wall area can be divided into two energies, one of which is a small scale turbulent energy which helps to produce turbulence and the other is a large scale turbulent energy that contributes to the formation of the laminar kinetic energy (Serdar Genç et al. (2012).

4.4.2 The Transition SST (γ-Re_θ) model

The Transition SST (γ-Re_θ) model is used to predict an onset of transition and its length. It can predict the natural, bypass, and separation-induced boundary layer transitions (Rezaeiha et al., 2019). The Transition SST (γ-Re_θ) model, which was developed by (Langtry and Menter, 2009) , is based on the coupling of the SST k-ω equations, which is/are used to predict the onset and duration of transition, with two other transport equations. One of these equations is for intermittency γ (Eq. 4-1), while the other (the momentum-thickness equation Re_θ) is to predict the beginning of the transition (Eq. 4-2).

$$\frac{\partial(\rho\gamma)}{\partial t} + \frac{\partial(\rho U_j \gamma)}{\partial x_j} = P_{\gamma 1} - E_{\gamma 1} + P_{\gamma 2} - E_{\gamma 2} + \frac{\partial}{\partial x_j}\left[\left(\mu + \frac{\mu_t}{\sigma_\gamma}\right)\frac{\partial\gamma}{\partial x_j}\right] \qquad \ldots\ldots\ldots\ldots 4\text{-}1$$

$$\frac{\partial(\rho \tilde{R}e_{\theta t})}{\partial t} + \frac{\partial(\rho U_j \tilde{R}e_{\theta t})}{\partial x_j} = P_{\theta t} + \frac{\partial}{\partial x_j}\left[\sigma_{\theta t}(\mu + \mu_t)\frac{\partial\tilde{R}e_{\theta t}}{\partial x_j}\right] \qquad \ldots\ldots\ldots\ldots 4\text{-}2$$

In the first equation, γ lies between zero and one, where when it is zero, the flow is considered fully laminar, whereas when it is one, the flow is considered fully turbulent, and the value between zero and one represents the state of transition. According to Sheng (2017, p. 21-54), γ can be interpreted as a measure of the probability of turbulent flow occurring over a fraction of the time during the transition.

In a study on the performance of a vertical axis wind turbine, conducted by Rezaeiha et al. (2019), seven disturbance models in addition to inviscid modelling were tested (Table 4-1), and they were compared with experimental studies. The unsteady Reynolds-Averaged Navier-Stokes (URANS) were used in this analysis. The study showed that the Spalart-Allmaras (S-A) model is unable to predict the high rotational characteristics of the wind turbine blade, resulting in incorrect predictions of turbine performance. Furthermore, they showed that using the realizable k-ε and RNG k-ε models, the prediction of a stall occurs only at the trailing edge of the blade aerofoil, and the occurrence of stall cannot be predicted as seen in experimental tests. This, in turn, leads to fundamental differences in the prediction of the aerodynamic performance of the aerofoil. Finally, the prediction of the shed of the stall vortex did not occur via the k-k_l-ω transition model. For each of the above reasons, an incorrect prediction in the performance coefficient of the wind turbine occurs. However, the author stated that only the SST group (SST k-ω, SST k-ω with intermittency transition model and Transition SST (γ-Re_θ) model) was suitable for modelling, as this was the only group in reasonable agreement with the practice tests.

Table 4-1: List of turbulence models according to a number of equations and transition models (Rezaeiha et al., 2019)

Turbulence Models	Number of equations.	Transition modelling
Inviscid model	0	No
Spalart-Allmaras model	1	No
RNG k-ε model	2	No
Realizable k-ε model	2	No
SST k-ω model	2	No

SST k-ω with intermittency transition model	3	Yes
Transition k-k_l-ω model	3	Yes
Transition SST (γ-Re_θ) model	4	Yes

In another study conducted by Aftab et al. (2016), a numerical analysis was performed on the NACA4415 aerofoil to predict a laminar separation bubble (LSB) at Reynolds number 120,000. In this study, several turbulence models were used as follows: Spalart-Allmars (S-A), SST k-ε, Intermittency (γ) SST, k-k_l-ω, and γ-Re_θ SST. The accuracy of these models was determined by comparing them with the results of previous experimental tests (Figure 4-2). The results stated that Spalart-Allmars was unsuitable for an angle of attack higher than or equal to 6º. Furthermore, it showed that SST k-ω, Intermittency (γ) SST, and k-k_l-ω are unsuitable to predict LSB. Nevertheless, the author proved that the Transition SST (γ-Re_θ) model provides reliable results which are very close to reality compared to the other models investigated. It also accurately predicts the presence of LSB at low and high angles of attack. According to the results of those studies, the unsteady Reynolds-Averaged Navier-Stokes (URANS) with a model Transition SST (γ-Re_θ) model were used to predict low Reynolds number aerofoil transitions.
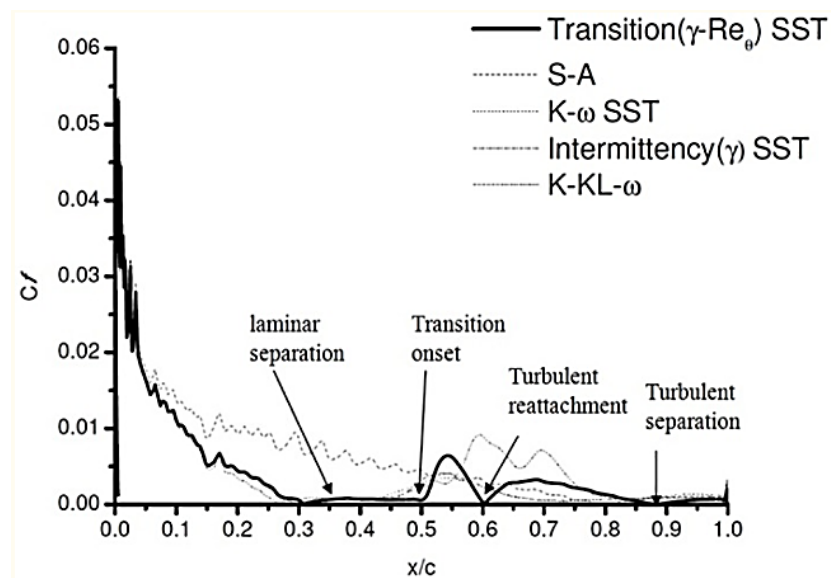
4.5 Grid quality evaluation

Table 4-2 was used to select a good quality mesh. One of these criteria is the Skewness of the grid. Grid Skewness is an appropriate indicator for assessing mesh quality. The large Skewness affects the accuracy of the grid. The mesh is unacceptable when Skewness approaches one. Mathematically, the Skewness can be expressed as:

$$Skewness = \frac{optimal\ cell\ size - cell\ size}{optimal\ cell\ size}$$

Where: the optimum cell size is defined as the size of an equilateral cell of the same circumradius.

The second criterion is the orthogonality quality of the grid, which relates to how close the angles of the adjacent faces or edges are to the optimal angle which is 90° for structured quadrilateral cells (quadrilateral faced elements) and 60° for unstructured triangular cells (triangular faced elements). The mesh is an excellent quality when the orthogonal is close to 1. A mesh which has low-quality values gives inaccurate simulation results as shown in Table 4-2. It is essential to determine the quality of the mesh accurately, but high quality means that the computing cost will be higher due to finer mesh. The meshing used in this project was based on unstructured triangular cells for both NRELS822 and NRELS823 aerofoils (Figure 4-3 and Figure 4-4, respectively).

Table 4-2: The mesh quality evaluation in terms of skewness and orthogonal quality
(Lim et al., 2018)

Cell Quality	Value of Skewness	Orthogonal Quality
Excellent	> 0.00 – 0.25	0.95 – 1.00
Good	0.25 – 0.50	0.70 – 0.95

Fair	0.50 – 0.75	0.20 – 0.69
Poor	0.75 – 0.90	0.15 – 0.20
Bad	0.90 – 1.00	0.00 – 0.14
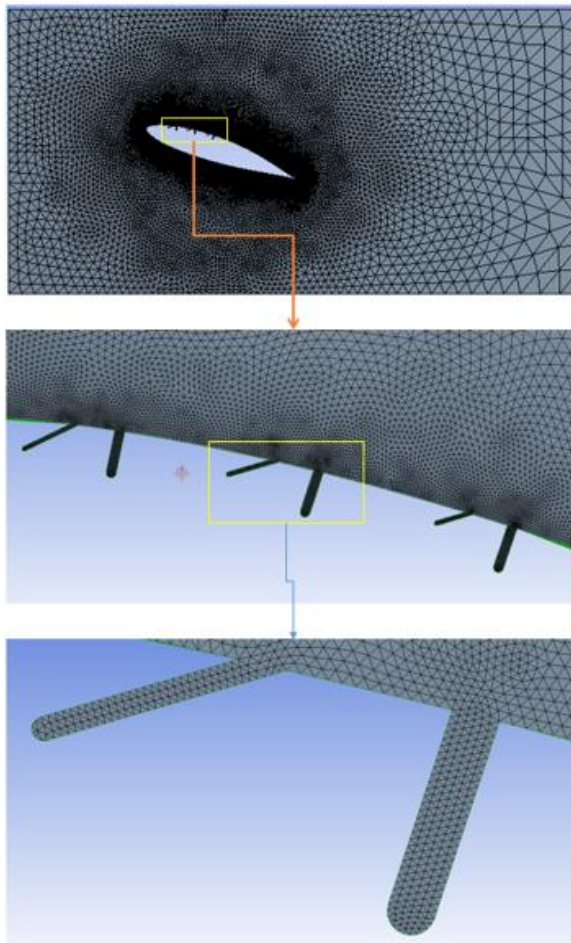
Figure 4-3: Triangular mesh with 94,269 cells and maximum mesh metric skewness of 0.58 for S822 aerofoil
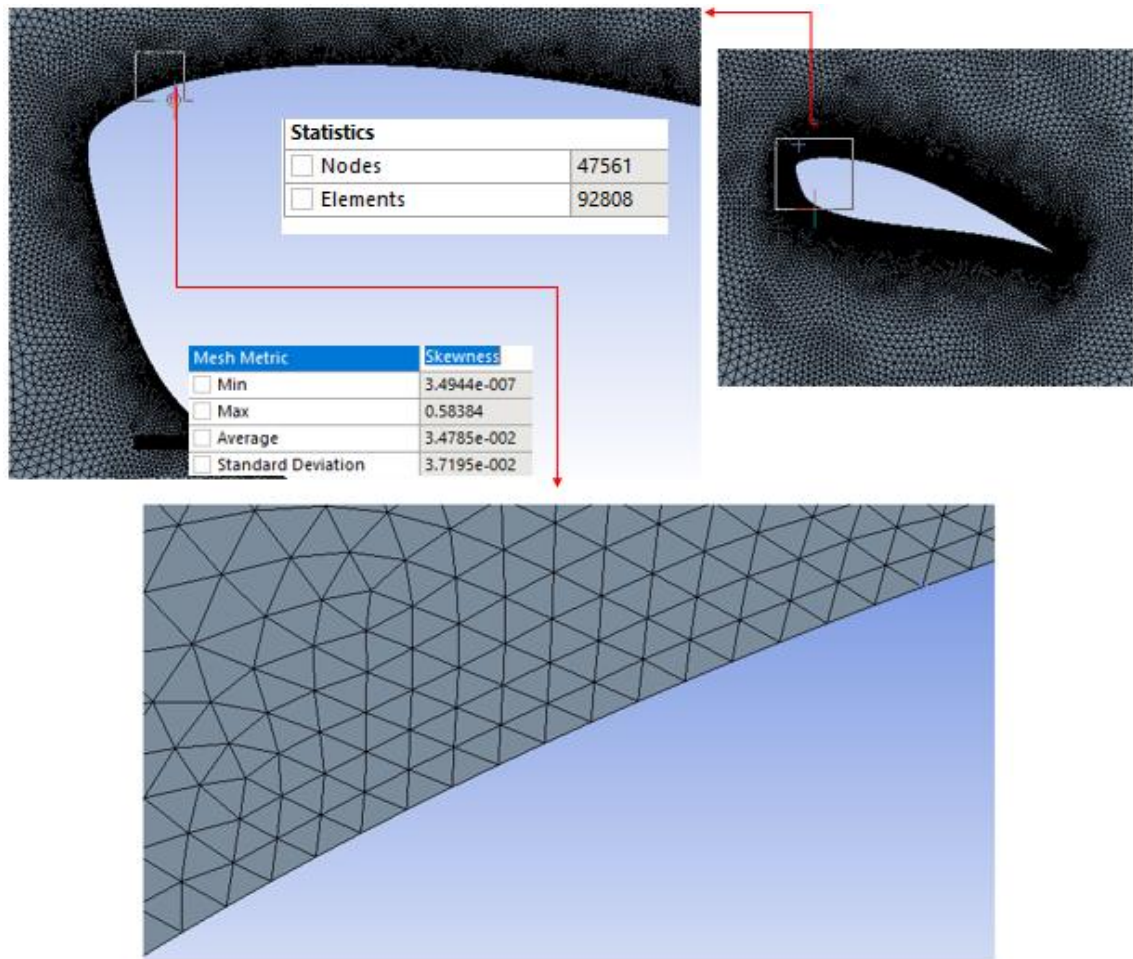
Figure 4-4: Triangular mesh with 92,808 cells and maximum mesh metric skewness of 0.56, for S823 aerofoil

4.6 NREL S822 aerofoil and NREL S823 aerofoil CFD modelling

In this section, a computational fluid dynamics (CFD) for a two-dimensional (2D) aerofoil was investigated. The 2D model was designed for a small wind turbine. Analysis of the NRELS822 aerofoil, being a small wind turbine, was simulated via CFD modelling. The simulation procedures can be summarised in four steps: the geometry process; the process of creating the mesh; the setup and the solutions process. For the Geometry process, the simulation models (S822 and S823 aerofoils) were imported from Creo Direct 6.0.0.0 into DesignModeler. The dimensions of selected aerofoils were designed according to Figure 3-17 (in Chapter 3). In the Mesh

generation process, the type of grid used was unstructured mesh consisting of 57,141, 2D triangular cells. A large number of triangular cells formed around the surface of the aerofoil, which enabled us to obtain accurate pressure gradient readings at the boundary layer in order to determine the state of flow separation and the adverse pressure gradient (APG). As the APG leads to flow separation, when separation expands, a stall occurs. Undesirable steep gradients occur near the leading edge, trailing edge and on the upper surface of the aerofoil at high angles of attack, so the grid size transit should be smooth. When moving away from the surface of an aerofoil, the resolution reduces as the mesh gradually becomes coarser.

4.7 Boundary conditions

The optimum computational conditions for aerofoil simulations can be shown in Table 4-3. The computational domain dimension (Figure 4-5) was designed based on the dimensions of the wind tunnel test section (Figure 3 -5 in Chapter 3). In the test section domain, the accuracy of the boundary conditions is imperative in order to obtain meaningful values. The boundary condition was determined, as shown in Figure 4-5. At the inlet, the velocity and gauge pressure were defined, the inlet velocity was taken to be 15.8 m/s; while at the outlet, and the gauge pressure alone was defined. The gauge pressure at the inlet and outlet were made identical. According to Bernoulli's equation and the continuity equation, the static pressure at the inlet and outlet of the test section was taken to be 149.4 Pa. This value was almost identical to the static pressure of the wind tunnel test section (-156 pascals) see Appendix B-1.

Table 4-3: Optimum computational conditions for aerofoil simulations

Aerofoils	NRELS822 and NRELS823 aerofoils
Simulation Type	Unsteady Simulation
Fluid Material	Air
Temperature	288 K

Kinematic Viscosity	$1.4607 \times 10^{-5} \, m^2/s$
Reynolds Number	179,489
Density	$1.225 \, kg/m^3$
Wind Speed at test section	15.8 m/s
Turbulent model	Transition SST (γ-Re_θ) (4eqn)
Inlet and outlet static pressure	-149.4 Pa
Inlet intermittency gamma (γ)	1
Inlet turbulent intensity	5%
The angle of attack (AoA)	18°
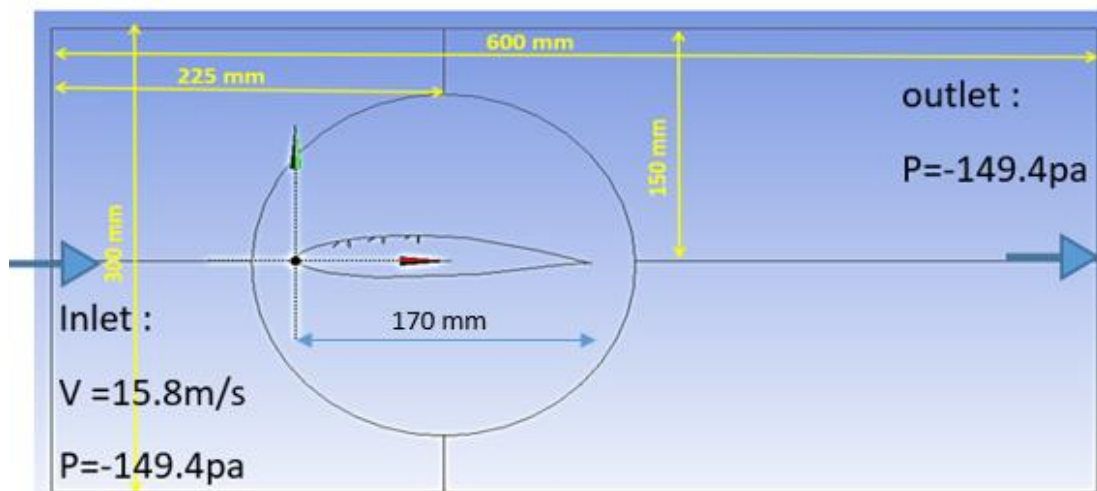
Figure 4-5: The computational domain of the NRELS822 aerofoil

4.8 Mesh independence study

Five grid levels were implemented (Table 4-4) using a coarse mesh of 22,491 to finer mesh of 144,027 cells to identify the optimal mesh (numerically accurate without excess computational time). In Case 4 (with 94,269 cells), the values of lift and drag coefficients (Figure 4-6) were not affected by increasing the number of cells. Therefore this model was considered suitable for simulation. The Skewness and Orthogonal quality, as a Mesh Metric, was used to predict the Mesh quality. In Appendix B-2, Histograms for mesh quality (Skewness) of tested cases are listed.

Moreover, the pressure coefficient (in all cases) was combined in addition to the experimental test in one graph (Figure 4-7). The points in the fifth case appear to have mirrored the points in the fourth case. Therefore, as suspected, the results are unaffected by an increase in the number of mesh cells.

Table 4-4: The mesh quality of the NRELS822 aerofoil based on data obtained in Table 4-2

Tested Cases	No. of elements	Maximum element skewness		Minimum element orthogonal quality)	
Case 1	22,491	0.84	Good	0.37	Good
Case 2	33,116	0.64	Very good	0.50	Good
Case 3	57,141	0.58	Very good	0.54	Good
Case 4	94,269	0.56	Very good	0.67	Good
Case 5	144,027	0.55	Very good	0.67	Good
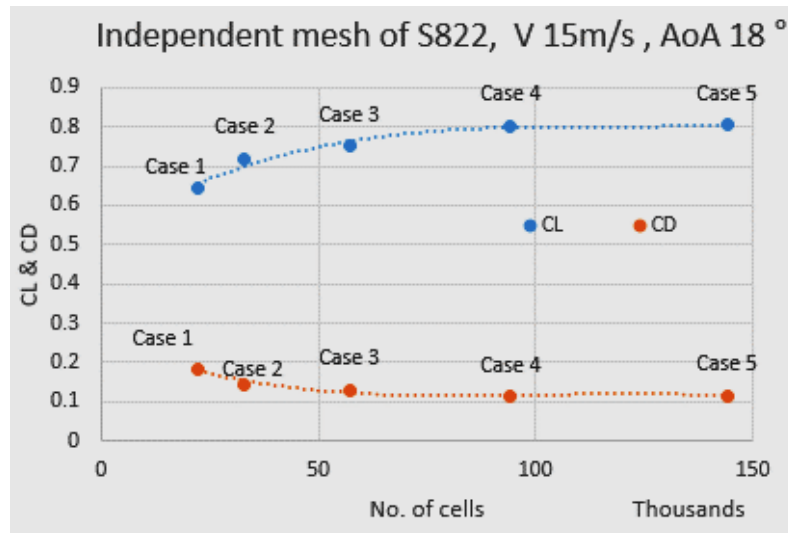
Figure 4-6: Mesh Independence study for S822 aerofoil at inlet velocity 15 m/s and AoA 18°
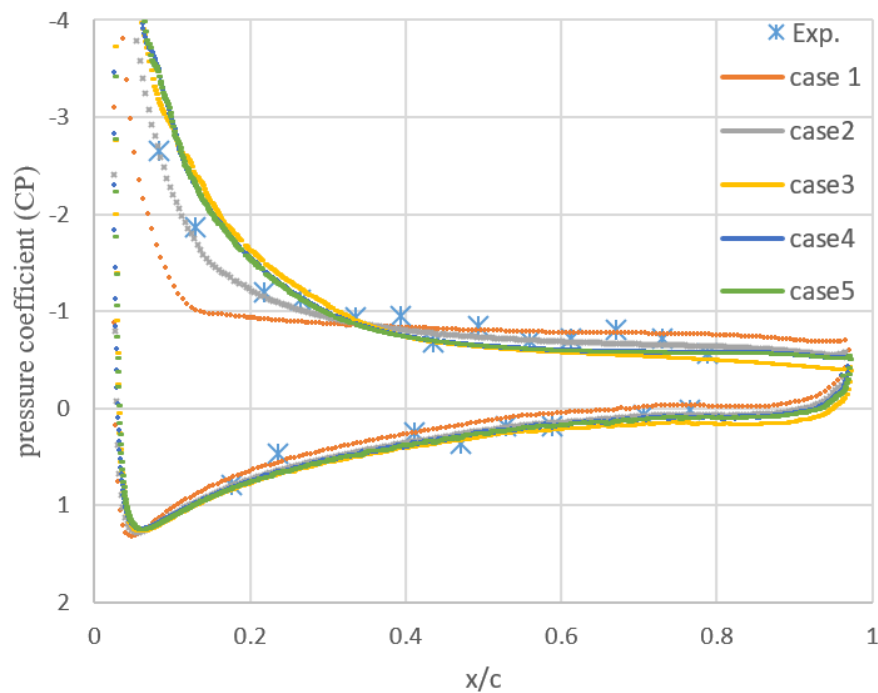
Figure 4-7: Distribution of pressure coefficient around the aerofoil for independent mesh cases, including the experimental test.

Case 4 was applied using the URANS turbulent models to predict flow separation by using the skin friction coefficient (of the upper surface of the model) along the model's chord (Figure 4-8). Certain models were unable to predict the flow separation, for

69

example, the SST k-ω with intermittency transition and the SST k-ω model. The remaining models demonstrated different locations of flow separation, but in the RNG k-ε model, the separation point value was close to the separation point value in the used model (Transition SST (γ-Re_θ) model).

The lift and drag coefficients were represented for the same case (Case 4) using the URANS models (Figure 4-9). The transition SST (γ-Re_θ) and RNG k-ε modes showed similar values for both lift and drag coefficients but differences in flow separation points.
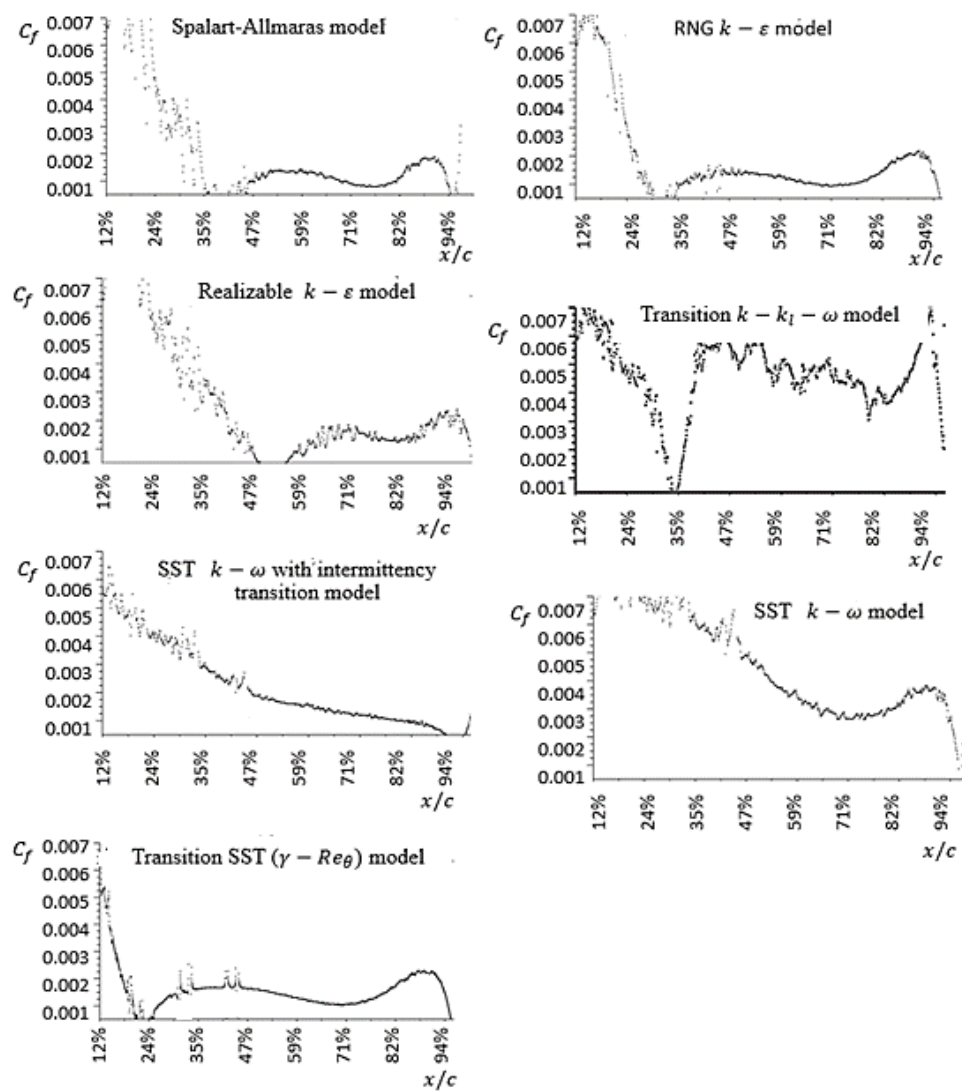
Figure 4-8: Skin friction coefficient over the upper surface of the NRELS822 aerofoil for the various URANS turbulent models

70

Turbulent models (URANS)

Legend: ■ CD ■ CL

Model	CD	CL
Transition SST ($\gamma - Re_\theta$) model	0.113	0.806
Transition $k - k_l - \omega$ model	0.430	1.111
SST $k - \omega$ with intermittency transition model	0.165	0.629
SST $k - \omega$ model	0.200	0.912
Realizable $k - \varepsilon$ model	0.120	0.832
RNG $k - \varepsilon$ model	0.113	0.806
Spalart-Allmaras model	0.159	0.915
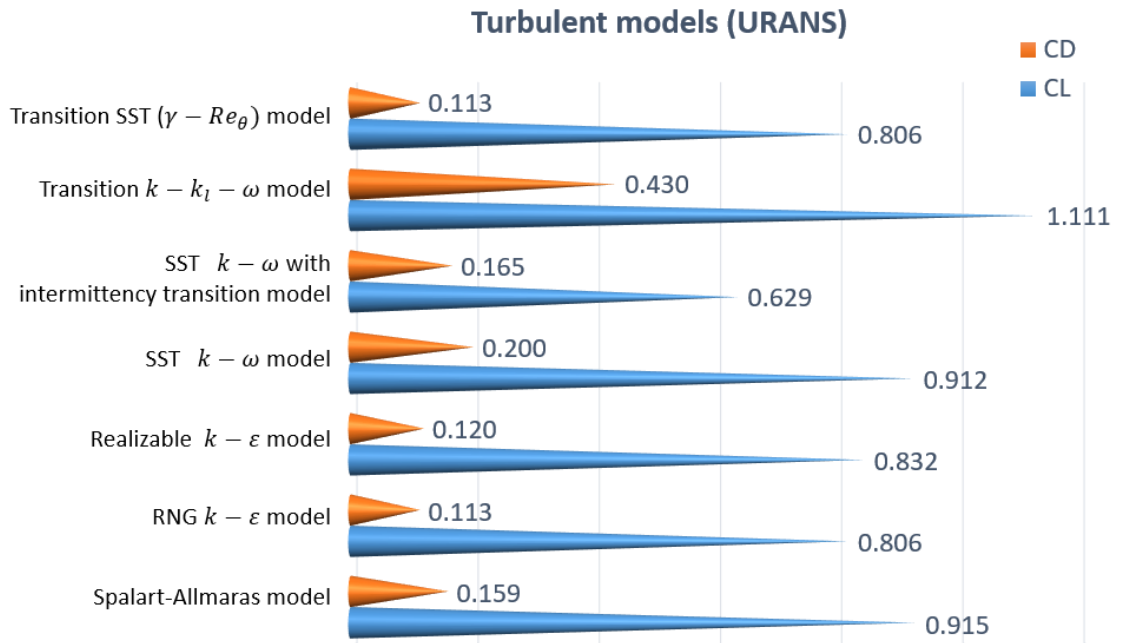
Figure 4-9: The lift and drag coefficients for the URANS turbulent models based on the Mesh in Case 4.

4.9 Summary

This chapter discussed the following aspects: the turbulence model used, the model's geometry, the mesh generation processes, the grid quality evaluation, the boundary conditions and the mesh independence. The transient SST (γ-Re_θ) turbulence model was selected (with its default values) as the best model, to predict the flow separation and the adverse effect of pressure gradient on wind turbine blade performance. Five grid levels were tested to determine the optimal mesh. Case four was selected as the best grid level with 94,269 cells. The lift and drag were used as a parameter to investigate the mesh quality. In case four, the lift and drag coefficients were not affected by the increase in the number of mesh.

71

CHAPTER 5: EXPERIMENTAL AND CFD RESULTS COMPARISON

5.1 Introduction

This Chapter identifies the results obtained from experiments conducted on, and simulated work fulfilled by the transient SST (γ-Re_θ) turbulence model via ANSYS Fluent 2020, R1 Academic. Figure 5-1 represented the main items of this chapter. The experimental tests and CFD results were performed on both S822 and S823 aerofoils. The primary purpose of conducting these tests was to validate the simulations (perform the necessary tests to ensure that the results simulated actual reality). However, the flow separation behaviour and pressure distribution will be determined as a second goal.
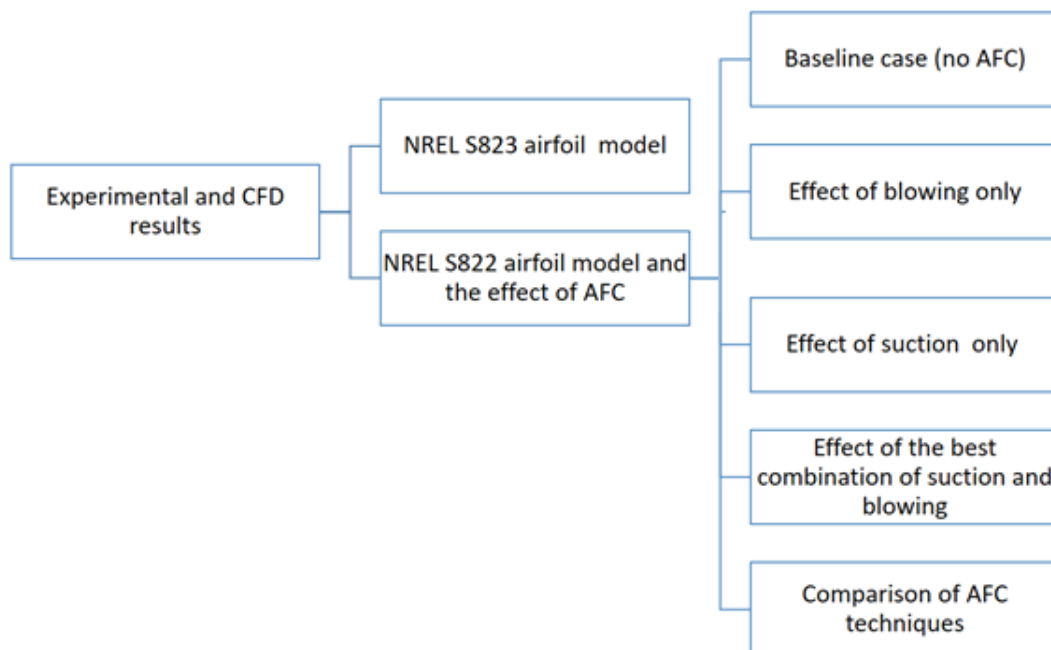
Figure 5-1: Chapter structure

In the experimental tests carried out in this study, in order to have a better view of the flow separation, a low inlet velocity (15.8 m/s) was adopted to avoid smoke dissipation (if using high inlet velocity) which would obstruct a clear view of the flow behaviour.

Furthermore, the multi-tube manometer (used to measure static pressure) was unable to provide readings when wind speeds at the test section were less than 10 m/s. Consequently, the wind speed adopted in the test section was specifically 15.8 m/s. Moreover, since flow separation occurs with high angles of attack (Figure 5-2), an angle of 18º was chosen to achieve the required flow separation and for conducting the visualisation process.
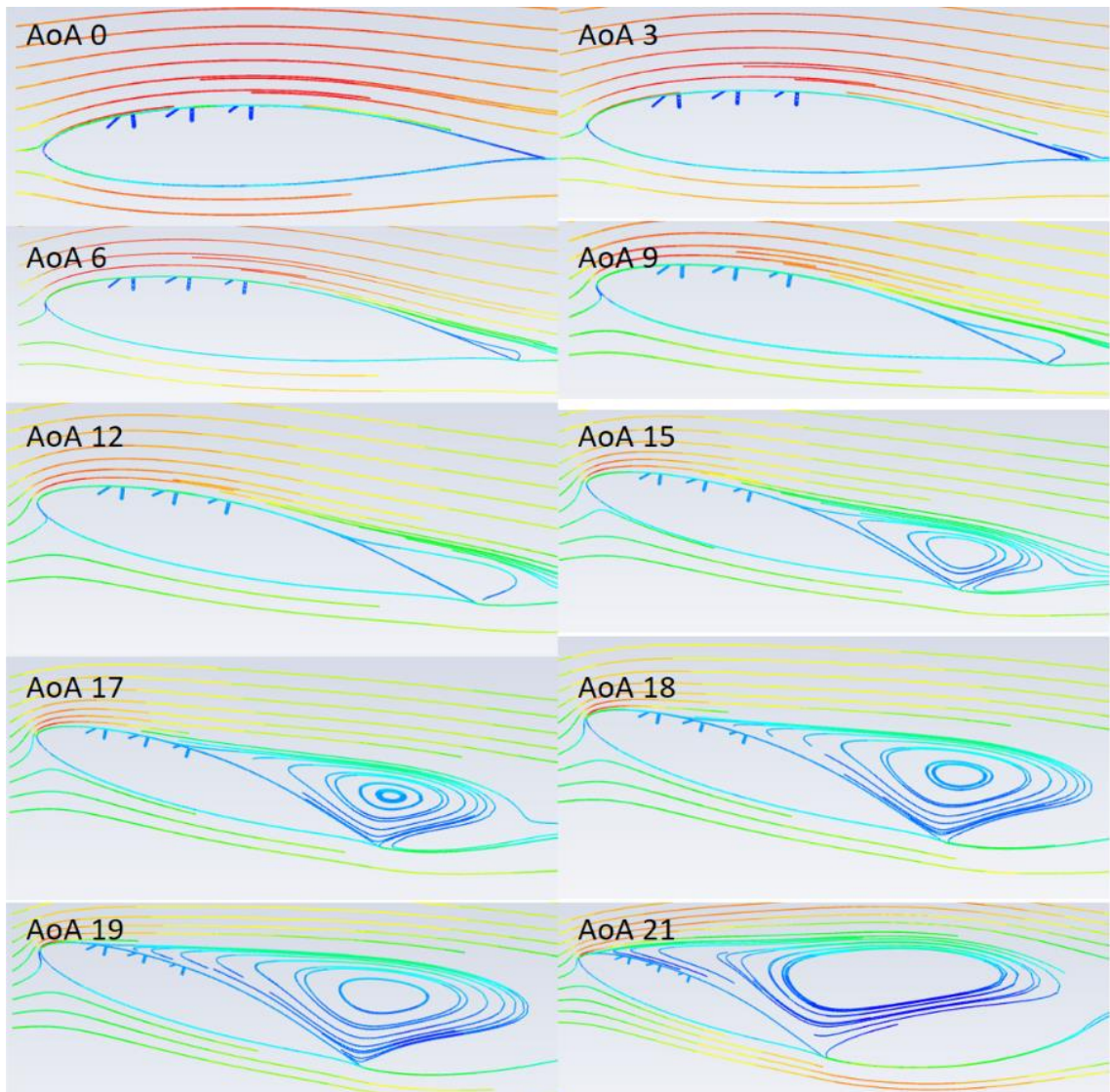
Figure 5-2: Flow separation of S822 aerofoil for angles of attack between 0 and 21° with an inlet wind speed of 15.8 m/s.

5.2 NREL S823 aerofoil model

Tests conducted using the NREL S823 aerofoil model were only intended to investigate the effect of velocity and angle of attack on the occurrence of flow separation. Active flow control (AFC) techniques were not applied to this type of aerofoil. The wind tunnel flow velocity is illustrated in Table 5-1.

Table 5-1: Wind tunnel velocities and angles of attack for NREL S823 aerofoil without AFC

V (m/s)	9 & 15			
AoA	6º	9º	15º	20º

Figure 5-3 shows the flow separation in the NREL S823 aerofoil model. The simulation results were mostly consistent with the experimental results. At both wind tunnel speeds, no flow separation was observed in angles of attack below 10º. Only a tiny detachment at the trailing edge of the aerofoil was noted, and this would not affect lift and drag forces. The separation increased with increasing angles of attack as well as with increasing wind tunnel speeds. Nevertheless, the increase in the flow separation capacitance is greater with the increase in the inlet velocity compared to the increase in the angle of attack.

Experimental test   CFD test

AoA 6º
V9 m/s

AoA 9º
V9 m/s

AoA 15º
V9 m/s

AoA 20º
V9 m/s

AoA 6º
V15 m/s

AoA 9º
V15 m/s
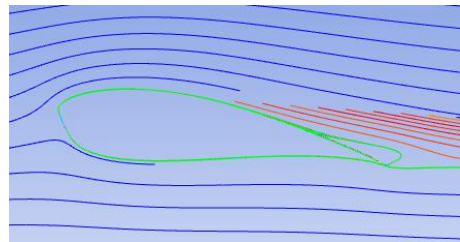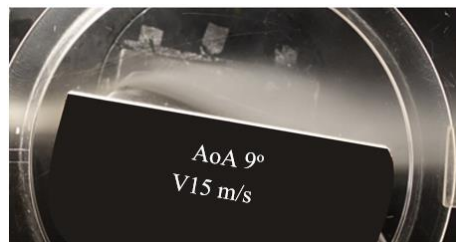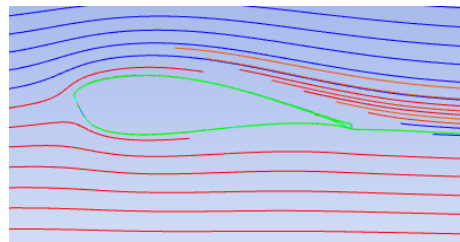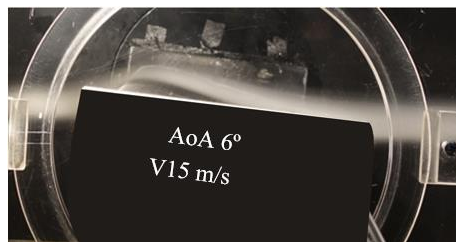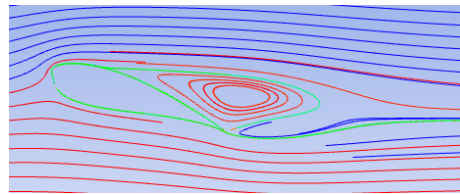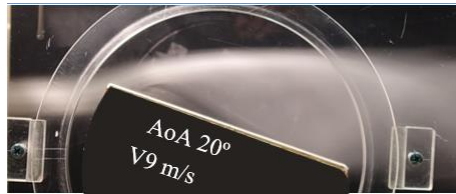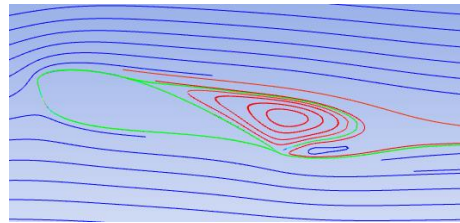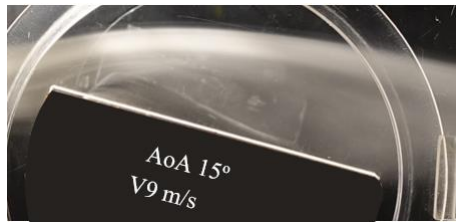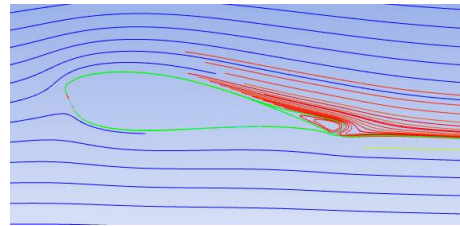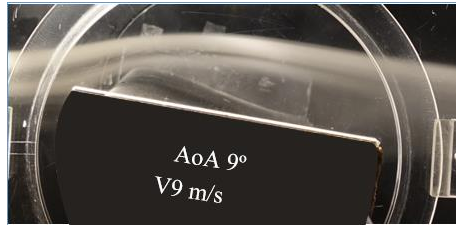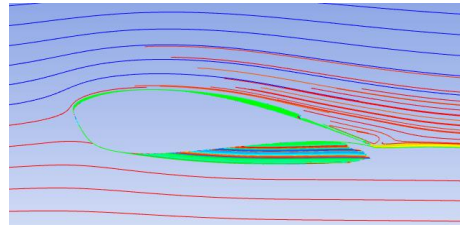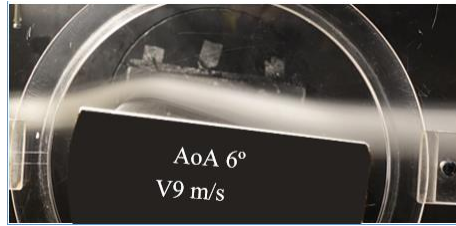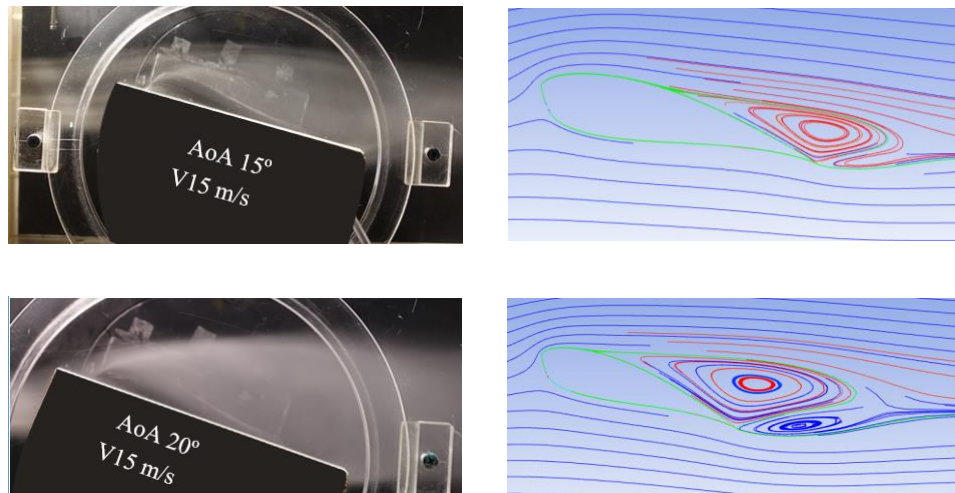
Figure 5-3: Flow visualisation of the NREL S823 aerofoil

5.3 NREL S822 aerofoil model and the effect of AFC

This section includes results from simulations and experiments which studied the effect of both suction and blowing processes in different locations when compared to the baseline case (without AFC).

In initial experimental tests, a loss in flow energy was noted. This was to be expected due to minor losses which occur due to the passage of air through valves, branches and bends as well as major losses due to friction between pipes and flow, and hence it became challenging to determine precise slots' flow speeds. Therefore, blowing/suction speeds were measured at the precise location of the slots using an anemometer before any tests were carried out. At the same time, digital pressure gauges were incorporated into suction and blowing system, which controlled the flow using a flow control valve. Through a combination of these two processes, suction and blowing speeds were regulated, so that the control valve was controlled, taking into account the reading of the digital manometer to reach the required suction or blowing speeds.

To avoid 3D flow effects, as suggested by Chawla et al. (2014), a wide slot is required for suction control. Therefore, the width of suction slot was designed to be slightly wider than blowing slot. However, to make the mass flow rate in suction process equal to the mass flow rate in blowing process, and according to the principle of the continuity equation, suction velocity was chosen to be lower than blowing velocity as demonstrated in Table 5-2. Therefore, the total mass flow rate for blowing is always the same as the total mass flow rate for suction.

Table 5-2: Speeds of blowing and suction techniques.

AFC location	Velocity / slot	No. of active slots
B1, B2, and B3	10 m/s	1
S1, S2, and S3	-5 m/s	1

Moreover, a visual imaging technique was used to see the effect of locations of suction/blowing techniques on aerofoil performance. Smoke visualization was used by Lee (2004) to observe the behaviour of flow around the aerofoil. In this chapter, the flow behaviour observed in the experiments is compared to the results from the corresponding simulation. In CFD, the velocity streamlines, pressure coefficient contours and velocity profiles were all collected in order to be presented in one graph. Furthermore, the experimental flow visualisation around the aerofoil model was also presented.

Moreover, the pressure coefficient (CP) distribution was shown for both the experimental work results and simulation results in a single graph. Furthermore, another parameter being presented was the skin friction coefficient (C_f). Finally, the trailing edge separation (TES) in both experimental and simulation was presented.

In experimental tests, to ensure the accuracy of the results, each operation was performed three times, then the standard deviation was calculated. The average of the three tested points and their standard deviation errors were represented in the pressure distribution graph.

77

The observed behaviour of pressure distribution, as shown in Figure 5-4 matches what one would anticipate should occur, which is higher pressure on the lower surface (the pressure surface) than the upper surface. Also, on the pressure surface, the maximum pressure was noted at a region near to the leading edge. As for the upper surface (suction surface), the pressure at the leading edge was minimal and then began to increase as the flow heads towards the trailing edge. The gradual increase in this pressure led to the occurrence of early separation, as the flow could not overcome the adverse pressure generated.
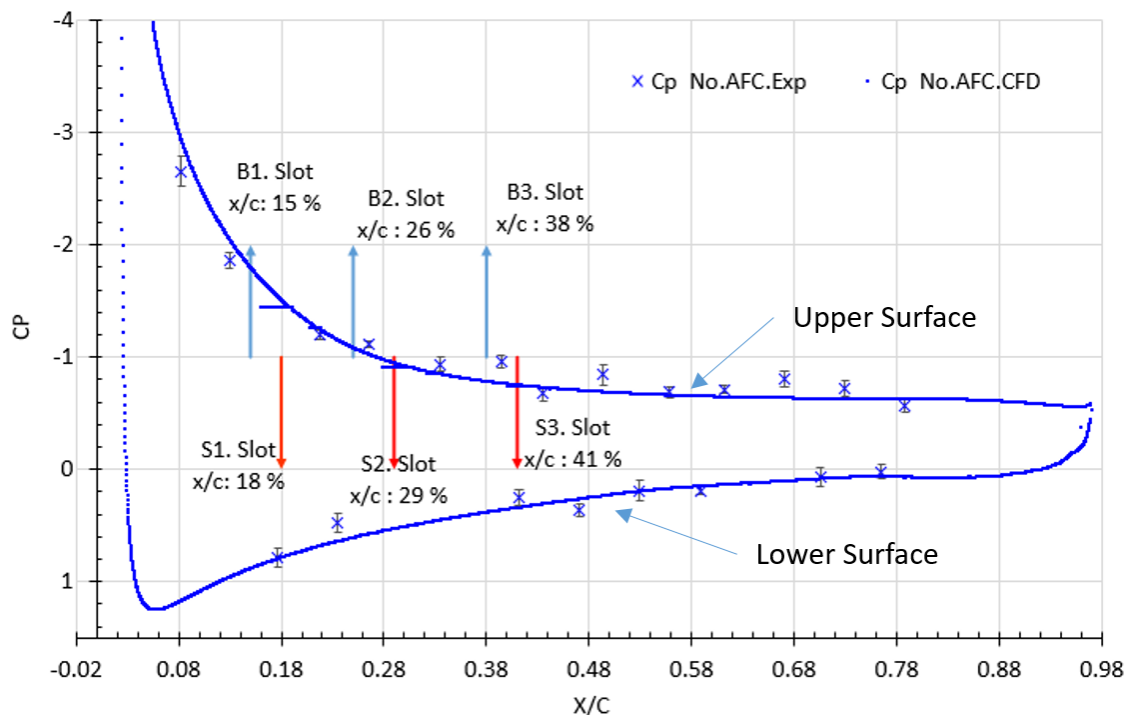
Figure 5-4: Pressure distribution of the baseline case around the aerofoil

AFC techniques were developed to conduct large-scale tests to optimise methods for mitigating the flow separation with blowing and suction techniques. Suction and blowing techniques were implemented for 14 different configurations, including the baseline case (without AFC). The behaviour of some examples was almost identical, therefore in order to avoid repetition, samples of these tests (containing mostly obvious results) were taken and explained. The reason was these tests are for validation, and using a single slot for validation is better than using two or three slots. Another reason for choosing these technologies over others is that they are considered the basic techniques that must be tested first, as the behaviour of each technique must be known

separately before combining it with another technology. Therefore, only eight configurations are discussed in this chapter; the remaining cases are listed in Appendix C . However, the lift-to-drag ratios for all cases are compared.

The eight techniques that will be discussed in this chapter are classified into three groups in addition to the baseline condition (Table 5-3). The first group included only blowing techniques (B1, B2, and B3) that exhibited only a single active slot. The second group included only suction techniques (S1, S2, and S3) that also exhibited only one active slot. The third group involves activating the best technique of blowing group (B3) with one at a time from the suction group (S1B3, S2B3, and S3B3).

Table 5-3: Blowing and suction configurations presented in detail

Baseline	blowing cases Only	suction cases Only	Suction and Blowing
no AFC	B1, B2, and B3	S1, S2, and S3	S1B3, S2B3, and S3B3

In this chapter, the effect of active control techniques (suction and blowing) on the adverse pressure gradient and hence on the delay of flow separation will be studied.

Finally, in the following subsections, the results for each case shown in Table 5-3 will be illustrated and discussed separately, before finally being discussed together. An individual explanation for each technique, LSB, separation region, and pressure distribution on the upper surface will be illustrated, compared with the baseline.

5.3.1 Baseline case (no AFC)

The first test was conducted without any active flow separation control techniques. In this chapter, the simulation tests were validated by experimental tests. The simulation results showed that the behaviour of the separation of the boundary layer, from the upper surface of the aerofoil, has similar characteristics with the experimental data. That is, there is a good agreement between the two. The flow separation point (SP) was noted at around $x/c = 0.23$ (Figure 5-5-d). This point plays an essential role in determining the progression or delay of flow separation points after AFC procedures,

as it is the baseline reference for all separation points after the application of flow control techniques. It (the baseline case) occurred before slot B2 (Figure 5-5-a), which is very close to the leading edge. In the area of TES (Figure 5-5-a), the velocity profile revealed that reverse flow occurred with a maximum velocity of -8.21 m/s. Also, the velocity gradient vector on the upper half of the TES vortex was more extensive than in the lower half. In experimental work, due to the 3D view, when smoke spread through the model's span (in the z-direction), the flow separation point was unclear (Figure 5-5-b).

The main reason for the occurrence of boundary layer separation is the adverse pressure gradient on the upper surface (Figure 5-5-a). The pressure at the lower surface of the aerofoil was higher than the atmospheric pressure ($CP = 0$). It gradually decreases towards the trailing edge, where it becomes approximately equal to atmospheric pressure after $0.92 \, x/c$. At the same time, it can be noted that the pressure in the upper surface of the aerofoil was lower than atmospheric pressure and continues to increase towards the trailing edge of the aerofoil. Moreover, after $0.4 \, x/c$, the pressure coefficient on the upper surface is approximately constant around the value of -0.6.

a V 15.8m/s ; AoA 18 ; without AFC

TE: Trailing Edge;   LE: Leading Edge;

SP: Separation point ;   CP: Pressure Coefficient;

Cf: Skin Friction Coefficient;

TES: Trailing edge Separation
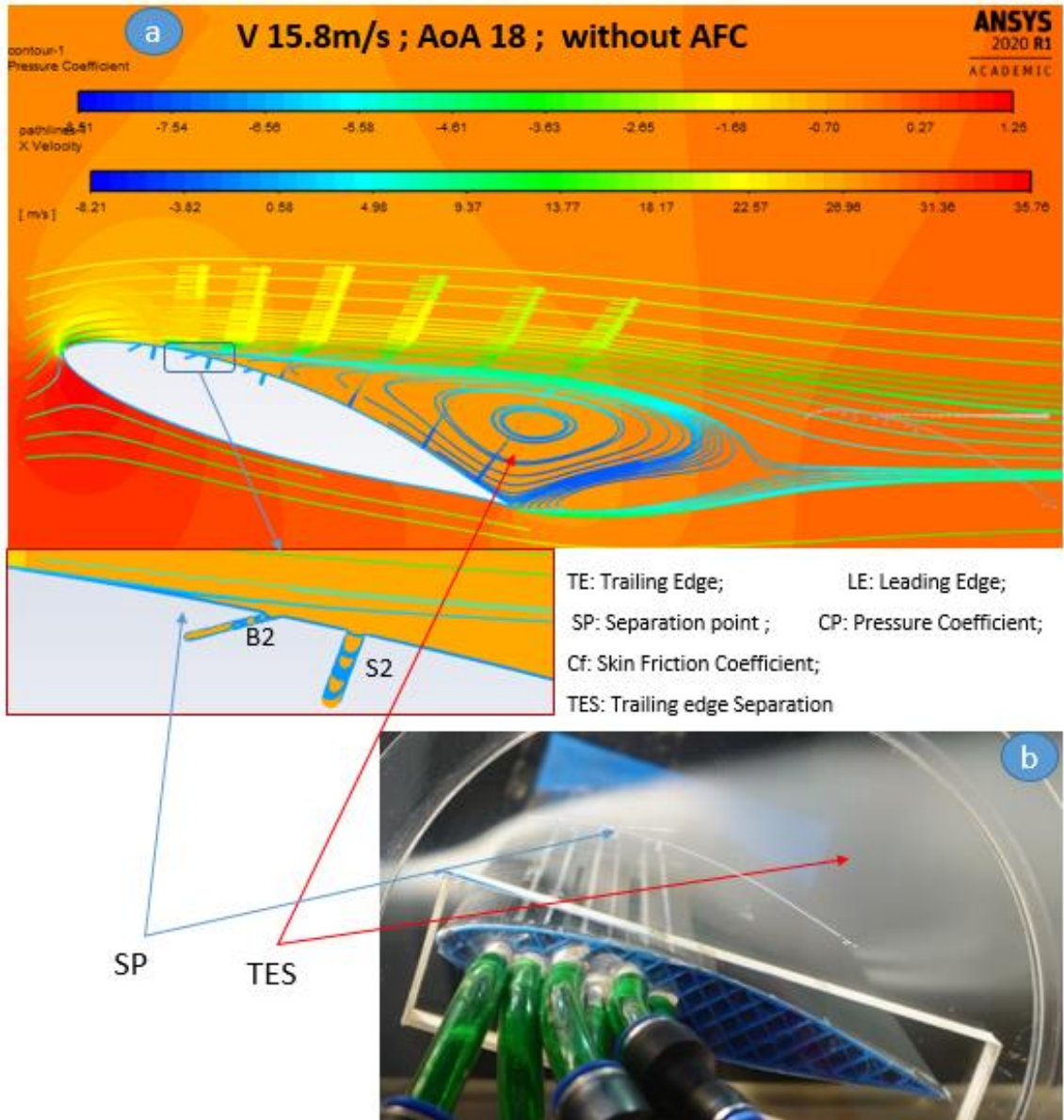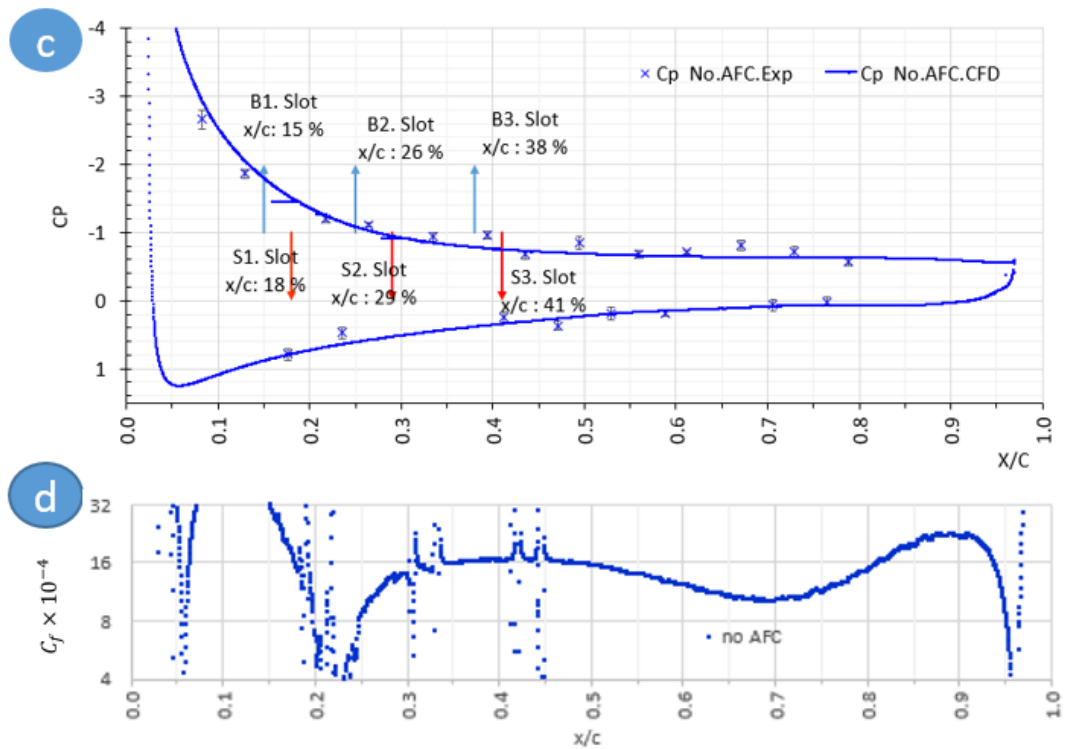
Figure 5-5: Results without AFC for flow inlet speed of 15.8 m/s and angle of attack of 18°. Flow visualisations around the aerofoil model for (a) simulation, showing streamlines and pressure contours; (b) experiment; (c) pressure coefficient (Cp) distribution for both experimental and simulation results; (d) skin friction coefficient (C_f) results of the baseline case (without AFC).

5.3.2 Effect of blowing only

The effect of blowing in slots B1, B2 and B3 will be discussed and compared with the baseline case. Figure 5-6 shows the results of the blowing technique at B1 ($x/c = 0.15$ (Table 3-1)). The separation point has moved slightly towards the leading edge ($x/c = 0.16$) (Figure 5-6-a and 5-d), so it (separation point) remains close to the leading edge. At the same time, an increase in pressure occurred from the leading edge to the point $x/c = 0.35$, followed by a slight decrease to the trailing edge compared to the baseline case (Figure 5-6-c). The separation in the baseline case occurred immediately after B1, and the angle of attack was high (18°) so B1 cannot help in delaying the separation. Furthermore, the momentum generated due to the blowing process, at an

82

angle of 30° with the upper surface of the model, will undoubtedly lead to an early separation compared to the baseline case.
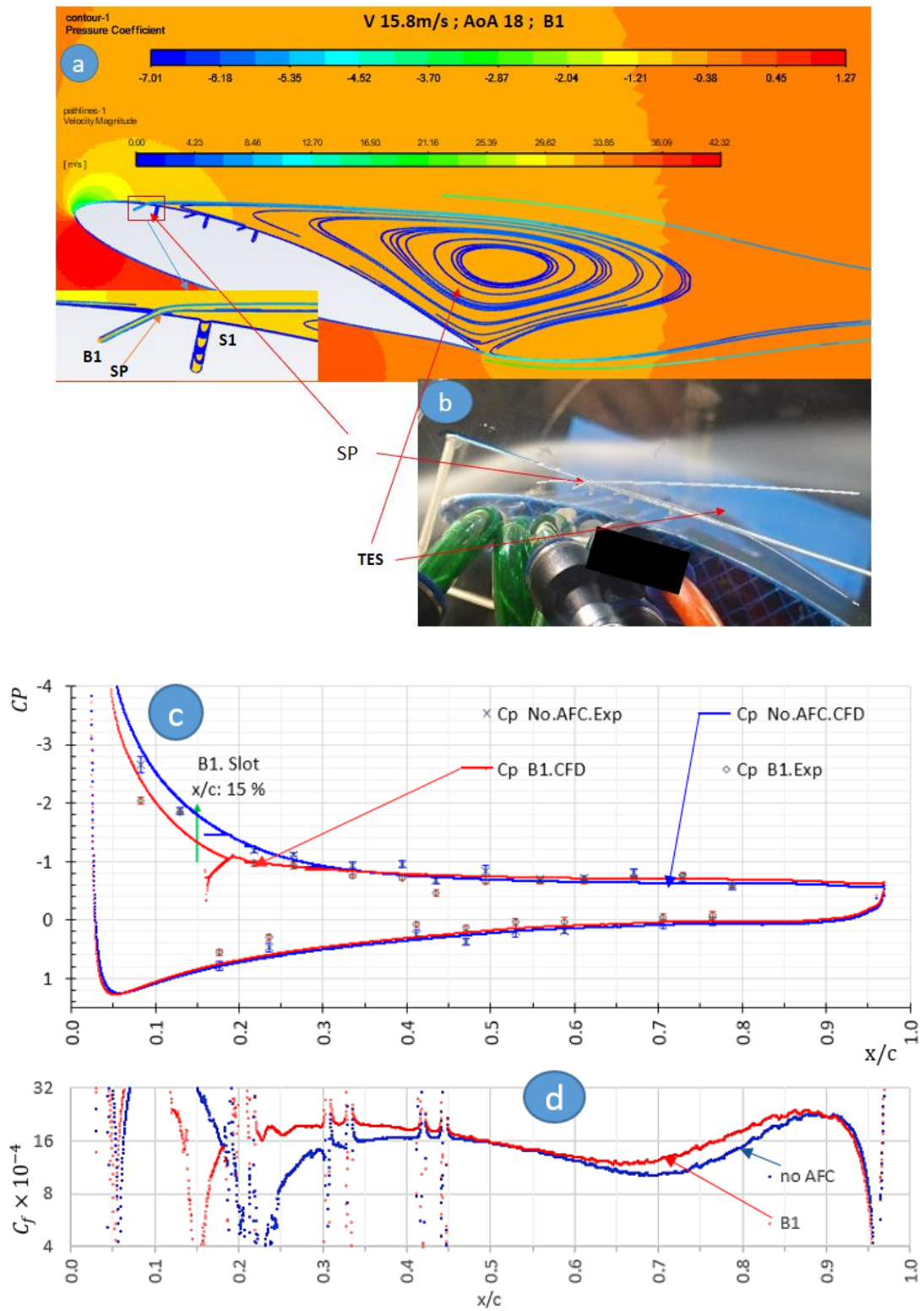
Figure 5-6: Flow behaviour of the blowing technique at B1 as per Figure 5-5.

Figure 5-7 shows the results from applying the blowing technique at station B2 (at location $x/c = 0.36$). This forms a LSB between B2 and S2 (Figure 5-7-a), due to the increased flow speed in that region. Moreover, as a result of blowing process at B2, it caused a delay in the separation point and moved it downstream from the point $x/c = 0.23$ to the point $x/c = 0.37$. This was accompanied by a decrease in pressure from the leading edge down to B2, followed by a pressure fluctuation that continued until $x/c = 0.34$, and then a very slight increase in pressure until the end.

The third technique is blowing at slot B3 ($x/c = 0.54$) (Figure 5-8). Due to the high angle of attack (18°), the LSB was formed and extended from $x/c = 0.28$, near S2, to $x/c = 0.38$, at B3. This was followed by another LSB occurring between B3 and S3, due to blowing technique at B3. Then the flow reattached with the surface until separation occurred at $x/c = 0.51$. On the other hand, the pressure decreased from the leading edge to point $x/c = 0.4$, followed by a fluctuation in pressure to the point of $x/c = 0.45$. A very slight increase was then observed that continued to the trailing edge.
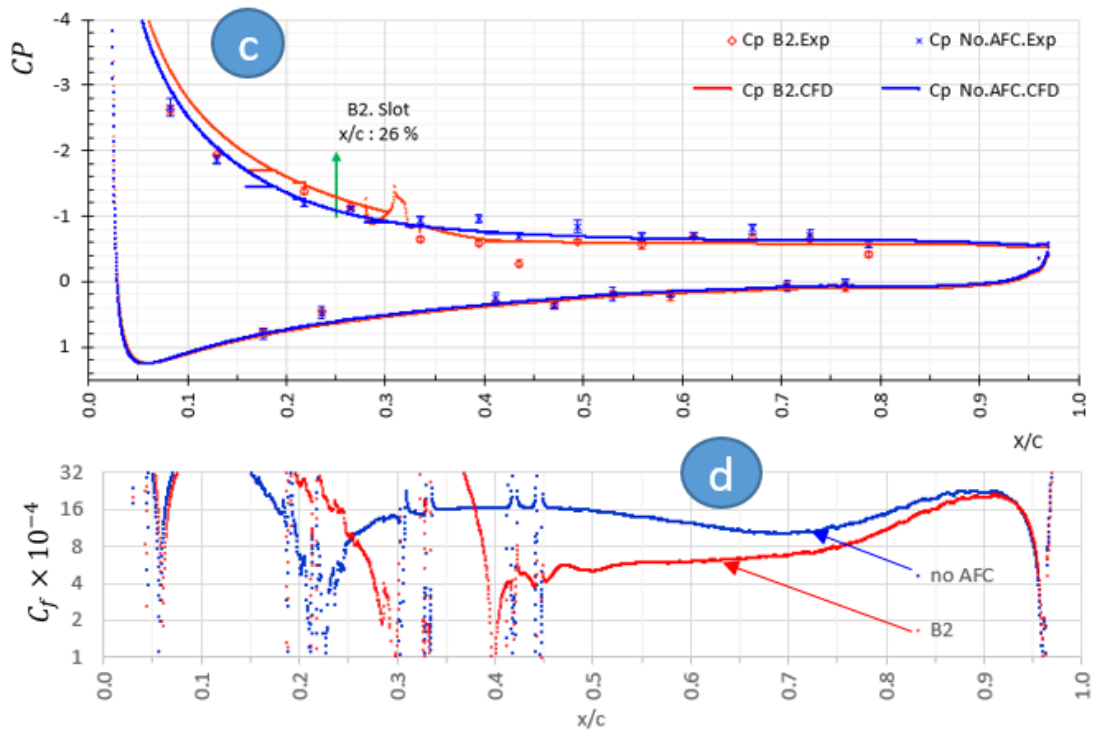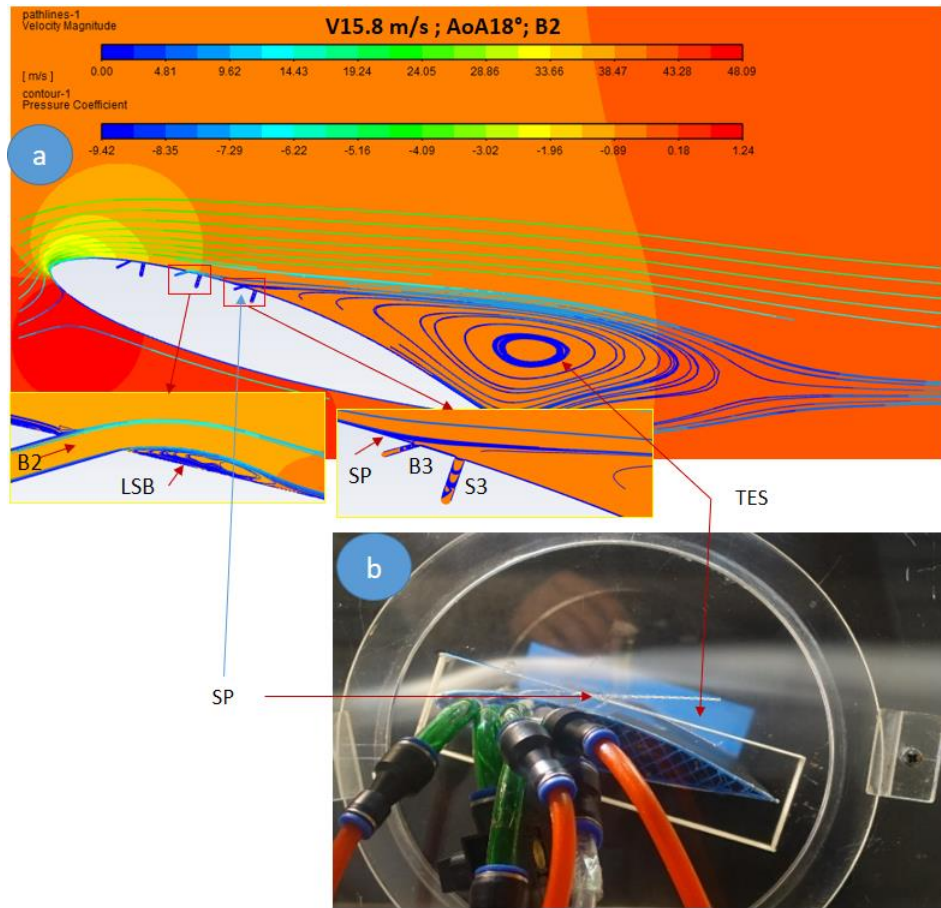
Figure 5-7: Blowing technique flow behaviour at B2, as per Figure 5-5.
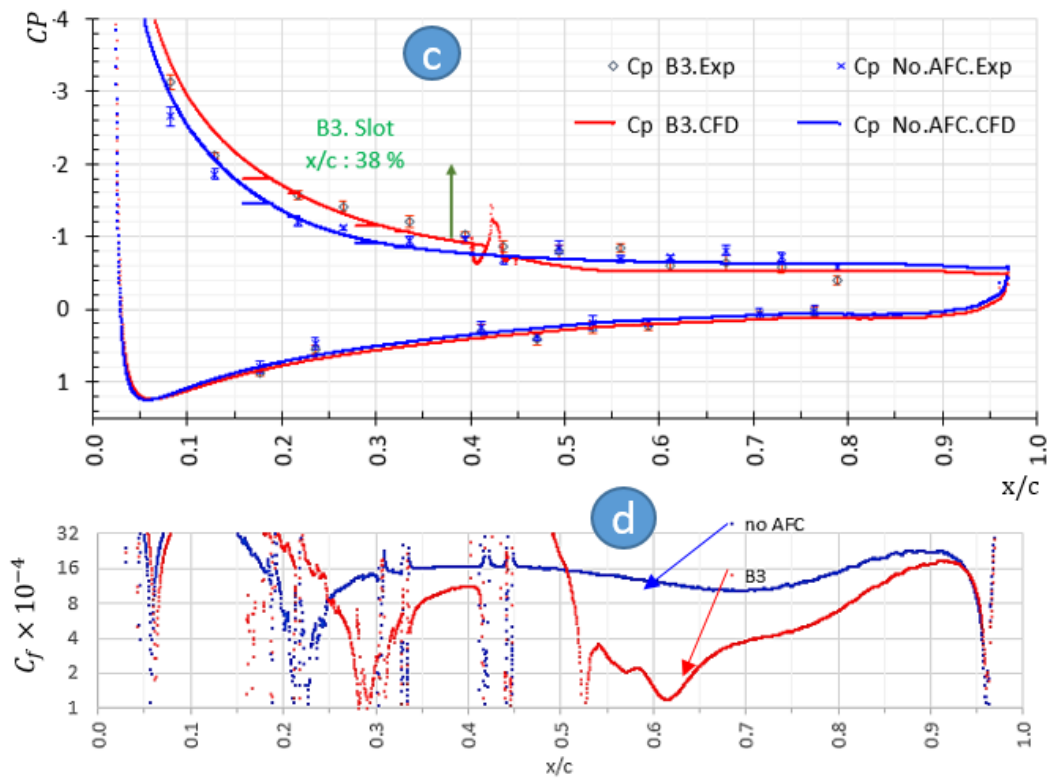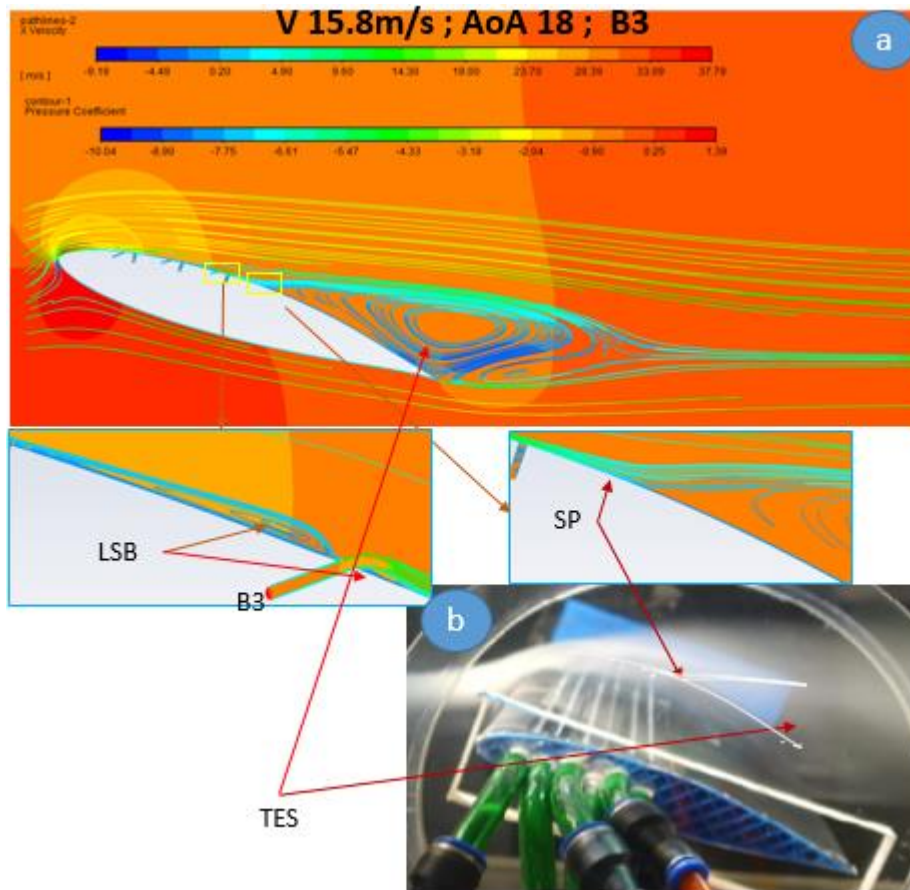
Figure 5-8: Blowing technique flow behaviour at B3 as per Figure 5-5.

5.3.3 Effect of suction only

In suction techniques, the same procedures will be undertaken as with blowing operations described in the previous section (5.3.2).

In Figure 5-9, suction technique at S1 ($x/c = 0.18$) is represented. In this test, the point of flow separation (SP) has moved from the point $x/c = 0.23$ (in the baseline case) to $x/c = 0.46$ (with AFC). No LSB was observed in this test. The pressure decreased significantly compared to the baseline case until the point $x/c = 0.21$ followed by a fluctuation in pressure as a result of the technique used (S1), resulting in a second, smaller pressure drop ($0.20 < x/c < 0.42$) due to the APG. Thereafter, there was a very slight increase in pressure until the end of the model.

Figure 5-10 illustrates suction technique procedure of S2. It is noticed that LSB did not appear for the second time in the suction procedure. There was also a pressure drop to the point $x/c = 0.33$ followed by a short fluctuation and then an increase in pressure up to the trailing edge. The separation point occurred at the location of $x/c = 0.43$.

Nevertheless, in Figure 5-11, which illustrates using the suction technique at S3, the extended type LSB was formed from point $0.25 < x/c < 0.41$ (where suction technique used is present), and this is because S3 is too far downstream from the usual separation point. This approach is unable to overcome the effect of APG and leads to LSB generation. Moreover, there were no continuations of the re-attachment to the surface after LSB, but a separation occurred directly after S3.
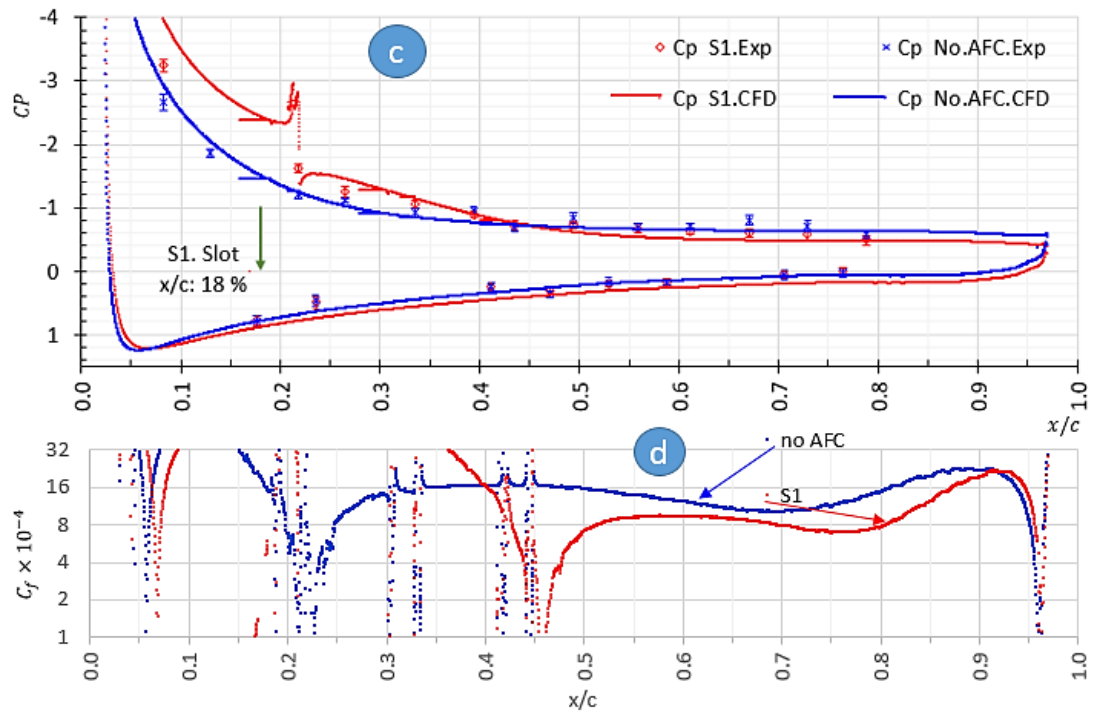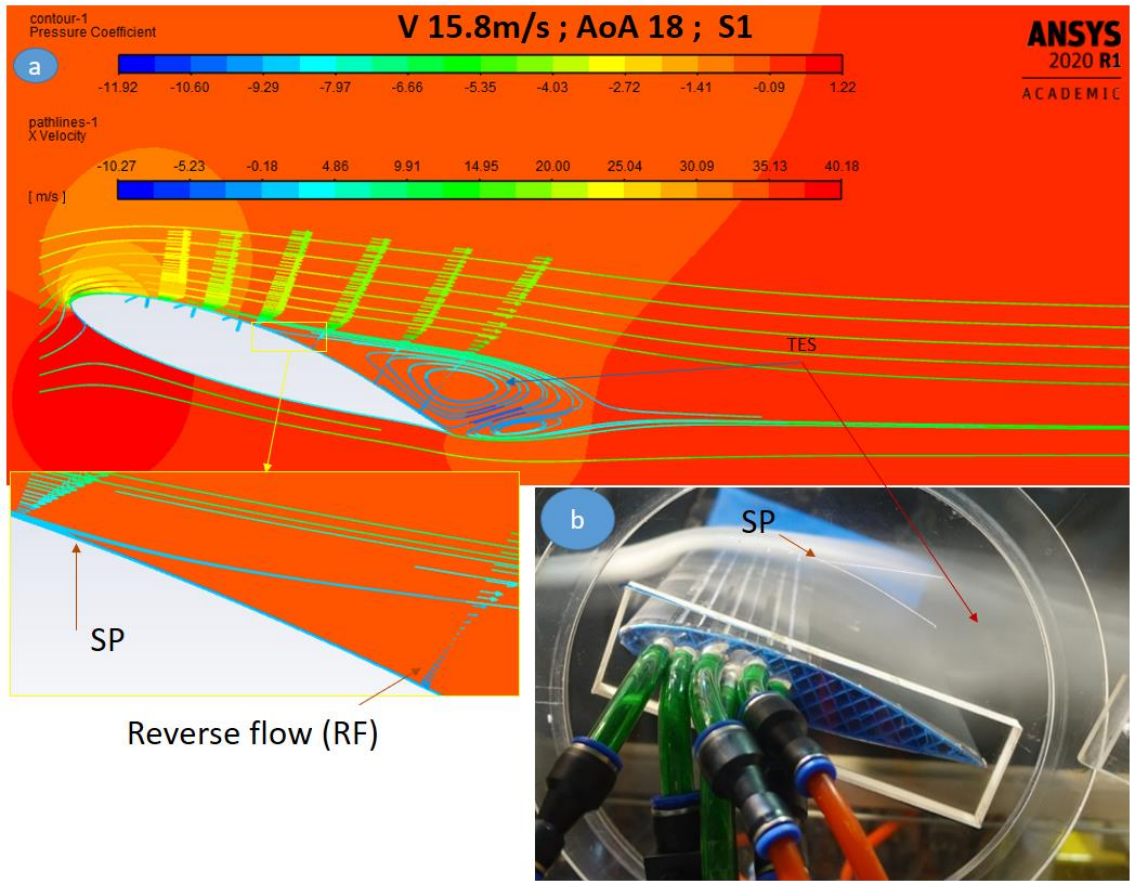
Figure 5-9: Suction technique flow behaviour at S as per Figure 5-5.
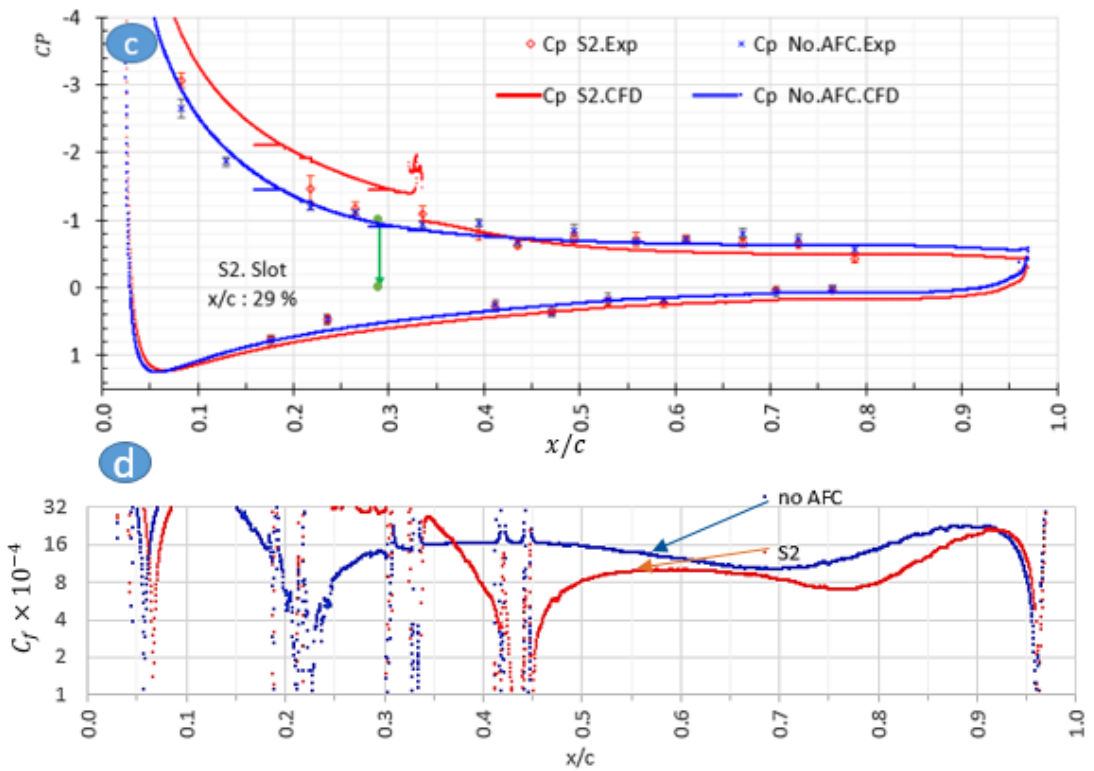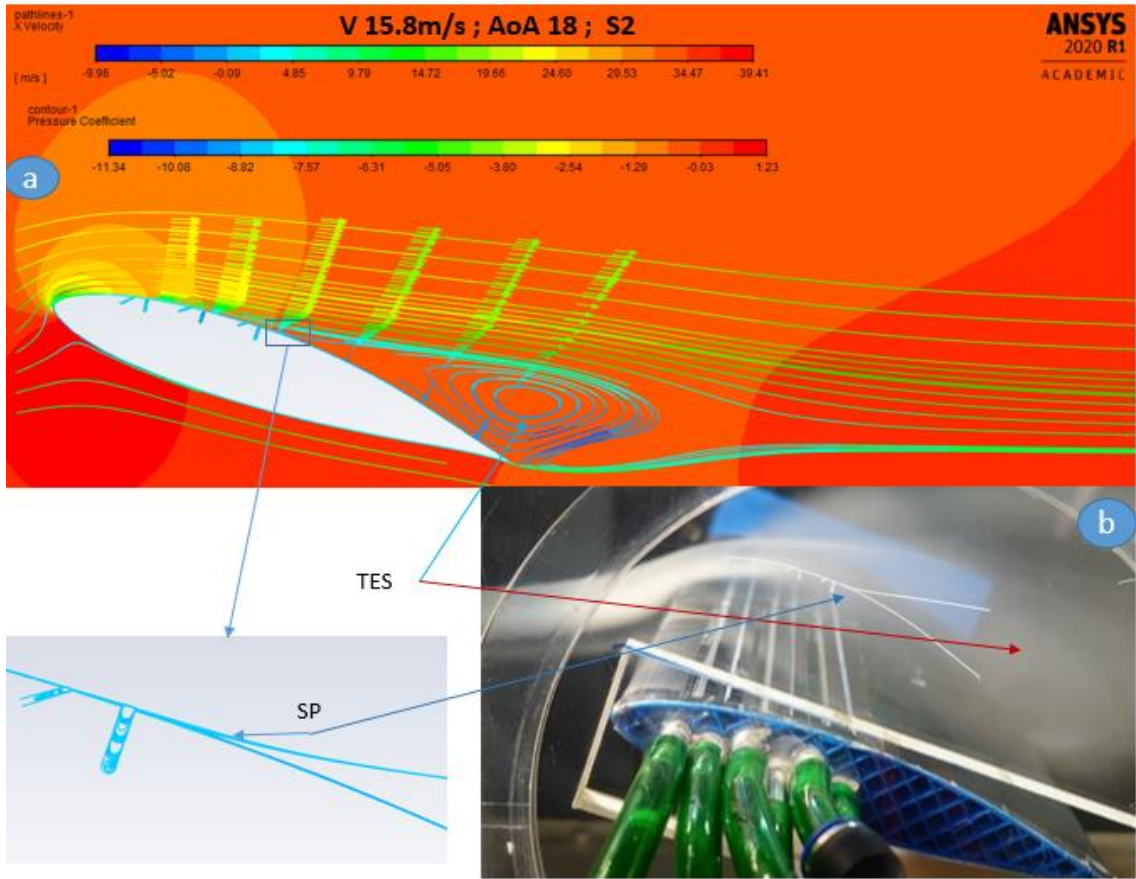
Figure 5-10: Suction technique flow behaviour of S2 as per Figure 5-5.
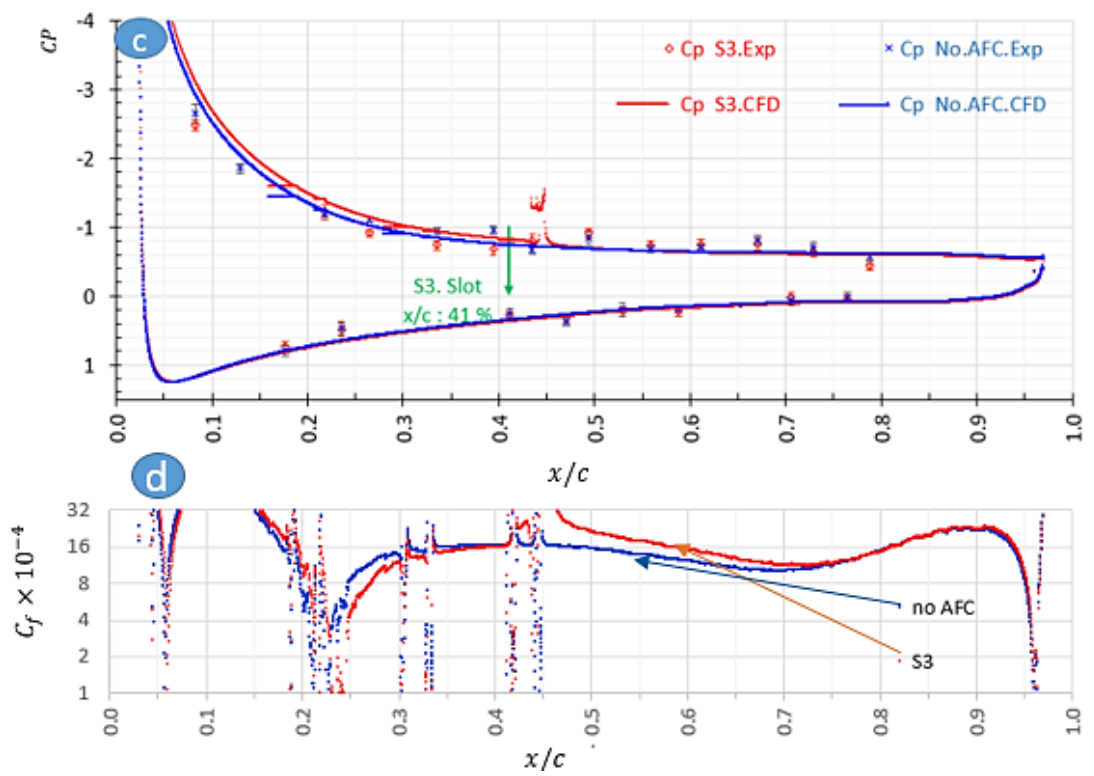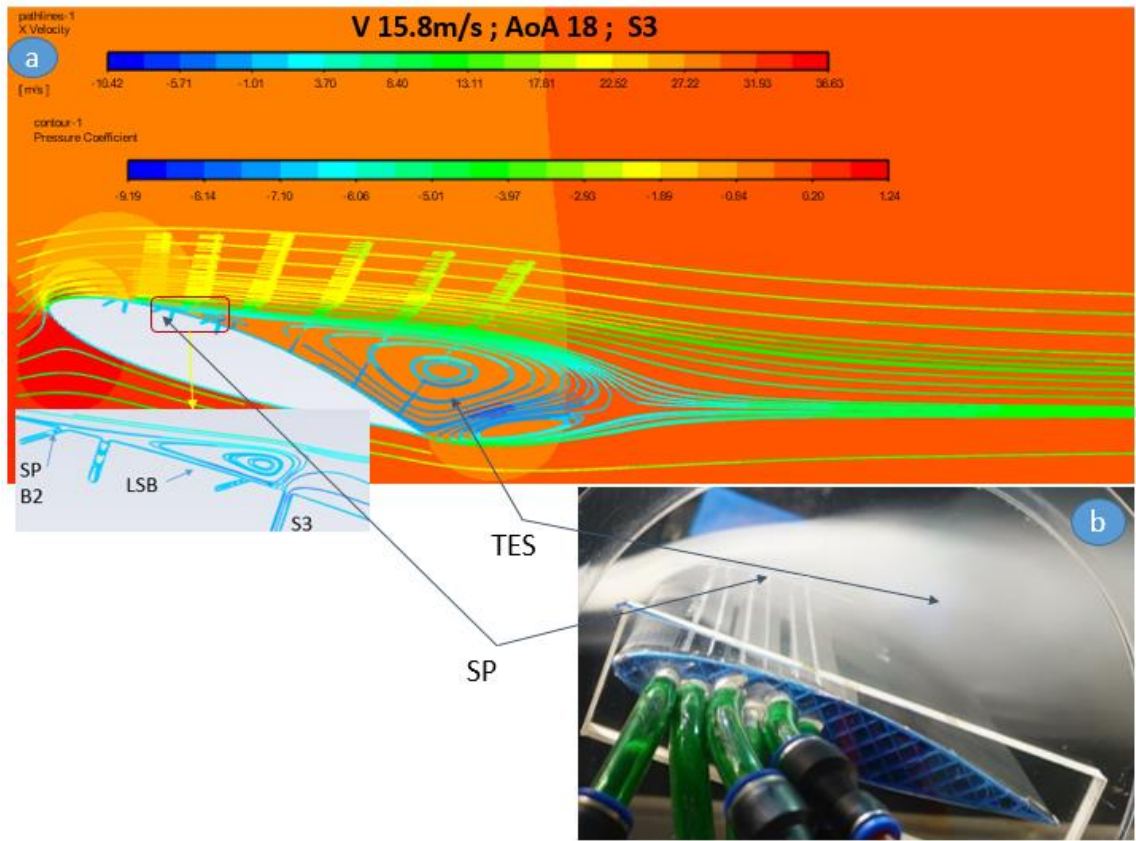
Figure 5-11: Flow behaviour of the suction technique at a slot of S3 as per Figure 5-5

5.3.4 Effect of the best combination of suction and blowing

From the results above, the best blowing technique was the technique at B3 slot, and the best suction technique was the technique at S1 slot so that the technique S1B3 will be tested (Figure 5-12).

A short LSB appeared between slots B3 and S3 because of the technique at B3. The separation point was moved from $0.23 < x/c < 0.53$. So, the combination of methods is an improvement on B3 and S1 individually. Moreover, after using both techniques (S1 and B3) individually, two short pressure fluctuations occurred ($0.21 < x/c < 0.24$ and $0.45 < x/c < 0.47$). The behaviour of the pressure drop for the combination S1B3 was similar to the two techniques S1 and B3 individually, but the combination of the two methods made the pressure drop greater by reducing the pressure on the upper surface overall. However, a very slight increase in pressure was noticed after the point of $x/c = 0.47$. This is normal since the pressure gradient becomes greater towards the trailing edge.
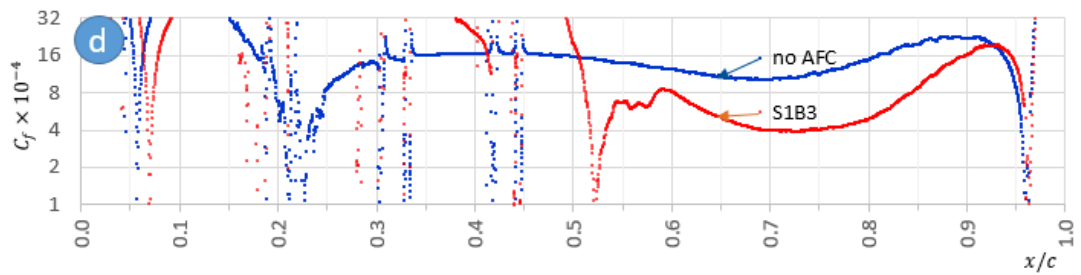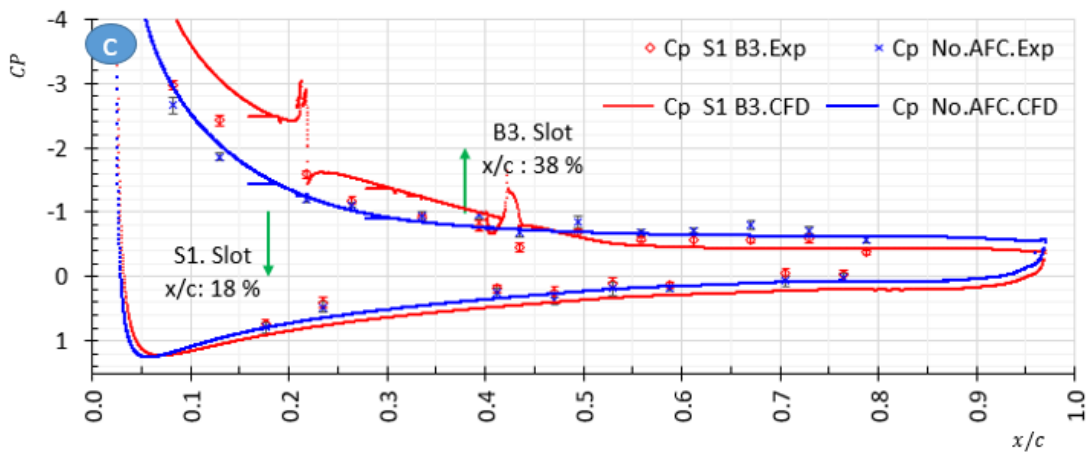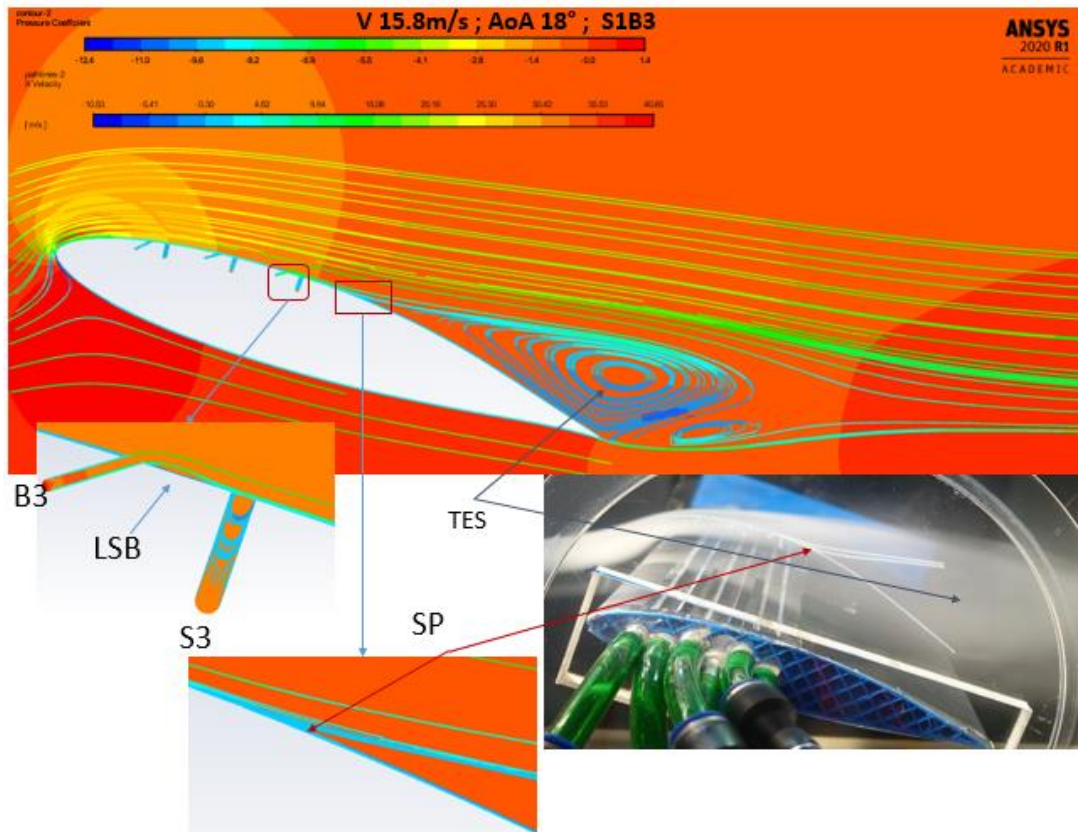
Figure 5-12: Flow behaviour of the suction technique at slots of S1 & B3 as per Figure 5-5

5.3.5 Comparison of AFC techniques

The following diagram (Figure 5-13) shows a summary of the ten cases previously discussed in section 5.3. It is expected to give a clear visualization and perception of the significance of the inferred outputs related to the flow separation LSB, and APG effect.

Since blowing in B1 was performed upstream of the separation point in the baseline case, the pressure on the upper surface increased because kinetic energy was added to the flow, which increased the amount of momentum. However, this accelerated the separation caused by the high angle of attack, so the separation point shifted towards the leading edge. However, in the B2 and B3 blowing techniques, a separation delay was observed with a short LSB generation downstream of each technique. Nevertheless, the separation delay in B3 was significant. However, a long LSB occurred upstream of the B3 technique. In other words, the blowing process in B3 cannot wholly overcome the effect of APG upstream of the position of this technique (B3). However, it is considered the best technique (of the chosen locations) for blowing operations.

From another point of view, it is known that suction operation reduces the amount of momentum and thus the effect of APG. However, since suction stations are located significantly downstream of the baseline separation point, the delay occurs with a long LSB before suction technique, as in the case of S3. However, because the suction technique in S1 occurred near the separation point, and even upstream of the separation point, it gave noticeably more positive results compared to other suction technique cases. It can be concluded that blowing should preferably be significantly downstream of the leading edge (after the flow exceeds the highest point (geometrically) on the upper surface of the aerofoil) and suction slot as close as practicable to the leading edge. In other words, it is preferable to have early suction with/without delayed blowing
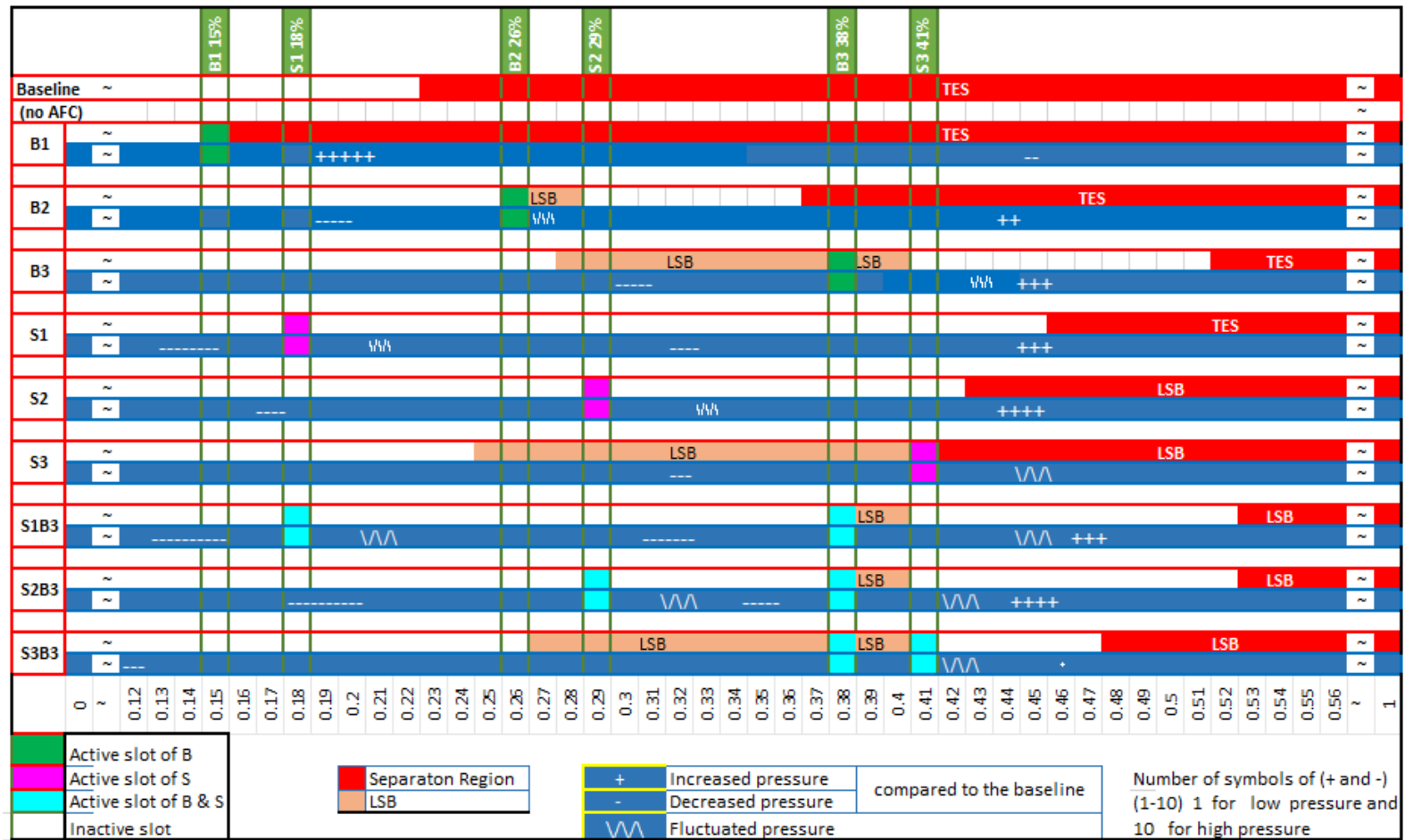
Figure 5-13: Summary of AFC techniques used by explaining the LSB, SP, TES and pressure distribution.

In order to see the improvement in AFC implementation, the percentage improvement in the lift-to-drag ratio should be as found in Equation 5.1:

$$\text{Percentage improvement} = \frac{\text{the new value} - \text{the original value}}{|\text{the original value}|} \times 100 \qquad \text{..... 5-1}$$

The percentage of improvements of lift-to-drag ratios for all of the tested AFC techniques for high (18°) angles of attack, is shown in Figure 5-14. The results show that the best technique for blowing is B3 with an improvement of lift-to-drag ratio of 30%. Also, it was shown that the best technique for suction is S1 with an improvement of 71%. S1 is significantly superior due to the presence of LSB during the procedure of the B3 technique.

Based on Figure 5-14 the highest lift-to-drag ratio (C_L/C_D) is S1B3. So, it can be considered that S1B3 is the best technique with an improvement rate of 87%, at first glance. However, the power consumption is proportional to mass flow rate multiplied by velocity, so blowing consumes significantly more power. Therefore, AFC S1 gives results with more efficiency (71%) than the AFC S1B3 technique. Moreover, the additional cost of installing two slots, let alone the necessity to include both a vacuum pump and a normal pump is prohibitive. Therefore, in many engineering fields, the simplest solution is often the best, even if it is not the best scientific solution. Therefore, S1 will be the optimal technique for high angles of attack.

Other tests were conducted for the same set of AFC techniques, but with an angle of attack of 9° to ensure that the drag coefficient could be reduced at low angles of attack compared to the baseline case. In Figure 5-15, the percentages of lift-to-drag ratios were represented for a lower (9°) angle of attack. The results show that the best technique was S3 with a value of 18%. Furthermore, S1 improves the lift-to-drag ratio to 14%. So S1 is optimal for both low/high angles of attack because the optimum design would be to install only one slot, instead of two.
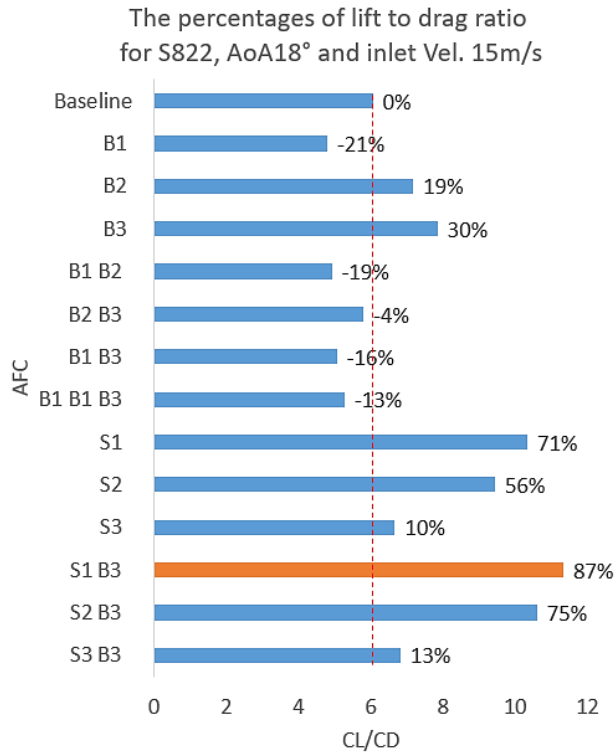
Figure 5-14: Lift-to-drag ratios with their improvement percentages for S822 aerofoil AFC with AoA of 18° and 15.8 m/s inlet wind speed.
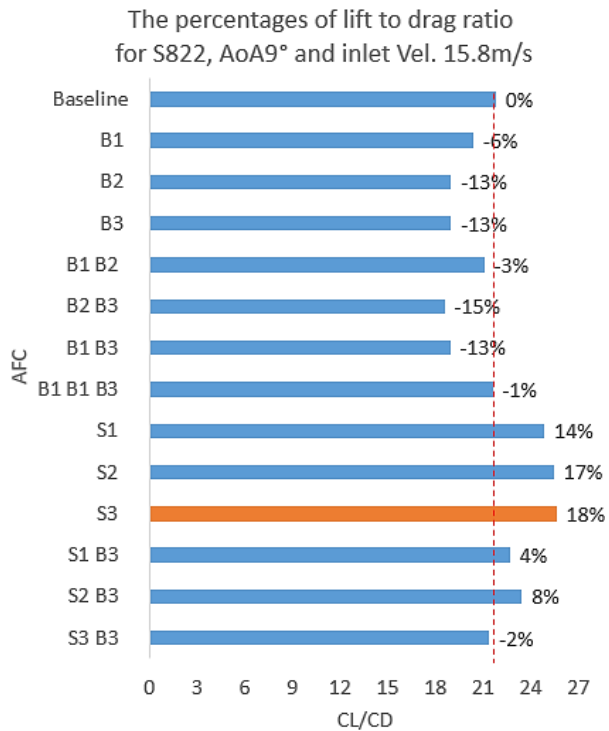
Figure 5-15: Lift-to-drag ratios with their percentages for S822 aerofoil AFC with AoA of 9° and 15.8 m/s inlet wind speed.

5.4 Summary

In this chapter, simulations performed on S822 and S823 aerofoil models using the transient SST (γ-Re_{θ}). Turbulence model was validated by laboratory experiments. Separation points were also determined after applying suction and blowing techniques to the NREL S822 aerofoil. The delay in the occurrence of separation was accompanied by an improvement in lift coefficient, as the flow may be connected to the upper surface of the model due to high lift coefficient value. However, the drag coefficient may also be high, and its effect on the flow separation does not appear. In other words, the flow separation delay may appear as a result of the improvement of the lift coefficient, which may be accompanied by a rise in the drag coefficient. Therefore, the state of lift-to-drag ratio must be taken into consideration even if there is a fully-attached flow on the aerofoil surface.

Moreover, the optimum technique was determined at high/low angles of attack. It was found that the S1 technique was the best for high and low angles of attack . The reason for that is because using one slot with one vacuum pump is far superior to using two slots. Therefore the S1 technique for both low and high angles of attack will be investigated for multi suction's velocities, and hence, the optimum technique will be investigated for a wide range of AoA in the next chapter.

CHAPTER 6: THE OPTIMUM AFC TECHNIQUES

As mentioned previously, knowledge of aerofoil performance improvement lies in the knowledge of the highest glide ratio (lift-to-drag ratio). In the previous chapter, the optimum technique was found to be suction technique at slot S1, which provides the best lift-to-drag ratio for high and low angles of attack, respectively. In this chapter, the optimum suction velocities for several values of Reynolds numbers will be investigated. Figure 6-1 illustrates the methodology to obtain the optimal technique.
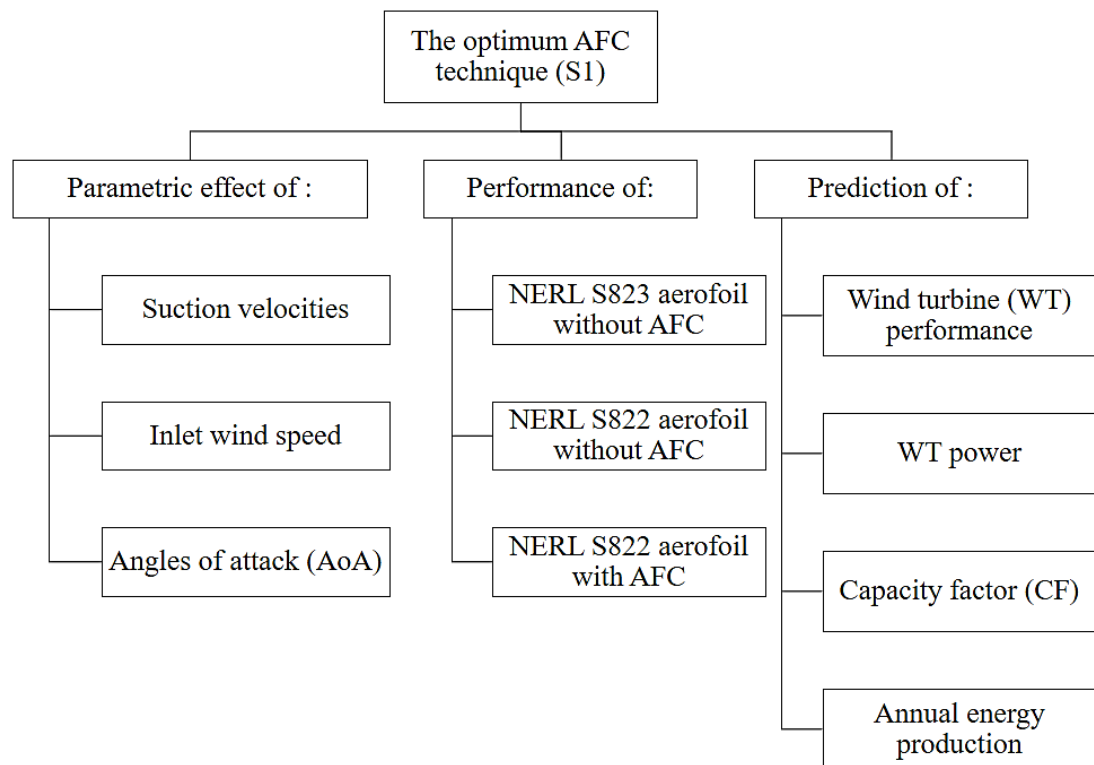
Figure 6-1: The methodology to obtain the optimisation technique

6.1 Parametric effect of suction velocities

The simulation was performed on the NREL S822 aerofoil model with and without flow control techniques, for inlet wind speeds of 15.8 m/s, producing a low Reynolds number (1.83×10^5), for the chord line of the models (0.17 m). Two angles of attack (9° and 18°) were selected for low and high angles of attack conditions, respectively. Moreover, suction flow speeds were adjusted for the S1 technique in order to identify

the best operating condition. Four suction speeds were used in these tests (Table 6-1). Also, lift coefficient, drag coefficients and lift-to-drag ratio were represented for NREL S822 aerofoil, as shown in Figure 6-2-a, b, and c respectively).

Table 6-1: Suction speeds at slot S1 which were utilized in the tests

Suction speed at slot S1 (m/s)	-5	-15	-25	-35
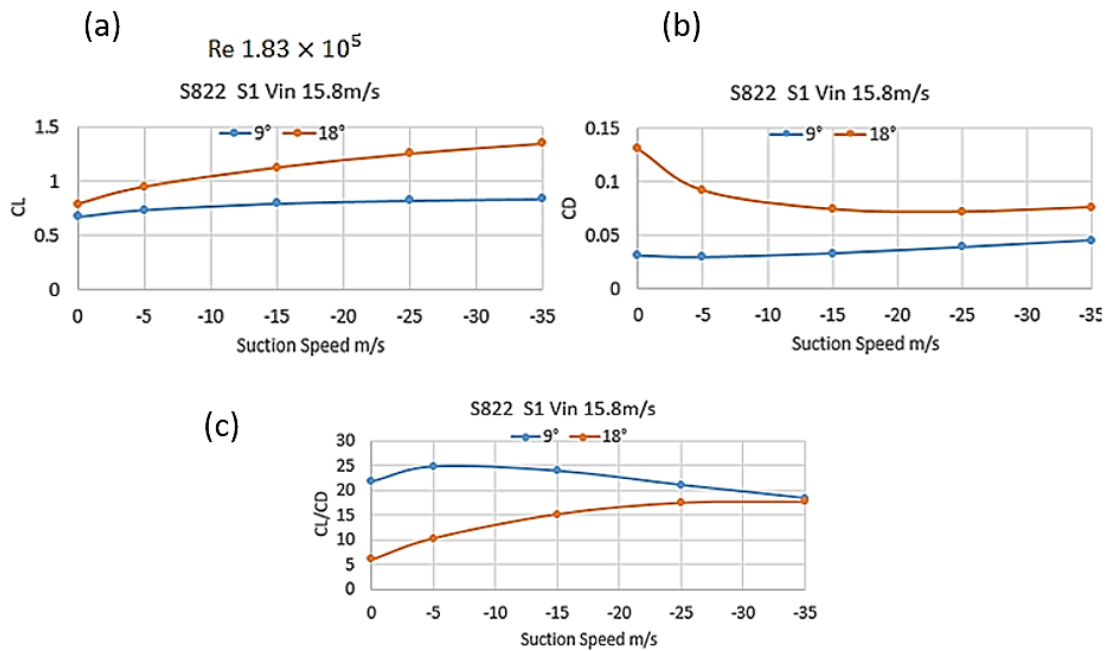
Figure 6-2: (a) Lift and (b) Drag coefficients and (c) the lift-to-drag ratio of S822 aerofoil with AFC S1 for variable suction speed for low (9°) and high (18°) angles of attack (AoA)

In order to establish the effect of suction speed on both the lift and drag coefficients, a specific suction case was studied at an inlet velocity of 15.8 m/s. The results revealed that the lift coefficients increase with the increase in suction speed (Figure 6-2 -a). However, the amount of increase at AoA 18°, is greater than at an angle of attack of 9°. On the other hand, the drag coefficient (Figure 6-2-b) with an angle of attack of 18° decreases when increasing suction speed up to-15 m/s because the amount of momentum sucked will increase, which reduces the effect of the adverse pressure gradient (Figure 6-3). Once a speed of-15 m/s is exceeded, suction velocity becomes

higher than the inlet velocity (15.8 m/s) so that the drag force becomes approximately stable. However, the increase in suction speed once-15 m/s is exceeded will improve the amount of lift force, and this is what makes the ratio of lift-to-drag increase. With an angle of attack of 9°, lift-to-drag ratio starts to rise slowly after suction speed of -5 m/s. The drag coefficient with an AoA of 18° is higher than with an AoA of 9°.
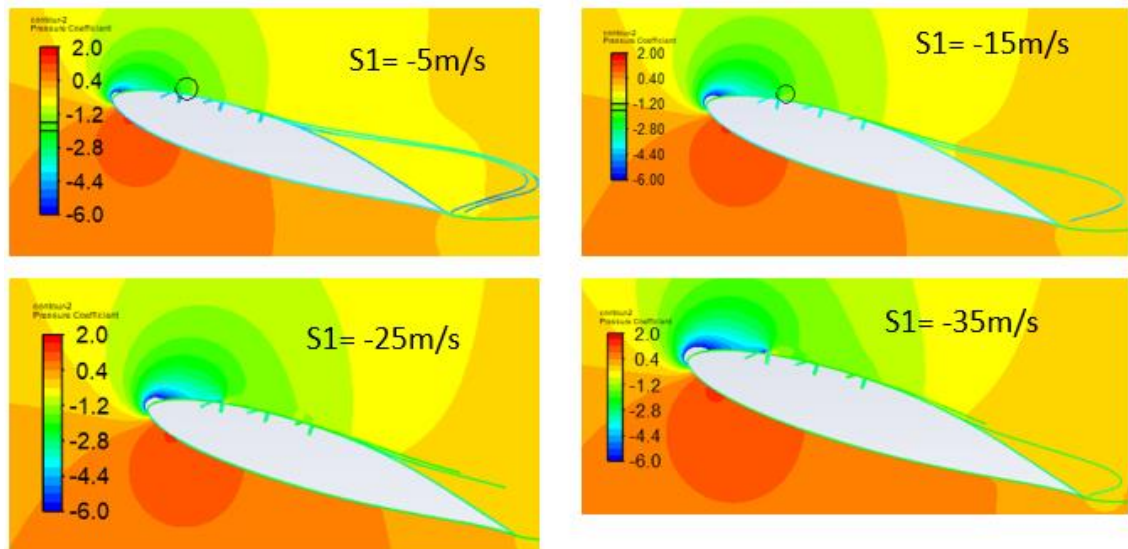
Figure 6-3: Pressure contour and streamlines of S822 aerofoil (AoA 18°) with variable suction velocity

The lift-to-drag ratios for AFC S1 were examined using suction speeds, as mentioned in Table 6-1 and inlet wind speeds, in Table 6-2. Low Reynolds numbers were calculated (Table 6-2) according to inlet wind speeds mentioned when the chord line of the models was 0.17m. So the results of all required outputs (such as lift-to-drag ratio, power coefficient of the wind turbine, and wind energy production for low wind speed sites) will be presented according to Reynolds number instead of inlet wind speed.

Table 6-2: Reynolds number for selected inlet velocities

V_{inlet} (m/s)	15.8	25	35	45
Reynolds No.	1.83×10^5	2.85×10^5	4.00×10^5	5.14×10^5

Figure 6-4 shows lift-to-drag ratios for the Reynolds numbers mentioned. When the angle of attack is 18°, the lift-to-drag ratios increase with the increasing suction speed. So the optimum suction speed, in this case, is -35 m/s according to the input data. However, when the angle of attack is 9°, the best suction speed is -5 m/s because it is close to the maximum lift-to-drag ratio for all Reynolds numbers.
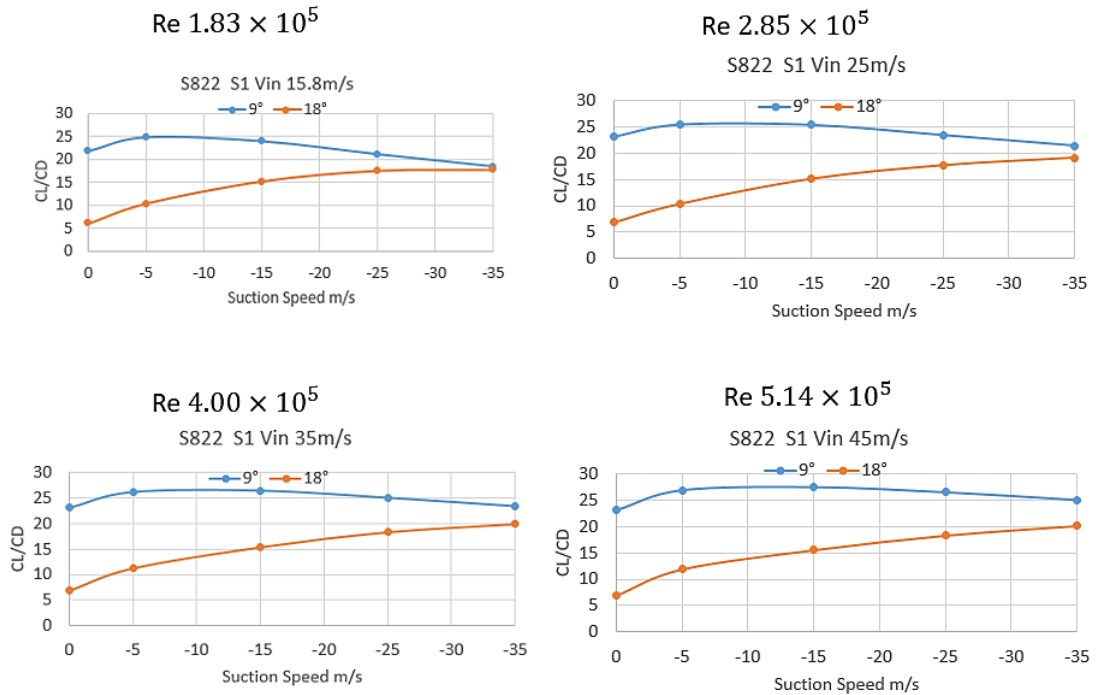
Figure 6-4: Lift-to-drag ratios for S822 aerofoil with AFC S1 for variable suction speed and several inlet wind speeds for AoA of 9° and 18°

6.2 Parametric effect of flow Reynolds number

In this section, the simulation was performed on the NREL S822 aerofoil model with and without active flow control (AFC) techniques to identify lift and drag coefficients and hence, lift-to-drag ratios (Figure 6-5). The AFC S1 technique was employed, with the following preferred suction velocities: (-5 m/s for low AoA and -35 m/s for high AoA). Two angles of attack were implemented with these tests (9° for low AoA and 18° for high AoA). The inlet wind speeds were varied, according to Table 6-2.
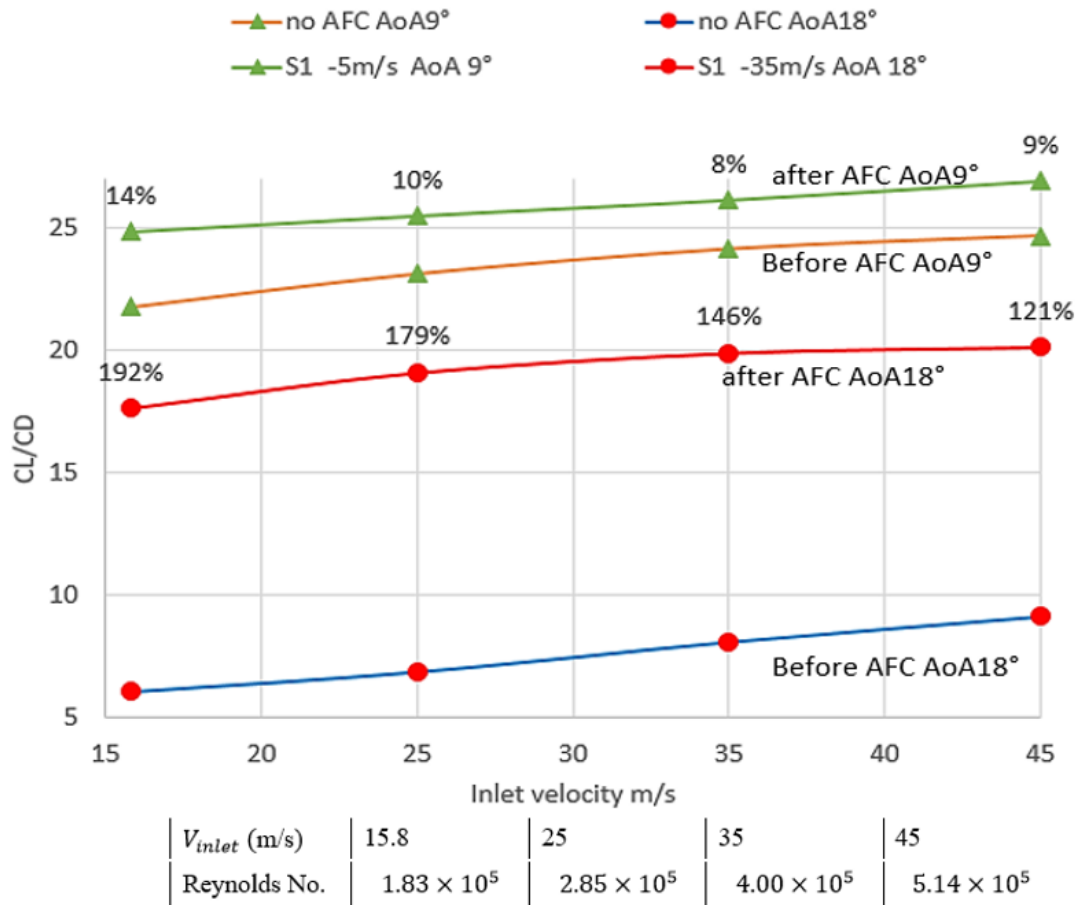
Figure 6-5: Lift-to-drag ratios with improvement percentages of S822 aerofoil with variable inlet wind speeds and optimum suction velocities (-5 m/s for low AoA and -35 m/s for high AoA) with AoA of 9° and 18°

The results identified in Figure 6-5 reveal that using AFC S1 improved the aerofoil performance in all of the test cases. The maximum percentage improvement occurred at the lowest Reynolds number for both AoA, which is partly due to the corresponding lowest lift-to-drag ratio without AFC. Nevertheless, the amount of improvement at high angles of attack (AoA) (such as 18° for instance) is greater than at low angles of attack (for example, 9°). The reason for this is that the separation at higher AoA was large, and the flow separation point closer to the leading edge. From this, it can be concluded that the separation treatment requires considerable suction energy. Therefore, suction speed is 35 m/s for high AoA (18°), whereas, for the lower AoA (9°), the separation is closer to the trailing edge and therefore the separation was

tackled using less suction energy; therefore the lower suction speed of -5 m/s could effectively be utilised. Moreover, Figure 6-5 indicates that there is an optimal flow Reynolds number for a given suction velocity because, at the higher AoA, the lift-to-drag ratio is approximately the same for the two highest Reynolds numbers. This optimal Reynolds number can be seen to decrease with increasing AoA; therefore, significant performance degradation at the highest experienced Reynolds number for a given suction velocity is only observed very close to the stall.

For a given Reynolds number and AoA, there is an optimal suction speed which will balance the improvement in lift-to-drag ratio with the power consumption of the suction process. Determining this suction speed will be aerofoil-dependent, so it is a suggestion for future studies.

6.3 Parametric effect of angle of attack

In this section, lift and drag coefficients of both NREL S823 and NREL S822 aerofoils were investigated for a range of AoA.

6.3.1 Performance of the NREL S823 aerofoil

The simulation was conducted on the NREL S823 aerofoil model. The lift coefficient curves are shown in Figure 6-6-a, increase with increasing Reynolds number and with increasing angle of attack. The stall occurred at 20º. The drag coefficient (Figure 6-6-b) reduced with increasing Reynolds number and increasing angle of attack. The lift-to-drag ratios (Figure 6-6-c) improved with increasing Reynolds number; however, the largest value measured was at 6.
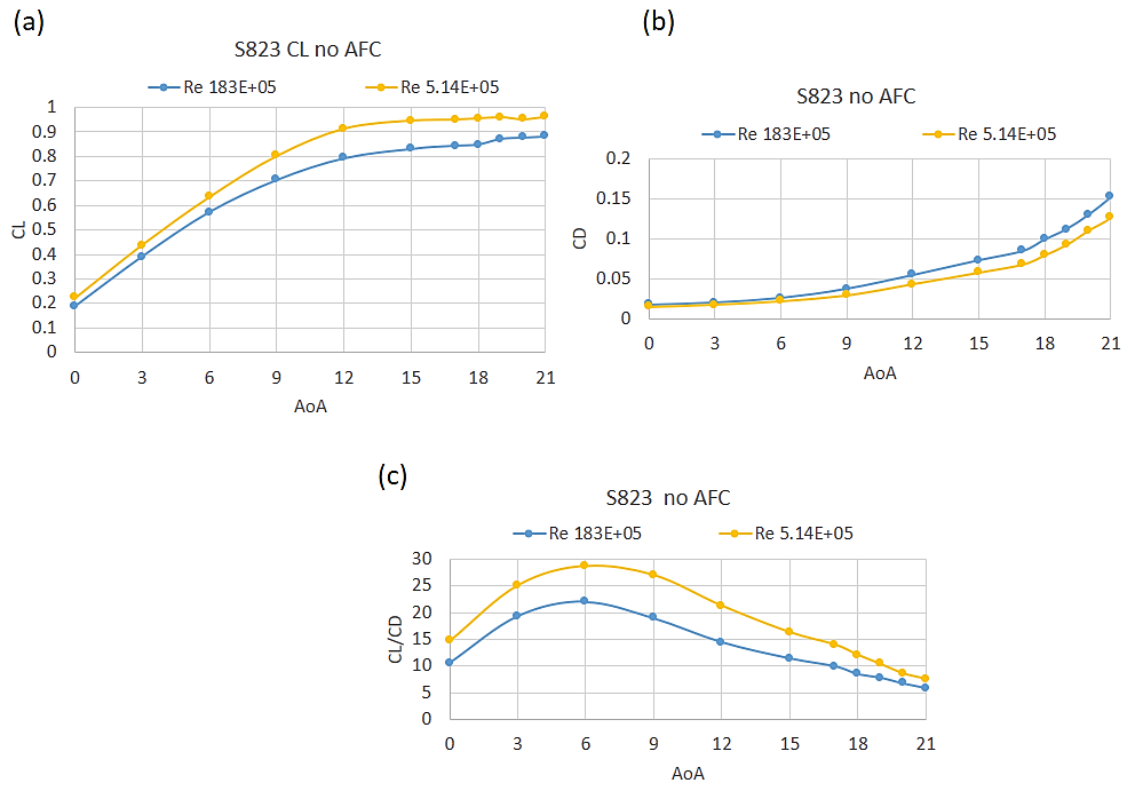
Figure 6-6: Performance of the NREL S823 aerofoil with low Reynolds numbers:
(a) lift coefficient; (b) drag coefficient; (c) lift-to-drag ratios

6.3.2 Performance of NREL S822 aerofoil for baseline (without AFC) case

The NREL S822 aerofoil (with/without AFC) was studied for lowest/highest Reynolds numbers (1.83E+05 and 5.14E+05 respectively). The lift coefficients (Figure 6-7 (a and b)) appear, as expected, to increase with increasing angle of attack and Reynolds number until they reach their highest value and consequently, the phenomenon of the stall occurs, where the lift coefficient decreases. At the same time, the drag coefficient (Figure 6-7-c and Figure 6-7-d)) slowly increases to the 15° angle of attack. The drag coefficient exponentially increases between 15° and 20°, but the rate of increase decreases once the lift coefficient recovers. It is only for AoA close to the stall that there is a significant effect of Reynolds number on the drag coefficient. The lift-to-drag ratio (Figure 6-7-c) behaves qualitatively the same as the NREL S823 aerofoil,

except for the highest AoA, where the value is insensitive to either AoA or Reynolds number
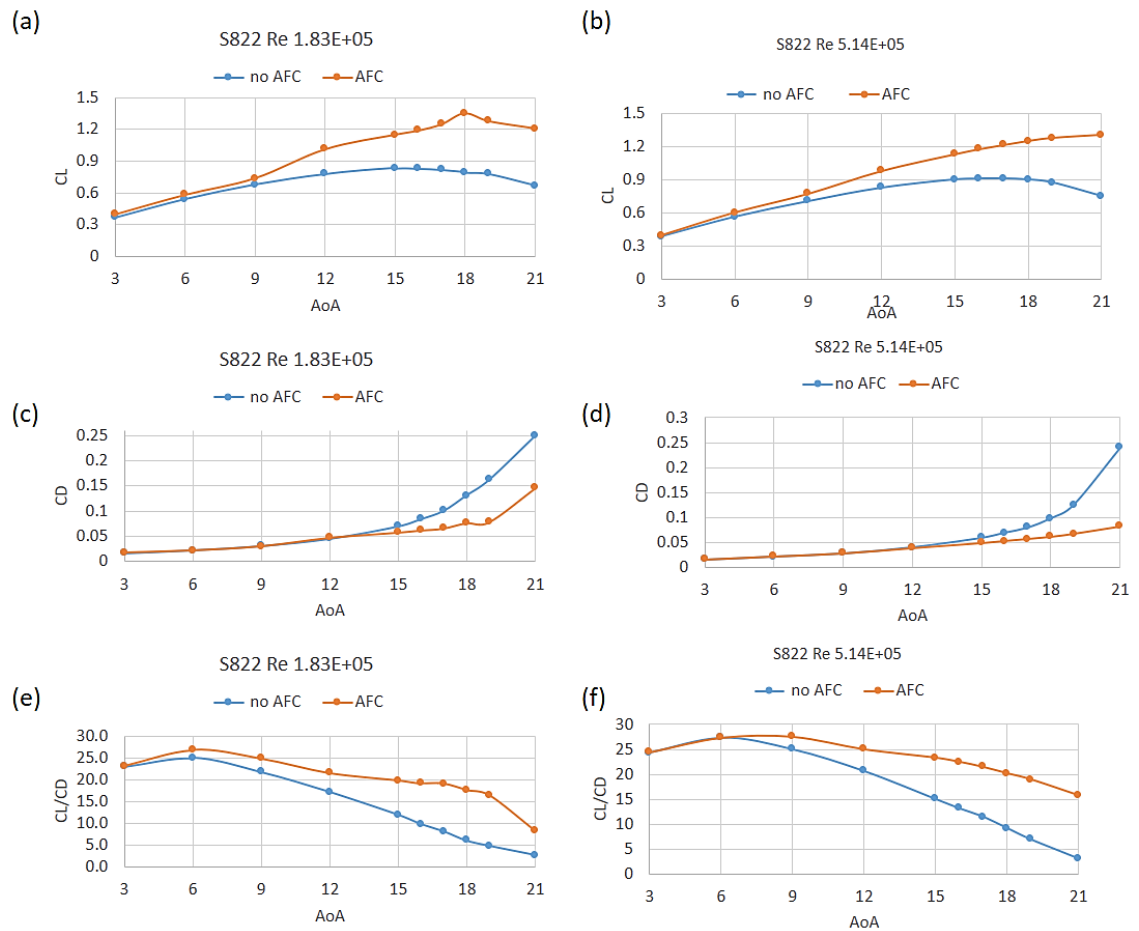
Figure 6-7: (a and b) lift and (c and d) drag coefficients with (e and f) lift-to-drag ratios with low Reynolds numbers for NREL S822 aerofoil with/without AFC techniques

Based on Figure 6-7 –a, it can be seen that the improvement in lift coefficient begins after AoA of 9°, where the amount of improvement increases until an AoA of 18°. That is, the curve after that angle appears parallel to the case 'without AFC'. In the higher Reynolds number case (Figure 6-7-b), the area between the two curves before and after the AFC is smaller than in the case of Figure 6-7-a. Figure 6-7-c and Figure 6-7-d represent the drag coefficients at low and high Reynolds numbers for the two states before and after the flow control technique (AFC). Despite the slight improvement in drag coefficient for angles of attack of less than 12°, the lift-to-drag ratio improved as a result of improving the lift coefficient by more than the

improvement in drag coefficient as shown in Figure 6-7-e and Figure 6-7-f. However, the improvement in drag coefficient at a higher Reynolds number (Figure 6-7-d) is better after the angle of attack of 18° which is different to Figure 6-7-c, where it is noticed that the improvement in lift-to-drag ratios (in both Figure 6-7-e and Figure 6-7-f) commences after a 6° angle.

In Figures 6-6 and 6-7, in spite of the largest values of lift-to-drag ratios were measured at 6°, but the separation at AoA of 6° may not occur. The AoA of 9 is the mean for all low angles of attack .so the AoA of 6 will not be represented all low angles of attack.

6.3.3 Performance of NREL S822 aerofoil with AFC

The potential improvement of the NREL S822 aerofoil was investigated for the lowest and highest Reynolds numbers by applying the best suction velocities (S -5 m/s for low AoA (0 – 11°) and S -35 m/s for high angles of attack (12°-21°)). In general, the lift-to-drag ratio (Figure 6-8) reaches its highest value at the angle of 6° (for the majority of them). Moreover, the improvement in aerofoil performance increases with increasing AoA. Furthermore, increasing the Reynolds number increases the lift-to-drag ratio. Finally, for each AoA, the improvement with Re 1.83+05 is greater than with Re 5.14+05.
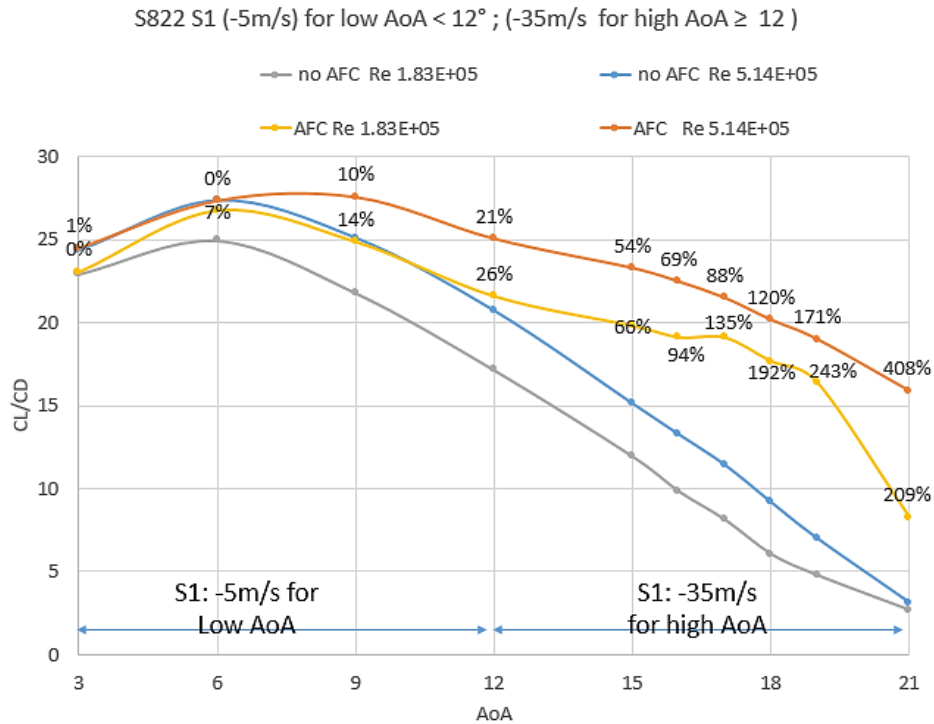
Figure 6-8: The effect of angle of attack on the lift-to-drag ratio for NREL S822 aerofoil with/without AFC techniques, and for different suction speeds

The flow separation expands with an increasing angle of attack. So more energy needs to overcome the adverse pressure gradient at high AoA and thus delay the separation as much as possible. Also at higher Reynolds numbers, the added energy produced by increasing the Reynolds number speeds up the flow and hence the ease of overcoming the reverse pressure gradient and thus improving aerofoil performance.

On the other hand, at high AoA, suction speed is -35 m/s, and the inlet speed is 15.8 m/s at lower Re, which is less than suction speed, while at higher Re, the inlet speed is 45 m/s, which is higher than suction speed. Therefore, logically, an improvement at a lower Re is a better outcome than a case of higher Re.

At low AoA, there is no improvement at or before an attack angle of 6° (at higher Re) because suction speed is -5 m/s compared to the inlet velocity (45 m/s), in contrast, the improvement in the lower Re condition starts from 3° and increases to 6° by 7%. This is because suction speed is closer to the inlet velocity than in the case of the higher Re. After that attack angle (6°), the amount of improvement stabilizes and is parallel to the

baseline case (lower Re; no AFC) up to the AoA of 12°. This is because of the increase in the angle of attack, which make the effect on APG greater.

6.4 Wind turbine performance and energy production

Wind turbine performance theories, including the blade element and momentum theories, are explained in Appendix D . In this research, a system was developed to improve the annual energy production for low wind speed sites, resulting in small horizontal axis wind turbines (sHAWT) with a rotor diameter of 10 meters, design tip speed ratio of 6.1, rated wind speed of 12 m/s, and two blades. Therefore, flow separation control technique (which has a significant effect on improving wind turbine performance) were used to delay the flow separation. NREL S823 aerofoil was utilised for the root of the blade (r/R (0-0.3)) and NREL S822 aerofoil for the tip blade (r/R (0.3-1)) as mentioned in Section 3 -5. The normalised radius ratio (r/R) is the ratio of the local radius of the blade to the wind turbine radius.

In Sections 6.3 Chapter 6: , the optimal method that used in this project, was studied using the (S1) suction technology with different suction speeds. In this section, a computer program (Appendix E was written in Matlab to predict the performance of sHAWT, its power and hence, the annual energy production for a low wind speed sites in Australia. The analysis in this section was based on the lowest and highest values of the Reynolds numbers tested (Table 6-2).

6.4.1 The geometry of wind turbine blades

The rotor blade parameters (including chord line, twist distributions and aerofoil type) are considered essential when determining the optimal design for wind turbine rotor blades. So the chord line and twist angle of the aerofoils as functions of r/R were investigated (Figure 6-9) for a 10 m diameter wind turbine. The r/R = 0 located at the centre of the wind turbine rotor (hub), and the tip of the blade, r/R are both equal to 1.
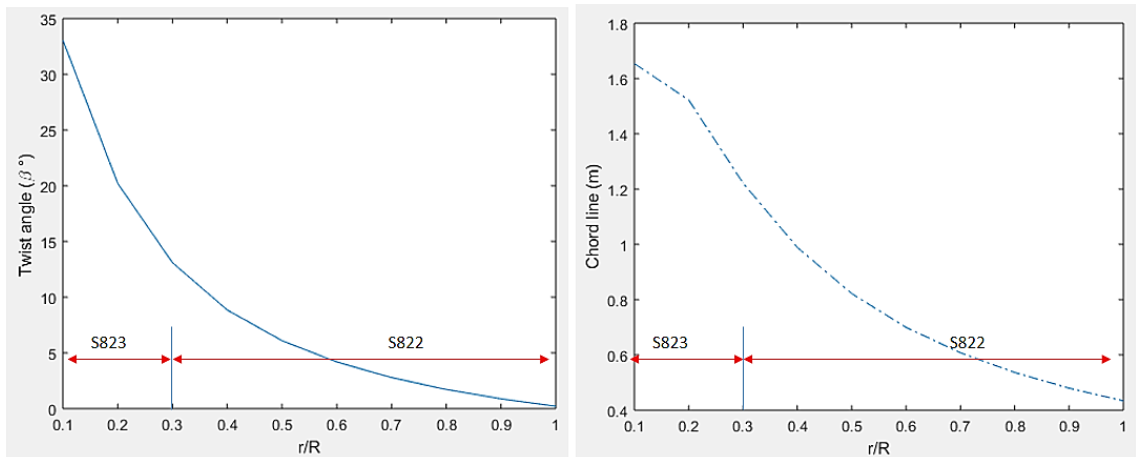
Figure 6-9: The blade twist angle and chord line versus local radius ratio r/R

6.4.2 The power coefficient (C_p)

The power coefficient is a suitable formula for measuring wind turbine power. According to power (6-1), the power coefficient of a selected wind turbine (Appendix F) for rated wind speed (12 m/s) and the rated power of 25kW is approximately 0.30. Besides, the rotational blade speed was 140 rpm at its rated wind speed.

$$P_w = \frac{1}{2} . \pi . \rho . R^2 . V_r^3$$

.... 6-1

$$P_r = P_w . C_{p.max}$$

Where P_w is the wind power; ρ is the air density; R is the rotor radius ; V_r is the rated wind speed ; P_r is the rated power; and $C_{p.max}$ is the maximum power coefficient that usually occurs at the design tip speed ratio λ_d .

In Appendix G-1, the performance of a wind turbine or power coefficient versus tip speed ratio, for a design tip speed ratio (λ_d) of 4.9 and 6.1, was investigated without AFC and with using the best AFC technique for both lowest and highest tested Reynolds numbers. Although the optimum case incorporated three blades, it was found to be more costly (design, maintenance costs). On the other hand, due to the maximum

power coefficient which occurred at design tip speed ratio, the use of a design tip speed ratio of 4.9 will shift the curve of the power coefficient to the right. Consequently, the maximum power coefficient will be at five instead of six. Since the relationship between tip speed ratio (λ) and wind velocity is an inverse relationship (Equation 6-2), high λ values occur at low wind speeds,

$$\lambda = \frac{\pi . D . N}{60 . V}$$

6-2

Where D (m) is the rotor diameter; N (rpm) is the blade   speed, and V is the wind velocity (m/s);

In Figure 6-10, the improvement in power coefficient is clear for both of the selected Reynolds numbers for tip speed ratio values of less than the design tip speed ratio (6.1). This means that improvement occurs when AoA is high.
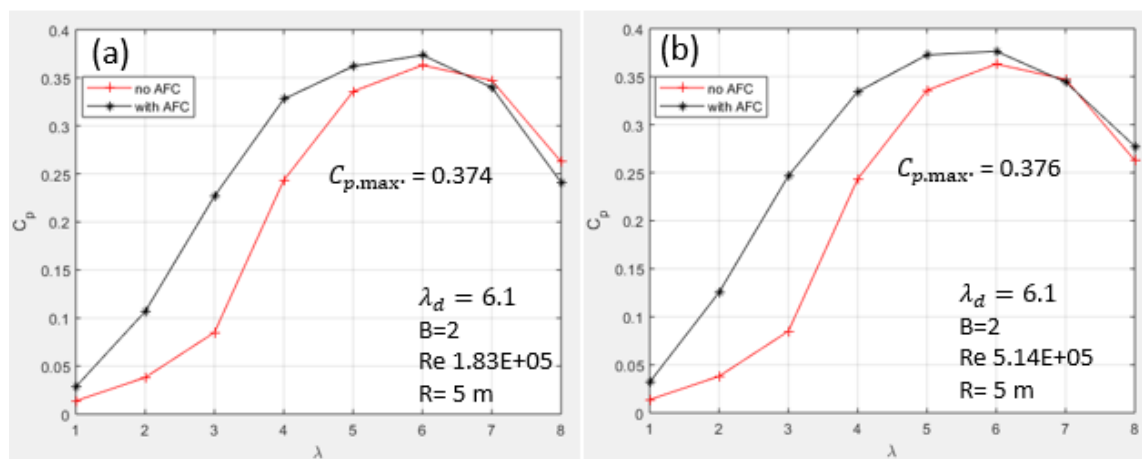
Figure 6-10: The power coefficient with/without the AFC for Reynolds numbers 1.83E+05 and 5.14E+05, when design tip speed ratios equal to 6.1 and when the number of blades is two

6.4.3 Wind turbine power and fixed rotational speed
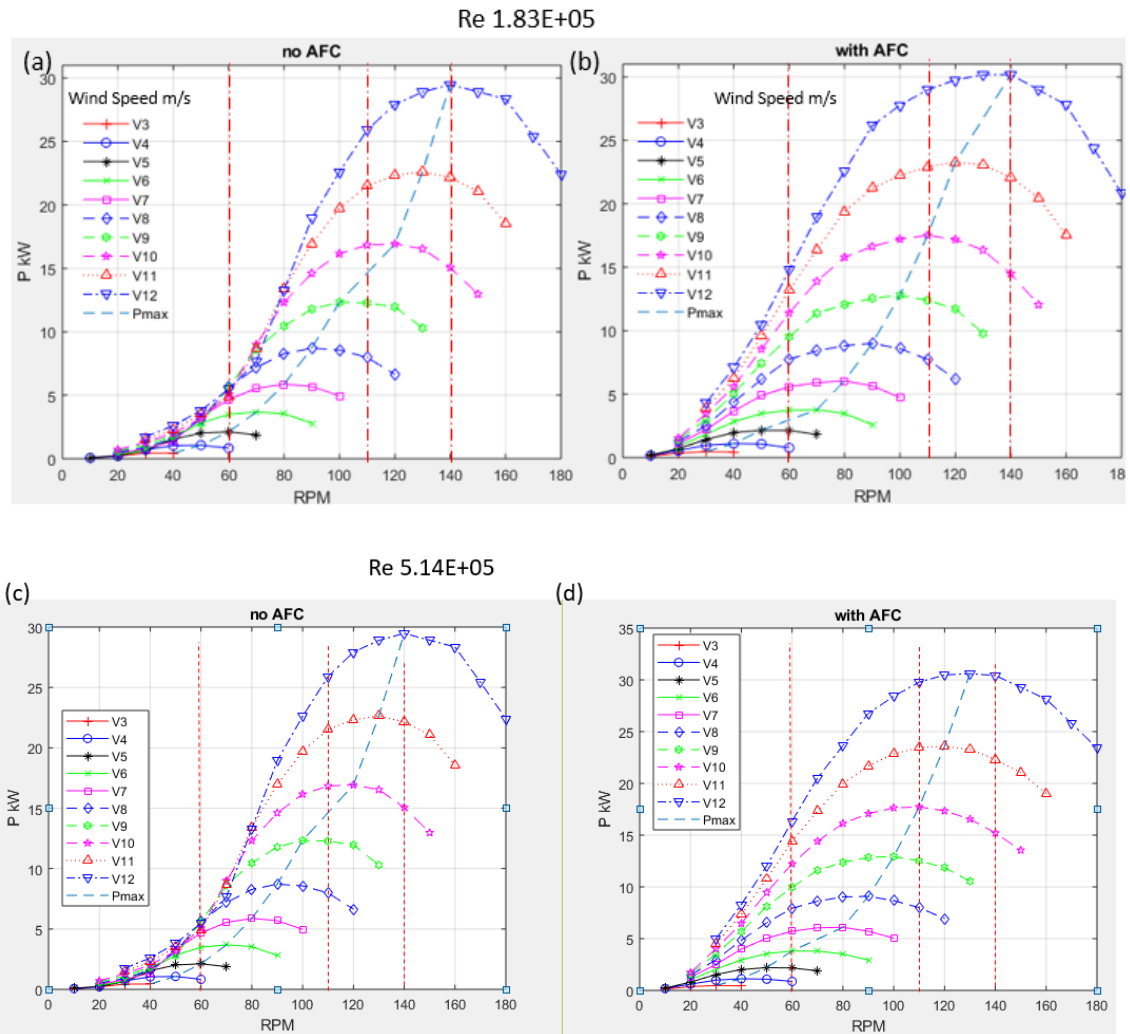
Figure 6-11: Wind turbine power, (a and c) without AFC, and (b and d) with AFC and versus rotational blade speed with multi wind speeds; the vertical (dashed lines for selected blade rotational speeds; the dashed curve marked as 'P_{max}' represented maximum power at any wind speed. (a and b) for lowest Reynolds number and (c and d) for highest Reynolds number.

To extract the maximum possible energy from the wind speed of 4 m/s, the rotational speed most appropriate to low wind speeds is 60 revolutions per minute (rpm). On the other hand, a wind turbine with a rated wind speed of 12 m/s operates at its maximum power at a rotational speed of 140 rpm (Appendix F-1). Nevertheless, in this latter case, the turbine will only produce significant power at wind speeds of 10–12 m/s. To extract significant energy from the intermediate wind speeds, let the rotational speed to be 110 rpm. , in the case of 'with AFC' and at a wind speed of 8 m/s, the wind

111

turbine power at 110 rpm and 60 rpm is the same value (7.75 kW). Using a wind turbine with a lower rotational speed for the same wind capacity is better than using a higher rotational speed because it reduces the wear on the turbine. Therefore, the speed of 8 m/s was considered among low wind speeds at which the turbine would operate at a rotational speed of 60 rpm. So the wind turbine power improvement for a rotational blade speed of 60 rpm; for wind velocities of (4-8 m/s); and for the case with/without AFC, are represented in Figure 6-12
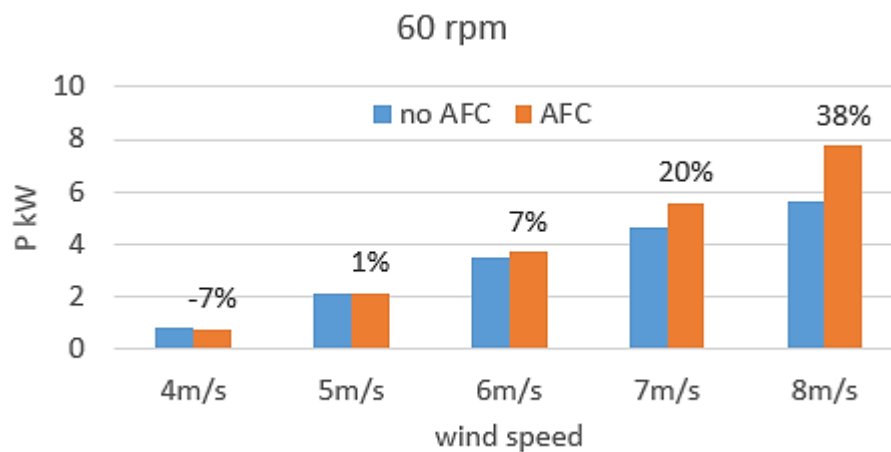
Figure 6-12: The wind turbine power for S822 aerofoil with/without AFC, versus wind speed for the rotational blade speed of 60 rpm.

Figure 6-12 shows that the use of suction technology (for low wind speeds) is appropriate for wind speed (5-8 m/s) and that the rate of improvement increases exponentially with increasing wind speed.

The rated wind speed (V_r) is between 1.5 – 2 of the annual mean wind speed (V_m) for a site (Sedaghat et al., 2017). The annual mean wind speed for Adelaide is 4.3 m/s (Appendix H-2). So the rated wind speed for this site is about 8.6 m/s. So according to Figure 6-11-b, the wind turbine will not generate more than 13kW at 100 rpm. So it is necessary to select a wind turbine with a rated wind speed of 9 m/s in sites like these. However, in Townsville, the annual mean wind speed is 6 m/s. so the rated wind speed will be 12 m/s. Therefore when the wind turbine operates at 60 rpm (for wind speeds of 4-7 m/s) and 110 rpm for wind speeds of 8 and 12 m/s, much energy will be gotten for a range of wind speeds between (4-12 m/s). The maximum power which can be produced from using the wind turbine is 30.40 kW at a rated wind speed of 12 m/s.

In Figure 6-13, the percentages of power coefficient improvements were represented. The average percentage of improvement is 15%.
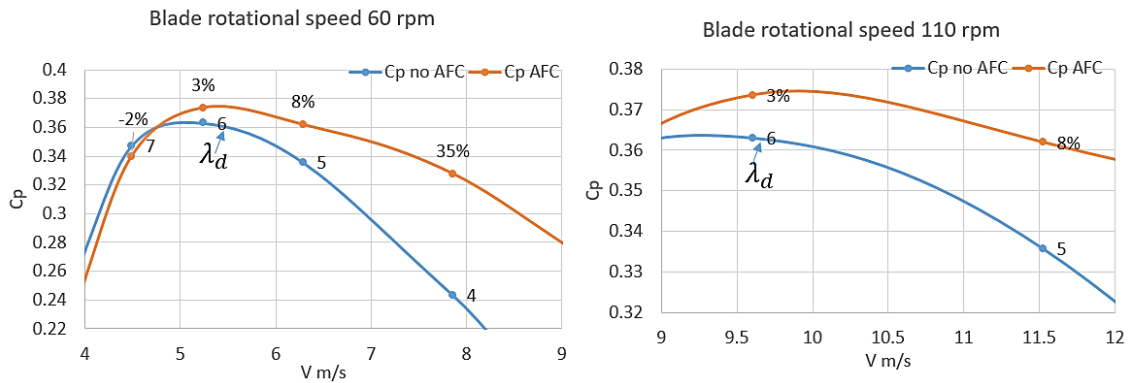
Figure 6-13: The power coefficient, after/before AFC, versus wind speed for blade rotational speed of 60 and 110 rpm with their improvement percentages.

6.4.4 Capacity factor and the annual energy production

The mean wind speed data, Weibull parameters, and the capacity factor data are listed in Appendix H . The capacity factor is an indicator of the amount of wind energy produced in a specific region during a limited period. Mathematically, it can be introduced, as shown in Equation 6-3 (Johnson, 2006).

$$CF = \frac{exp\left[-\left(\frac{V_i}{C_w}\right)^{k_w}\right] - exp\left[-\left(\frac{V_r}{C_w}\right)^{k_w}\right]}{\left(\frac{V_r}{C_w}\right)^{k_w} - \left(\frac{V_i}{C_w}\right)^{k_w}} - exp\left[-\left(\frac{V_o}{C_w}\right)^{k_w}\right] \qquad \text{........} \quad 6\text{-}3$$

Where V_i is the cut-in wind speed; V_o is the cut off wind speed and, V_r is the rated wind speed. C_w and k_w are the scale and shape factors respectively for Weibull parameters and describe the wind speed frequencies for a specific region.

A bar chart of capacity factor (CF) (Appendix H-3), for the selected sites, was implemented. An Australian map was included for the representation of the selected cities. The capacity factor has a significant role in estimating energy production. It can determine the average mean wind turbine power per hour ($Pe.ave$) of a selected wind

turbine when operating at the selected site. Weibull parameters should be provided to calculate the Capacity Factor CF.

The annual energy production for a particular wind turbine is listed in Equation 6-4:

$$E_o = CF.P_r.8756$$ ………..   6-4

Where the mean average power $Pe.ave = CF.P_r$; P_r is the rated power; (8760) is the number of hours per year.

In order to calculate the annual energy production of a particular wind turbine operating in a given location, it is necessary to find the rated wind power (P_r) produced at each wind speed "times the fraction of the time that wind speed is experienced, integrated over all possible wind speeds" (Johnson, 2006).

The rated wind speed and rated power for the selected wind turbine are 12 m/s and 25 kW respectively. Also, the capacity factor for Townsville is 0.237. So the annual energy production for the selected wind turbine is 51.851E+03 kWh. In contrast, the rated wind speed for the improved WT using the suction technique (S1) with the desired aerofoil types (S822 and S823 aerofoils) is 30.4kW. So the annual energy production for the improved WT is 63.050E+03 kWh. So the percentage of energy production improvement is 22%

6.5 Summary

For NREL S822 and S823 aerofoils as specific examples of HAWT blades, the wind turbine performance improvement and enhancements for a low wind speed site were investigated using the suction technique at slot S1. Multi-process was implemented to achieve improved wind turbine performances. The effect of each of the suction velocities, Reynolds number and angle of attack were studied for S822 aerofoil. Suction velocities of -5 m/s for low AoA and -35 m/s for high AoA were utilised with the lowest/highest selected Reynolds number (1.83E+05 and 5.14E+05) respectively. The lift and drag coefficients, as well as, to lift-to-drag ratio, were investigated for both S822 and S823 aerofoils. The lift and drag coefficients were investigated for S822

aerofoil with AFC (S1) techniques for a range of AoA (0-21). Wind turbine performance with/without AFC was predicted. Wind power versus rotational speed for multi wind velocity was predicted. The most productive rotational blade speeds were selected (60 rpm for low wind speeds less than 9 m/s, and 110 rpm for wind speeds greater than 9 m/s). Power coefficient versus wind speed was investigated. The average percentage of wind turbine performance improvement was 15% as a result of the suction technique. The percentage improvement for the improved wind turbine compared with the selected wind turbine (the baseline) was 22%. At a site with low mean wind speeds (like 4.3 m/s for Adelaide), When operating wind turbines (designed to operate in areas with high annual mean wind speeds) in areas with low annual mean wind speeds, much of the power (to be obtained at high annual mean wind speeds) will be lost.

CHAPTER 7: CONCLUSION

In this study, the lack of efficiency of small wind turbines (with a rotor diameter of 10 m) was investigated when operating in areas with low wind speed. A flow separation problem occurs when air passes over the aerofoil of a wind turbine. Therefore, suction and blowing techniques were used as one of the active flow control (AFC) methods available in order to overcome the adverse pressure gradient that causes the boundary layer to separate from the upper aerofoil surface. The primary objective of this study was to improve annual energy production for areas characterized as low wind speeds, by improving the wind turbine performance. Therefore, the specifications utilized were a horizontal axis wind turbine, with two blades, with a diameter of 10 m and a turbine capacity of 25 kW when operating at a rated wind speed of 12 m/s. Referencing data from the National Renewable Energy Laboratory (NREL), the NREL S822 and NREL S823 aerofoil types were identified as the most appropriate types for small-scale, horizontal-axis wind turbines (Table 2-1 in Chapter 2).

In the first Chapter, primary and general information is presented about the need for alternative energy, and about how the wind turbine works with different types of wind rotor. The challenges facing the wind turbine and its performance are discussed, along with some related variables.

In the second Chapter, the aerofoil components and the aerodynamic properties related to the wind turbine blade are defined. After that, the literature reviews relating to flow separation and how to control it in order to improve and maximize the annual energy output of the wind turbine were discussed. Finally, the previous studies and the research gap were discussed.

In the third Chapter, the two prototypes are designed and manufactured for the aerofoils chosen. In the design process, sites for active control technologies (blowing and suction) were identified. Some parts of the wind tunnel necessary for the experimental tests to be accurately performed were also designed and manufactured. Suction and blowing systems and smoke systems were established. The smoke system was vital in order to visualize flow behaviour.

In Chapter four, the models (S822 and S823 aerofoils) was made to simulate the nature of laboratory work using the URANS transient SST (γ-Re_θ) turbulence model via ANSYS Fluent 2020 R1 Academic, to validate the CFD model. A mesh independence study verified that the numerical errors were minimized.

In the fifth Chapter, several tests were performed using the ANSYS program, and their results were compared with the results that were conducted in the laboratory to ensure the validity of the results prepared by CFD.

A simulation study was also conducted on the effect of the adverse pressure gradient on the boundary layer separation. In addition to investigating the role of suction and blowing techniques mitigation of flow separation, it was thus able to identify the optimum techniques to apply at high and low angles of attack (AoA). It was discovered that a suction technique located as close as possible to the leading edge at x/c = 0.18 (S1) was the best technique when considering all AoA among the various techniques tested. A total of 13 tests were performed using different combinations of blowing/suction techniques. The results showed that there was an improvement in aerofoil performance, based on 'the baseline'(no AFC), by 62% with high AoA (18°), and 38% for low AoA (9°). The reason for this is due to its proximity to the leading edge (x / c = 0.18), being upstream of any separation point (located at x / c = 0.23 for angles as high as 18°), therefore always being able to mitigate the adverse pressure gradient which causes separation.

In Chapter Six, an optimization of the best technique is performed. The optimum speeds of these AFC technologies were investigated for low/high AoA (using the S1 technique with a suction velocity of -5 m/s for AoA between 0-11° and -35 m/s for AoA between 12-21°.

Moreover, the momentum lost due to a suction velocity of -35 m/s is substantial (at high AoA), so the adverse pressure gradient (APG) effect will easily be overcome, and the boundary layer remains attached to the upper surface of the aerofoil. At low AoA, the separation point will occur further downstream, enabling suction speeds of -5 m/s to suffice in overcoming the APG. Using large suction speeds at low AoA will generate a laminar separation bubble (LSB) and thus reduce the lift to drag ratio.

Furthermore, the lift and drag coefficients were investigated for a wide range of AoA (0-21°) for low Reynolds numbers (1.83E+05 and 5.14E+05). Subsequently, these values were used as inputs to the WT performance prediction program (Appendix E-1). The results revealed that the improvement rate at low Reynolds number with high AoA was better than at high Reynolds number. The reason for this is due to the suction velocity (-35 m/s) being greater than the inlet velocity (15.8 m/s). In the case of higher Reynolds number, the suction velocity (-35 m/s) was less than the inlet velocity (45 m/s).

There is no doubt that the use of the NREL S822 and NREL S823 aerofoils (with 'no AFC'), which served as the baseline for the flow separation treatment, contributed to making the wind turbine more efficient than it originally was.

Wind turbines should operate in regions with a mean annual wind speed consistent with the rated wind speed of the turbine. Therefore, for instance, in Adelaide, the annual mean wind speed is 4.3 m/s (Appendix H-2), so the rated wind speed will be 8.6 m/s (based on $V_r = (1.5 - 2)V_m$). This means that a wind turbine with a rated speed of 12 m/s and a rated power of 30 kW will only produce 13 kW at a rated wind speed close to 9 m/s. Here, much potential energy that this turbine could generate will be lost if it was to operate in regions with rated wind speeds of 6 m/s. The amount of increase in mean annual wind speed is small (4.3 to 6 m/s), but the amount of power is proportional to the wind speed cubed, and this is what generates substantial amounts of power.

Finally, the results revealed that the use of the NREL S822 and S823 aerofoils with AFC enhance the wind turbine performance by an average of 15% compared with using 'no AFC'. Moreover, the annual energy production will be improved, by using the improved wind turbine blade (with AFC S1), by 22% compared with annual energy production by using the selected wind turbine (no AFC and no using of S822 and S823 aerofoils). On the other words, 15%, the baseline is the using S822 without AFC. The improvement was made using AFC, while, 22%, the baseline is the using the actual wind turbine (unknown aerofoil type as shown in appendix F-1), the progress was made using AFC.

SUGGESTED FUTURE WORKS

It can be added some suggestion and recommendation future works like:

- Design and manufacture a small wind turbine using S1 slot and testing in a large-scale wind tunnel.

- Rotational Effects on Flow Separation when using S1 technique

- Using the solar energy to operate the pump for S1 technique

- developing an optimal airfoil section along with the S1 system for low speed wind turbines.

REFERENCES

ABRAHAM, J. P. & PLOURDE, B. 2014. *Small-Scale Wind Power : Design, Analysis, and Environmental Impacts,* New York, UNITED STATES, Momentum Press.

AFTAB, S. M. A., MOHD RAFIE, A. S., RAZAK, N. A. & AHMAD, K. A. 2016. Turbulence Model Selection for Low Reynolds Number Flows. *PloS one,* 11**,** e0153755-e0153755.

AIRFOILTOOLS.COM 2020. NREL's S822 Airfoil (S822-Nr) Xfoil Prediction Polar At RE=500,000 Ncrit=9.

ALI, A. M. 2014. *Aerodynamic optimisation of small scale horizontal axis wind turbine blades.* Master of Engineering, RMIT University.

BAHRAMI, A., TEIMOURIAN, A., OKOYE, C. O. & SHIRI, H. 2019. Technical and economic analysis of wind energy potential in Uzbekistan. *Journal of Cleaner Production,* 223**,** 801-814.

BAVANISH, B. & THYAGARAJAN, K. 2013. Optimization of power coefficient on a horizontal axis wind turbine using bem theory. *Renewable and Sustainable Energy Reviews,* 26**,** 169-182.

BENIM, A. C., DIEDERICH, M., GÜL, F., OCLON, P. & TALER, J. 2018. Computational and experimental investigation of the aerodynamics and aeroacoustics of a small wind turbine with quasi-3D optimization. *Energy Conversion and Management,* 177**,** 143-149.

BIN, W., YONGQIANG, L., NAVID, Z. & SAMIR, K. 2011. Fundamentals of Wind Evergy Conversion System Control. *Power Conversion and Control of Wind Energy Systems.* Wiley-IEEE Press.

BUHL, M. 2012. *Wind Turbine Airfoil Families.* [Online]. Available: https://wind.nrel.gov/airfoils/AirfoilFamilies.html [Accessed].

BURTON, T., JENKINS, N., SHARPE, D. & BOSSANYI, E. 2011. Wind Energy Handbook (2nd Edition). John Wiley & Sons.

BUSBY, R. L. 2012. Wind Power - The Industry Grows Up. PennWell.

CAI, X., GU, R., PAN, P. & ZHU, J. 2016. Unsteady aerodynamics simulation of a full-scale horizontal axis wind turbine using CFD methodology. *Energy Conversion and Management,* 112**,** 146-156.

CALAUTIT, J. K., CHAUDHRY, H. N., HUGHES, B. R. & SIM, L. F. 2014. A validated design methodology for a closed-loop subsonic wind tunnel. *Journal of Wind Engineering and Industrial Aerodynamics,* 125**,** 180-194.

CAO, H. 2011. *Aerodynamics Analysis of Small Horizontal Axis Wind Turbine Blades by Using 2D and 3D CFD Modelling.* MSc (by Research), University of the Central Lancashire Preston, England.

CATTAFESTA, L., BAHR, C. & MATHEW, J. 2010. Fundamentals of Wind-Tunnel Design.

CERMAK, J. E. 2003. Wind-tunnel development and trends in applications to civil engineering. *Journal of Wind Engineering and Industrial Aerodynamics,* 91**,** 355-370.

CHAWLA, J. S., SURYANARAYANAN, S., PURANIK, B., SHERIDAN, J. & FALZON, B. G. 2014. Efficiency improvement study for small wind turbines through flow control. *Sustainable Energy Technologies and Assessments,* 7**,** 195-208.

CHEN, J., WANG, Q., CHINA SCIENCE, P., MEDIA LTD, S. & SUN, Z. 2017. *Wind Turbine Airfoils and Blades : Optimization Design Theory,* Berlin/Boston, GERMANY, De Gruyter, Inc.

CHENG, M. & ZHU, Y. 2014. The state of the art of wind energy conversion systems and technologies: A review. *Energy Conversion and Management,* 88**,** 332-347.

CORTEN, G. P. 2001. *Flow Separation on Wind Turbine Blades.* Ph.D. Thesis dissertation., Utrecht University

DAI, J., LIU, D., WEN, L. & LONG, X. 2016. Research on power coefficient of wind turbines based on SCADA data. *Renewable Energy,* 86**,** 206-215.

DARWISH, A. S., SHAABAN, S., MARSILLAC, E. & MAHMOOD, N. M. 2019. A methodology for improving wind energy production in low wind speed regions, with a case study application in Iraq. *Computers & Industrial Engineering,* 127**,** 89-102.

DIWAN, S. S. & RAMESH, O. N. 2007. Laminar separation bubbles: Dynamics and control. *Sadhana,* 32**,** 103-109.

DUMITRACHE, A., FLORIN, F., HORIA, D. & CARDOS, V. 2014. *Blowing jets as a circulation flow control to enhancement the lift of wing or generated power of wind turbine.*

FAYED, I. M. 2007. Effects of internal Acoustic Excitation on the Improvementof Airfoil Performance. *Ai-Khawarizmi engineering journal,* 3**,** 66-88.

FAYED, I. M., MOHAMMED, A. K., SHIHAB, I. M. & ABED, K. N. 2009. Improvement of dynamics properties of NACA 23015 wing model using internal voice action techniques. *AL-TAQANI,* 22**,** A49-A63.

FENG, L.-H., CHOI, K.-S. & WANG, J.-J. 2015. Flow control over an airfoil using virtual Gurney flaps. *Journal of Fluid Mechanics,* 767**,** 595-626.

FLAVIN, C. 1999. Wind power sets new record as fastest growing energy source. 1.

GENÇ, M. S., AÇıKEL, H. H., AKPOLAT, M. T., ÖZKAN, G. & KARASU, İ. 2016. Acoustic Control of Flow over NACA 2415 Airfoil at Low Reynolds Numbers. *Journal of Aerospace Engineering,* 0**,** 04016045.

GENÇ, M. S., KARASU, İ. & HAKAN AÇıKEL, H. 2012. An experimental study on aerodynamics of NACA2415 aerofoil at low Re numbers. *Experimental Thermal and Fluid Science,* 39**,** 252-264.

GENÇ, M. S., KAYNAK, Ü. & YAPICI, H. 2011. Performance of transition model for predicting low R e aerofoil flows without/with single and simultaneous blowing and suction. *European Journal of Mechanics / B Fluids,* 30**,** 218-235.

GROSS, A. & FASEL, H. 2017. *ESFuelCell2011-54128 FLOW CONTROL FOR WIND TURBINE AIRFOIL.*

GUIDOLIN, M. & ALPCAN, T. 2019. Transition to sustainable energy generation in Australia: Interplay between coal, gas and renewables. *Renewable Energy,* 139**,** 359-367.

GWEC 2019. Global Wind Energy Council (GWEC). *Global Wind Report 2019.*

HANSEN, K., KELSO, R., CHOUDHRY, A. & ARJOMANDI, M. 2014. *Laminar Separation Bubble Effect on the Lift Curve Slope of an Airfoil*.

HOWARTH, L. 1960. Theory of Wing Sections. *Physics Bulletin,* 11**,** 279-279.

HU, H. & YANG, Z. 2008. An Experimental Study of the Laminar Flow Separation on a Low-Reynolds-Number Airfoil. *Journal of Fluids Engineering,* 130**,** 051101-051101-11.

JAHANMIRI, M. 2010. Active flow control: a review. Chalmers University of Technology.

JALAL, M. J., ASSIM, H. Y. & YASSER AHMED, M. 2010. Control of Separation For NACA 2412 Airfoil At Different Angles of Attack Using Air Blowing *Engineering & Technology Journal* 28**,** 5138-5150.

JAWAD, A. M., KHELIFA, M. Z., ABDULLATEEF, M. S. & MAHMOOD, Y. A. 2014. Enhancement of Wind Turbine Performance Using Air- Blowing Technique by Modified Strong Implicit Procedure (MSIP) Optimization Solver Method. *Engineering & Technology Journal,* 32**,** 1580-1601.

JOHNSON, G. L. 2006. *Wind Energy Systems*

JOHNSON, S. J. & DAM, C. P. C. V. 2008. *Active Load Control Techniques for Wind Turbines.* University of California.

KHUDER, N. A. & ITIMAD, D. J. A. 2015. Control of flow separation over NACA 0015 airfoil using synthetic jet actuators *Diyala journal of engineering sciences* 8**,** 674-685.

KOCA, K., GENÇ, M. S., AÇıKEL, H. H., ÇAĞDAŞ, M. & BODUR, T. M. 2018. Identification of flow phenomena over NACA 4412 wind turbine airfoil at low Reynolds numbers and role of laminar separation bubble on flow evolution. *Energy,* 144**,** 750-764.

LANGTRY, R. B. & MENTER, F. R. 2009. Correlation-Based Transition Modeling for Unstructured Parallelized Computational Fluid Dynamics Codes. *AIAA Journal,* 47**,** 2894-2906.

LANZAFAME, R. & MESSINA, M. 2009. Design and performance of a double-pitch wind turbine with non-twisted blades. *Renewable Energy,* 34**,** 1413-1420.

LE GOURIERES, D. 1982. Wind power plants: theory and design.

LE GOURIÉRÈS, D. 1982. CHAPTER IV - HORIZONTAL-AXIS WIND TURBINES DESIGN OF THE BLADES AND DETERMINATION OF THE FORCES ACTING ON THE WIND POWER PLANT. *In:* LE GOURIÉRÈS, D. (ed.) *Wind Power Plants.* Pergamon.

LEE, M.-H., SHIAH, Y. C. & BAI, C.-J. 2016. Experiments and numerical simulations of the rotor-blade performance for a small-scale horizontal axis wind turbine. *Journal of Wind Engineering and Industrial Aerodynamics,* 149**,** 17-29.

LEI, J., GUO, F. & HUANG, C. 2013. Numerical study of separation on the trailing edge of a symmetrical airfoil at a low Reynolds number. *Chinese Journal of Aeronautics,* 26**,** 918-925.

LENGANI, D., SIMONI, D., UBALDI, M., ZUNINO, P. & BERTINI, F. 2011. Application of a Synthetic Jet to Control Boundary Layer Separation under Ultra-High-Lift Turbine Pressure Distribution. *Flow Turbulence and Combustion,* 87**,** 597-616.

LI, H. X., EDWARDS, D. J., HOSSEINI, M. R. & COSTIN, G. P. 2020. A review on renewable energy transition in Australia: An updated depiction. *Journal of Cleaner Production,* 242**,** 118475.

LIANG, Y.-B., ZHANG, L.-X., LI, E.-X., LIU, X.-H. & YANG, Y. 2014. Design Considerations of Rotor Configuration for Straight-Bladed Vertical Axis Wind Turbines. *Advances in Mechanical Engineering,* 2014**,** 1-15.

LIM, N. R. E., DIMAGIBA, R., UBANDO, A., GONZAGA, J. & AUGUSTO, G. FEA of Thermal Warpage in Ball Grid Array with Consideration of Molding Compound Residual Strain Compared to Experimental Measurements. 2018 IEEE 10th International Conference on Humanoid, Nanotechnology, Information Technology,Communication and Control, Environment and Management (HNICEM), 29 Nov.-2 Dec. 2018 2018. 1-5.

MAEDA, M. & WATTS, D. 2019. The unnoticed impact of long-term cost information on wind farms' economic value in the USA. – A real option analysis. *Applied Energy,* 241**,** 540-547.

MAHMOOD, N. M. 2011. COMPUTER PROGRAM TO PREDICT PERFORMANCE OF FAST RUNNING HORIZONTAL AXIS WIND TURBINE TO REACHING THE OPTIMUM DESIGN. *DIYALA JOURNAL OF ENGINEERING SCIENCES,* 4**,** 57-71.

MAHMOOD, N. M. & ABBAS, M. K. 2011. Computer program to predict performance of fast running horizontal axis wind turbine to reaching the optimum design. *Diyala Journal of Engineering Sciences,* 4**,** 57-71.

MALALASEKERA, H. K. V. A. W. 2007. An Introduction to Computational Fluid Dynamics.

MALDONADO, V., FARNSWORTH, J., GRESSICK, W. & AMITAY, M. 2010. Active control of flow separation and structural vibrations of wind turbine blades. *Wind Energy,* 13**,** 221-237.

MALDONADO, V. & GUPTA, S. 2017. Active Flow Control of a Low Reynolds Number S809 Wind Turbine Blade Model under Dynamic Pitching Maneuvers. *Open Journal of Fluid Dynamics,* Vol.07No.02**,** 17.

MÜLLER-VAHL, H. S., CHRISTOPH; NAYERI, CHRISTIAN; PASCHEREIT, CHRISTIAN;GREENBLATT, DAVID 2015. *Control of Thick Airfoil, Deep Dynamic Stall Using Steady Blowing*.

MURTY, P. S. R. 2017. Chapter 24 - Renewable Energy Sources. *In:* MURTY, P. S. R. (ed.) *Electrical Power Systems.* Boston: Butterworth-Heinemann.

NAAMA, F. Z., ZEGAOUI, A., BENYESSAD, Y., KESSAISSIA, F. Z., DJAHBAR, A. & AILLERIE, M. 2019. Model and Simulation of a Wind Turbine and its Associated Permanent Magnet Synchronous Generator. *Energy Procedia,* 157**,** 737-745.

NATARAJAN, A. 2014. An overview of the state of the art technologies for multi-MW scale offshore wind turbines and beyond. *Wiley Interdisciplinary Reviews: Energy and Environment,* 3**,** 111-121.

OUKASSOU, K., MOUHSINE, S. E., HAJJAJI, A. E. & KHARBOUCH, B. 2019. Comparison of the power, lift and drag coefficients of wind turbine blade from aerodynamics characteristics of Naca0012 and Naca2412. *Procedia Manufacturing,* 32**,** 983-990.

RAM, K. R., LAL, S. & RAFIUDDIN AHMED, M. 2013. Low Reynolds number airfoil optimization for wind turbine applications using genetic algorithm. *Journal of Renewable and Sustainable Energy,* 5.

REZAEIHA, A., MONTAZERI, H. & BLOCKEN, B. 2019. On the accuracy of turbulence models for CFD simulations of vertical axis wind turbines. *Energy,* 180**,** 838-857.

RICCI, R., MONTELPARE, S. & RENZI, E. 2011. Study of mechanical disturbances effects on the laminar separation bubble by means of infrared thermography. *International Journal of Thermal Sciences,* 50**,** 2091-2103.

RICCI, R., MONTELPARE, S. & SILVI, E. 2007. Study of acoustic disturbances effect on laminar separation bubble by IR thermography. *Experimental Thermal and Fluid Science*, 31**,** 349-359.

SCHLICHTING, H. 2017. *Boundary-Layer Theory,* Berlin, Heidelberg, Springer Berlin Heidelberg.

SCHUBEL, P. J. & CROSSLEY, R. J. 2012. Wind Turbine Blade Design Review. *Wind engineering,* 36**,** 365-388.

SEDAGHAT, A., HASSANZADEH, A., JAMALI, J., MOSTAFAEIPOUR, A. & CHEN, W.-H. 2017. Determination of rated wind speed for maximum annual energy production of variable speed wind turbines. *Applied Energy,* 205**,** 781-789.

SEDIGHI, H., AKBARZADEH, P. & SALAVATIPOUR, A. 2020. Aerodynamic performance enhancement of horizontal axis wind turbines by dimples on blades: Numerical investigation. *Energy,* 195**,** 117056.

SERDAR GENÇ, M., KARASU, L., HAKAN AÇKEL, H. & AKPOLAT, T. 2012. *Low Reynolds Number Flows and Transition*.

SERDAR GENÇ, M. & KAYNAK, Ü. 2009. *Control of Laminar Separation Bubble over a NACA2415 Aerofoil at Low Re Transitional Flow Using Blowing/Suction*.

SHAH, H., MATHEW, S. & LIM, C. M. 2015. Numerical simulation of flow over an airfoil for small wind turbines using the γ-Reθ model. *International journal of energy and environmental engineering,* 6**,** 419-429.

SHENG, C., 2017. Introduction. *Advances in Transitional Flow Modeling: Applications to Helicopter Rotors.* Cham: Springer International Publishing.

SHEPHERD, D. G. 1984. Note on a Simplified Approach to Design Point Performance Analysis of HAWT Rotors. *Wind Engineering,* 8**,** 122-130.

SHKARA, Y. M. 2014. *Aerodynamic Analysis and Optimum Blade Design of HAWT Rotor with Winglet.* the Degree of Master, University of Technology - Baghdad.

SINGH, R. K. & AHMED, M. R. 2013. Blade design and performance testing of a small wind turbine rotor for low wind speed applications. *Renewable Energy,* 50**,** 812-819.

SØRENSEN, J. N. 2011. Aerodynamic Aspects of Wind Energy Conversion. *Annual Review of Fluid Mechanics,* 43**,** 427-448.

STALNOV, O., STALNOV, O., KRIBUS, A. & SEIFERT, A. 2010. Evaluation of active flow control applied to wind turbine blade section. *Journal of renewable and sustainable energy,* 2**,** 63101.

SUN, Z., CHEN, J., SHEN, W. Z. & ZHU, W. J. 2016. Improved blade element momentum theory for wind turbine aerodynamic computations. *Renewable Energy,* 96, Part A**,** 824-831.

TANGIER, J. L. & SOMERS, D. M. 1995. NREL Airfoil Families for HAWTs

VENNELL, R. 2013. Exceeding the Betz limit with tidal turbines. *Renewable Energy,* 55**,** 277-285.

WALKER, R. P. 2015. *Wind energy essentials : societal, economic, and environmental impacts,* Hoboken, New Jersey, John Wiley & Sons, Inc.

WILCOX, D. C. 2006. *Turbulence modeling for CFD,* La Cãnada, Calif, DCW Industries.

WOOD, D. 2011. Small Wind Turbines: Analysis, Design, and Application.

YAN, L. 2020. Straight-Bladed Vertical Axis Wind Turbines: History, Performance, and Applications.

YARAMASU, V. 2016. *Model Predictive Control of Wind Energy Conversion Systems,* Place of publication not identified, John Wiley and Sons, Inc.

YARUSEVYCH, S., KAWALL, J. G. & SULLIVAN, P. E. 2003. Effect of Acoustic Excitation on Airfoil Performance at Low Reynolds Numbers. *AIAA Journal,* 41**,** 1599-1601.

YARUSEVYCH, S. & KOTSONIS, M. 2016. Effect of Local DBD Plasma Actuation on Transition in a Laminar Separation Bubble. *Flow, Turbulence and Combustion***,** 1-22.

YARUSEVYCH, S., SULLIVAN, P. E. & KAWALL, J. G. 2007. Effect of acoustic excitation amplitude on airfoil boundary layer and wake development. *AIAA Journal,* 45**,** 760-771.

YOU, D. & MOIN, P. 2008. Active control of flow separation over an airfoil using synthetic jets. *Journal of Fluids and Structures,* 24**,** 1349-1357.

ZHU, F.-W., DING, L., HUANG, B., BAO, M. & LIU, J.-T. 2020. Blade design and optimization of a horizontal axis tidal turbine. *Ocean Engineering,* 195**,** 106652.

ZIFENG, Y., HAAN, F. L., HU, H. & HONGWEI, M. An experimental investigation on the flow separation on a low-reynolds-number airfoil. 2007 2007. 3421-3431.

APPENDICES

Appendix A

A-1 The wind tunnel fan utilized in the tests

PACIFICHVAC
ENGINEERING   **CHICAGO BLOWER**

TECHNICAL AND PRICE SCHEDULE. SUBJECT TO OUR STANDARD CONDITIONS OF SALE.

SALES ENGINEER : Lee Woodruff   DATE : 11/04/2018
                                                  QUOTATION : CB1804-219A

CUSTOMER : University of Southern Queensland
PROJECT : Low Speed Wind Tunnel   ITEM 1
ITEM REF : A   QTY 1

FAN SELECTED   SWSI-D53 F2 Size 521-100%
CONFIGURATION   Single Width CW180
DRIVE TYPE   Direct Driven Arrangement 4
CLASS   4
ROTOR TYPE   Backward Inclined
IMPELLER DIAMETER   521mm Over Blades.

PERFORMANCE DETAILS   DESIGN DUTY
INLET FLOW (ACTUAL) M3/S   1.2
DISCHARGE PRESSURE KPA   4
INLET PRESSURE KPA   -0 (Fan Static Pressure)
SELECTION TEMPERATURE °C   20
MAX INLET TEMPERATURE °C   40
ELEVATION metres   0
INLET DENSITY Kg/m3   1.2

FAN SPEED rpm   2955
OUTLET VELOCITY m/sec   37.1
TIP SPEED m/sec   80.6
SHAFT POWER at 20°C.   8.000 kW
FAN EFFICIENCY %   59.4
TEMPERATURE RISE °C   5.5
SHAFT POWER at 20°C. kW   8.000 kW

MOTOR DETAIL WEG W21 : 11 kW; 2 pole; Frame : D160M.
(Sized for starting using a variable speed drive) ELECTRICAL SUPPLY : 415-3-50Hz

CONSTRUCTION MATERIALS Grade 250 Casing.   Grade 250 Impeller.
EXTERNAL FINISH   Standard enamel (Dulux Luxol 4QD or similar) 1 Coat + 1 Coat GOZP
INTERNAL FINISH   GOZP 1 coat of primer only

DELIVERY : EX WORKS ST MARYS NSW

EQUIPMENT INCLUDED :
Electric Motor   Drain socket and plug
Shaft seal.

PRICE EACH ... $3,225.00 + GST
PRICE EACH (INCL TAX)... $3,547.50

Pacific Hvac

Phone : 61-2-4647 8066
Fax : 61-2-4647 8069

Customer : University of Southern Queensland
Project : Low Speed Wind Tunnel
Item 1 - Ref : A

PACIFICHVAC ENGINEERING — **CHICAGO BLOWER**

Quote Ref : CB1804-219A
11/04/2018

Gas Properties :

Barom Pressure :	101.325	kpa
Operating Temp :	20	Deg.C.
Humidity :	38	%
Specific Gravity :	1.0	
Inlet Density :	1.2	Kg/m3

Duty Required :

Inlet Volume Flow :	1.2	m3/s
Fan Static Pressure :		
Inlet Pressure :	-0	kpa
Outlet Pressure :	4	kpa

Fan Selected :

SWSI-D53 F2 Size 521-100%

Speed :	2955	Rpm
Impeller Ø :	521	mm
Fan Class :	4	
Maximum Rpm :	5040	Note 1

Fan Shaft Power :

@ 20 Deg C :	8.000	kW
@ Duty Temp :	8.000	kW
Tip Speed :	80.6	m/s
Inlet Velocity :	33.7	m/s
Outlet Velocity :	37.1	m/s
Temp Rise :	5.5	Deg.C.

Duty : 1.2 M3/S @ 4 KPA @ 20 Deg.C.

Fan Power kW

Fan Static Pressure KPA

Volume Flow M3/S X 0.1
Test data to AMCA standards 210 and 300 Prog V391.15
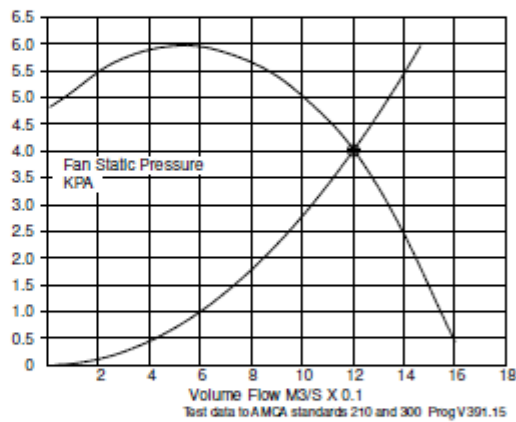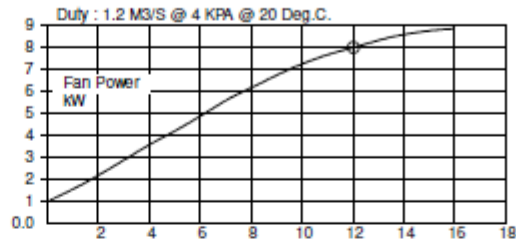
Noise Details :

	63 Hz	125 Hz	250 Hz	500 Hz	1 kHz	2 kHz	4 kHz	8 kHz	Total
Internal SWL dB	102	106	101	95	89	86	80	78	**109**
Free Inlet SPL dBA	47	67	75	78	78	76	70	66	**83**
Free Outlet SPL dBA	47	67	75	78	78	76	70	66	**83**
Outside Casing dBA	52	65	63	63	60	58	52	46	**70**

Motor noise is NOT included in the figures above. Average dBA for Motor at 1 metre is 67

Sound Pressure levels (SPL) assume Free Field Hemispherical Radiation at 1 metre(s)
Breakout at 1 metre from 4 mm thick casing (inside Near Field range).
Casing levels assume the inlet / outlet are ducted and noise does not breakout through duct.
All values are averages. Free Inlet assumes that outlet is ducted and vice versa.

Note 1) The max rpm may require a larger motor and/or upgraded drive components.

431 500
500 50 50
571
440
213 I/S
527

573 157
152 I/S SCROLL
81
406 160 50
219 I/S FLANGE
299 Ø/DIA
8 HOLES Ø10 ON 263 PCD OFF CRS
DRAIN
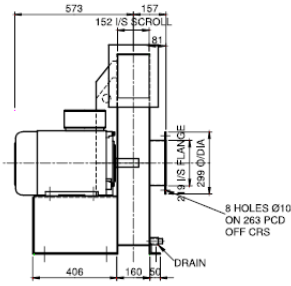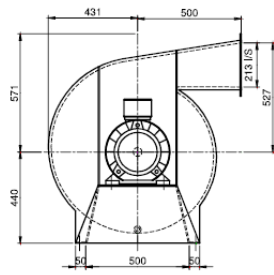
CLIENT : University of Southern Queensland
TAG : A
DUTY
INLET VOLUME : 1.2 AM3/S
STATIC PRESSURE : 4 KPA
TEMPERATURE : 20 °C
SPEED : 2955 RPM
POWER : 8 kW
MOTOR : 11 kW 2 POLE
FRAME D160M
415-3-50Hz

FOUNDATION LOADS
OUT OF BALANCE : NORMAL : 38.75 N
MAXIMUM : 5032.40 N
AXIAL THRUST : 123.92 N
TOTAL WEIGHT : 240 KG
ACCESSORIES :
DRAIN
SHAFT SEAL
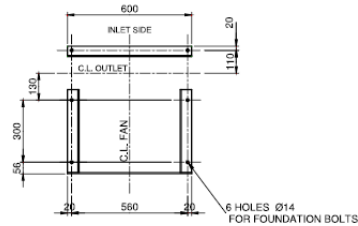
600 20
INLET SIDE
110
C.L. OUTLET
130
300
C.L. FAN
50
20 560 20
6 HOLES Ø14 FOR FOUNDATION BOLTS
PLAN VIEW FROM ABOVE SHOWING FOUNDATION BOLT HOLE DRILLING
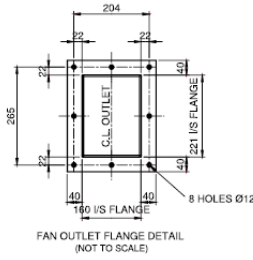
204 22
22
22
265
C.L. OUTLET
40
221 I/S FLANGE
40
40 40
160 I/S FLANGE
8 HOLES Ø12
FAN OUTLET FLANGE DETAIL (NOT TO SCALE)

		DRAWN Y.N	DATE 11/04/18	Pacific Hvac		REVISION A
		SCALE 1 : 13	JOB NO. CB1804-219A		3rd ANGLE PROJECTION	
		THIS DRAWING IS THE PROPERTY OF Pacific Hvac AND MUST NOT BE USED OR REPRODUCED WITHOUT PERMISION		SWSI-D53 F2 Size 521-100% GENERAL ARRANGEMENT DRAWING	DRG No	
A	11/04/18	ORIGINAL ISSUE				
REV.	DATE	DESCRIPTION				

A-2 Smoke generator system

Complete Smoke Generator System Manual
V11.1

AEROLAB

Controls and Connections

Top View of Base/Power Unit

PRESSURE REGULATOR – Allows the Operator to adjust the compressed air pressure in the smoke fluid reservoir.

PRESSURE GAUGE – Indicates the current air pressure within the smoke fluid reservoir.

FLUID FILLER PLUG – A screw-in cap for the smoke fluid reservoir.

TEMPERATURE CONTROLLER – Calibrated and set at AEROLAB, this component maintains correct smoke wand temperature.

FLUID FLOW – This knob controls smoke fluid flow from the reservoir to the smoke wand.

POWER – This switch powers the base/power unit and the smoke wand.

A-3   Pitot tube process calibration

In order to calibrate the Pitot tube meter, a set of devices were used in the calibration system (Figure A-1). In this process, (a) an air compressor, (b) Omega flow meter (used to measure the mass flow rate); (c) Venturi-meter, and (d) the pitot-static tube was connected in series on the same flow stream.
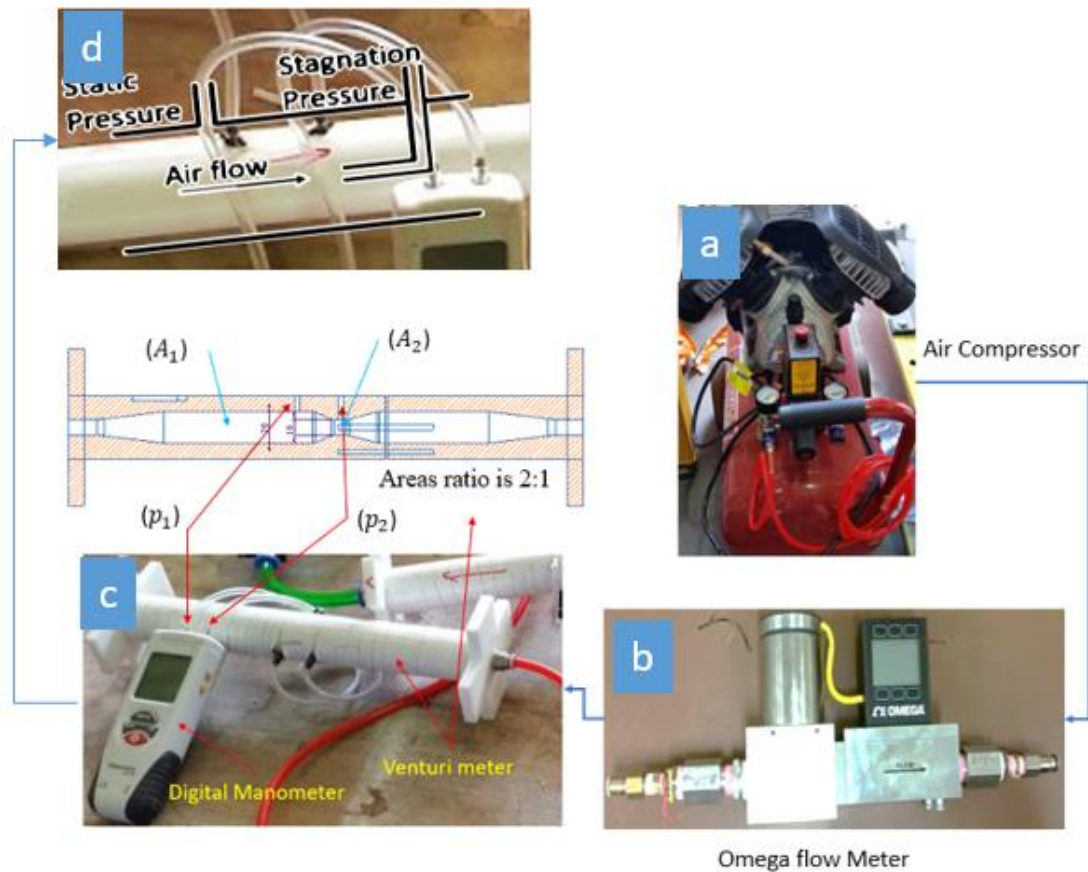
Figure A-1: The pitot tube calibration process

In the Venturi meter (c), according to the principle of Bernoulli's equation, the pressure difference is caused by reducing the cross-sectional area of the flow through the pipe. Therefore, the volumetric flow rate can be found from:

$$Q = A_1 \sqrt{\frac{\frac{2}{\rho}(p_1 - p_2)}{\left(\frac{A_1}{A_2}\right)^2 - 1}} \quad \ldots\ldots\ldots\ldots\ldots\ldots\text{.D-1}$$

Where Q is the volumetric flow rate (m^3/s) ; P_1 and P_2 are the measured pressures (via digital manometer) at point 1 and point 2 respectively; the ratio of areas was $A_1 : A_2 = 2 : 1$. The 'A' is the cross-sectional area, at points 1 and 2.

In the Pitot - static tube formula, the stagnation pressure is equal to the sum of the static pressure and dynamic pressure. So the velocity through a pipe can be expressed as:

$$V_p = \sqrt{\frac{2(P_t - P_s)}{\rho}} \quad \ldots\ldots\ldots\ldots\text{..D-2}$$

Where: V_p is the flow velocity in the Pitot tube pipe; P_t is the total pressure; and P_s is the static pressure.

The readings of the mass flow rate for connected devices were recorded and compared.

Appendix B

B-1 Calculations of static pressure at the test section

P_2=?

V_2=15.8 m/s

$A_2 = 0.09\ m_2$

Point 2

All Units in mm   720

370   300

770

500

793

300

P_1=0 Pa

V_1=?

$A_1 = 0.5929 m^2$

Point 1
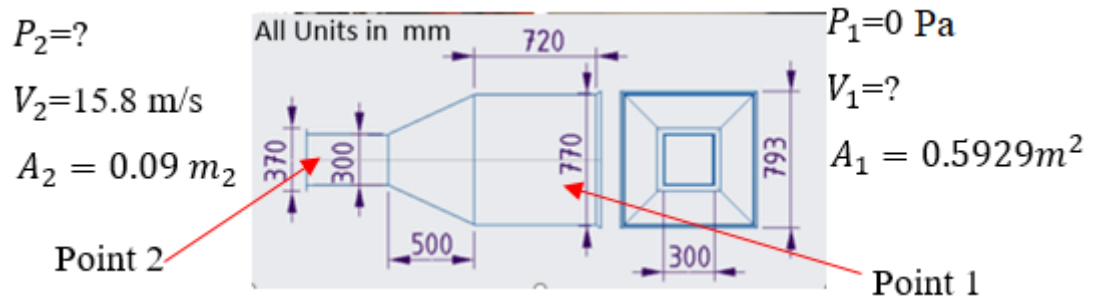
Figure B-1: Schematics of the wind tunnel entrance

Flow Rate = Flow Area × Flow Velocity

$V_1 = 2.4$

Bernoulli's Equation Formula:

$$\frac{P_1}{\gamma} + \frac{V_1^2}{2g} + z_1 = \frac{P_2}{\gamma} + \frac{V_2^2}{2g} + z_2$$

B-2 The mesh quality on the base of skewness cell quality type for NREL S822 aerofoil

Case 1

Mesh Metric	Skewness
Min	3.8937e-007
Max	0.83667
Average	4.4641e-002
Standard Deviation	6.8531e-002

Nodes 11559
Element 22491

Case 2

Mesh Metric	Skewness
Min	8.7684e-007
Max	0.64386
Average	4.1505e-002
Standard Deviation	4.8587e-002

Nodes 17095
Elements 33116

Case 3

Mesh Metric	Skewness
☐ Min	1.034e-007
☐ Max	0.57588
☐ Average	3.6565e-002
☐ Standard Deviation	4.0974e-002

	Tri3
☐ Nodes	29427
☐ Elements	57141

Case 4

Mesh Metric	Skewness
☐ Min	5.0887e-009
☐ Max	0.5619
☐ Average	3.3808e-002
☐ Standard Deviation	3.7831e-002

	Tri3
☐ Nodes	48296
☐ Elements	94269

135

Figure B-2: Skewness mesh metric with the number of cells for S822 aerofoil

Appendix C

C-1 Flow visualisations around the aerofoil model of S822 aerofoil using suction and blowing techniques
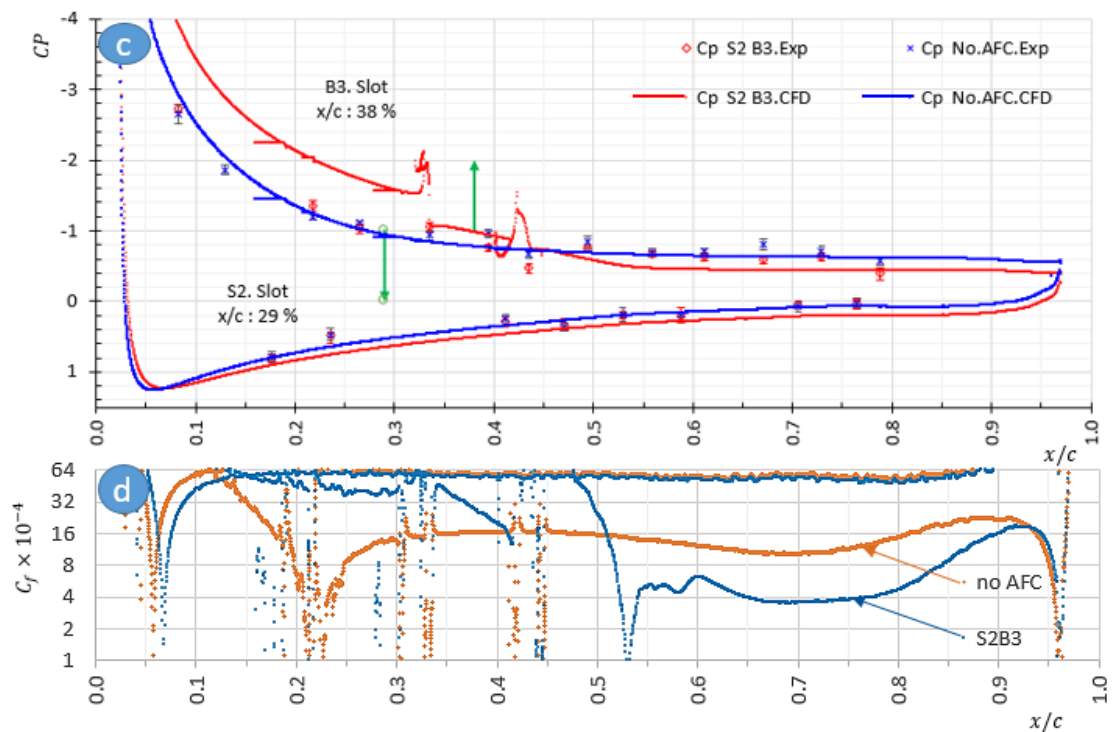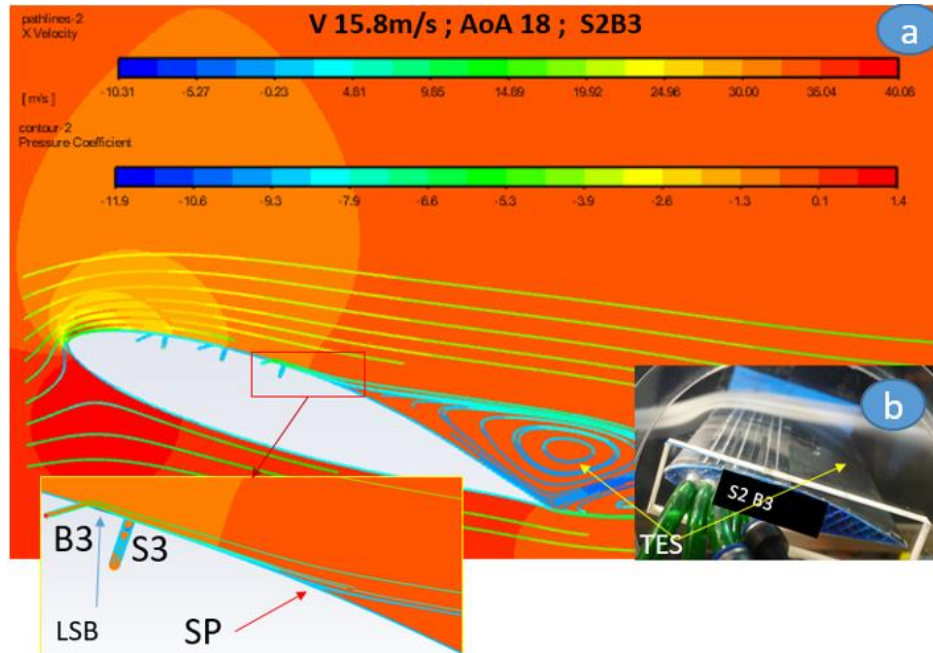
Figure C-1: Results with/without AFC for flow inlet speed 15.8 m/s and angle of attack 18°. flow visualisations around the aerofoil model for: (a) simulation, showing streamlines and pressure contours (b) experiment. (c) pressure coefficient (CP) distribution for both experimental and simulation results. (d) skin friction coefficient (C_f) results of the baseline case (with AFC S2B3)
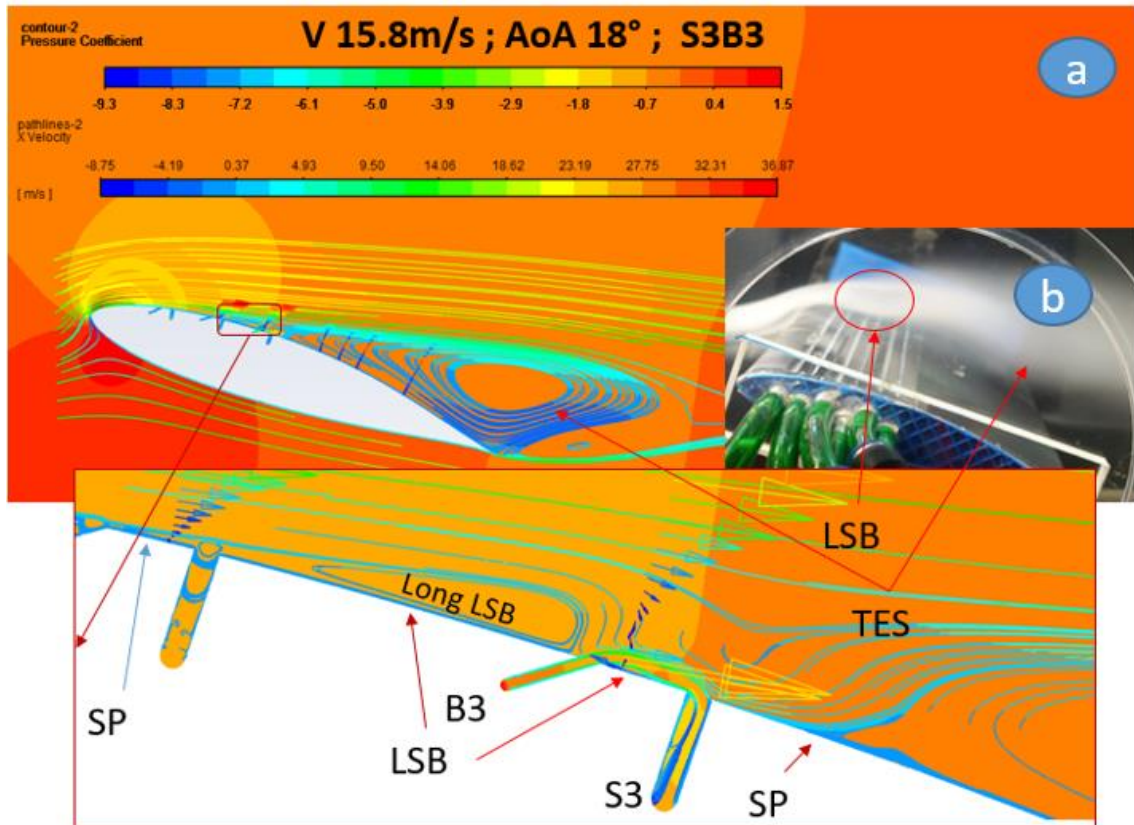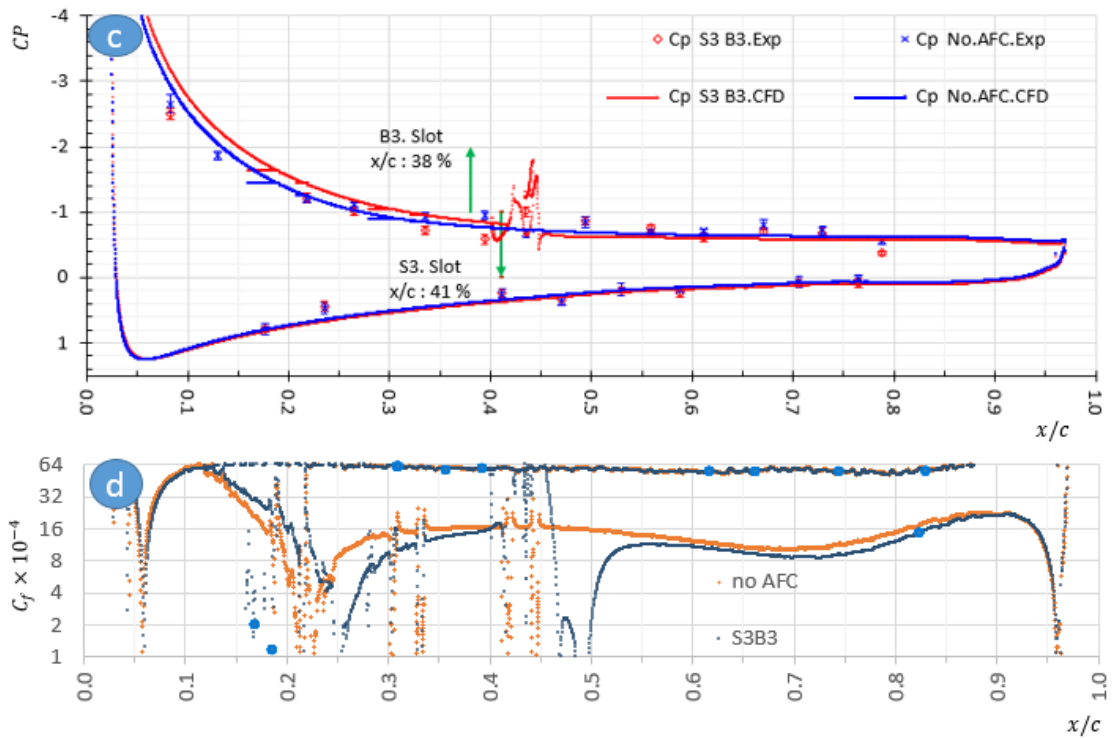
Figure C-2: Flow visualisations around the aerofoil model of AFC S1B3
as per Figure C-1
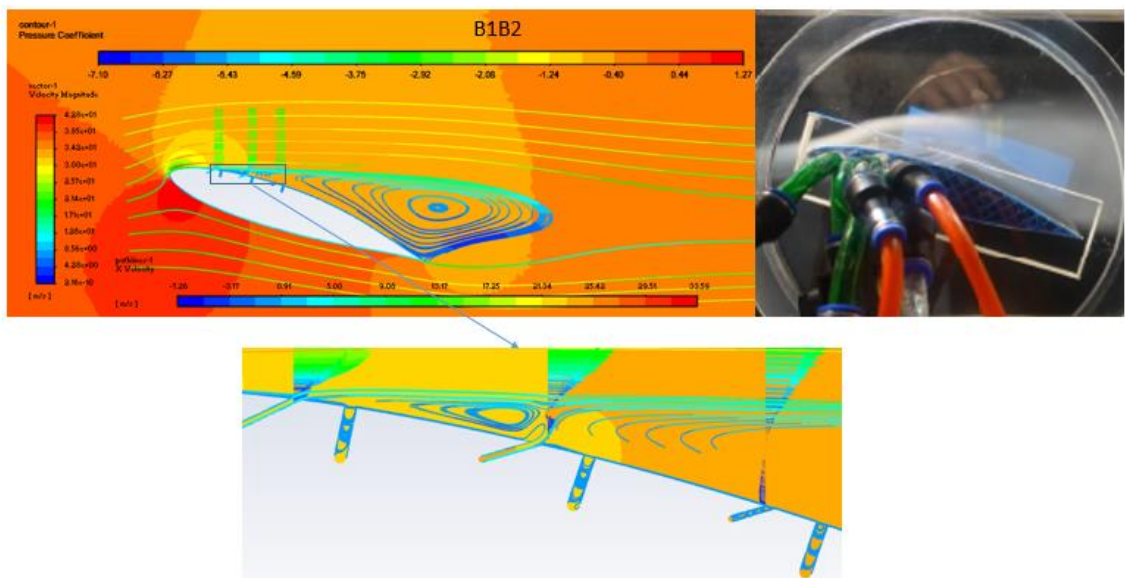
Figure C-3: Flow visualisations around the aerofoil model for simulation, showing streamlines and pressure contours, and experiment for AFC as a result of AFC B1B2 for flow inlet speed 15.8 m/s and angle of attack 18°.

Figure C-4: Flow visualisations around the aerofoil model of AFC B2B3 techniques
as per Figure C-3
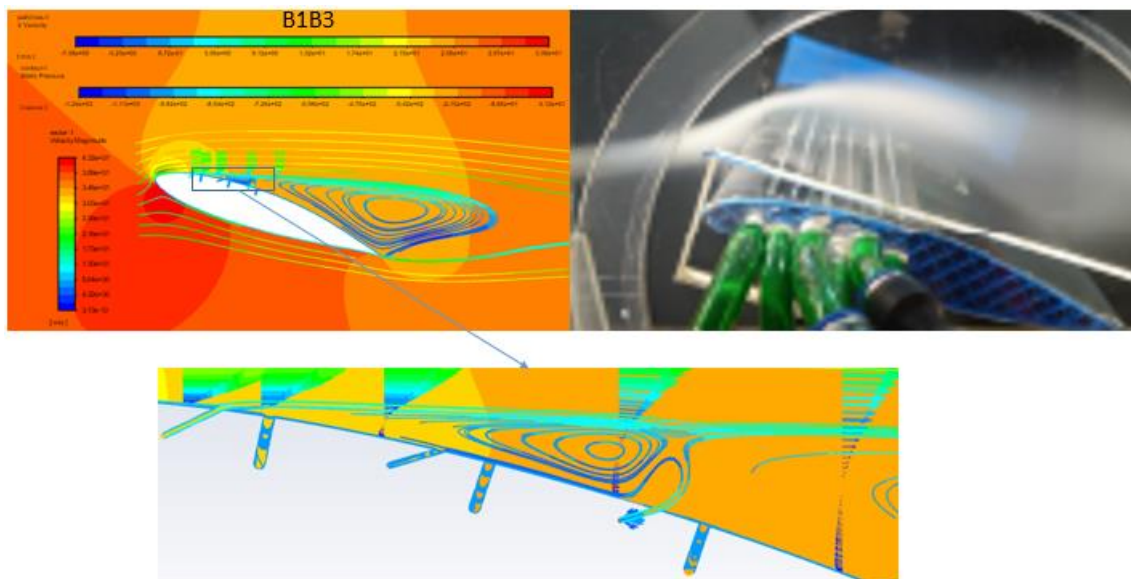
Figure C-5: Flow visualisations around the aerofoil model of AFC B1B3 techniques
as per Figure C-3
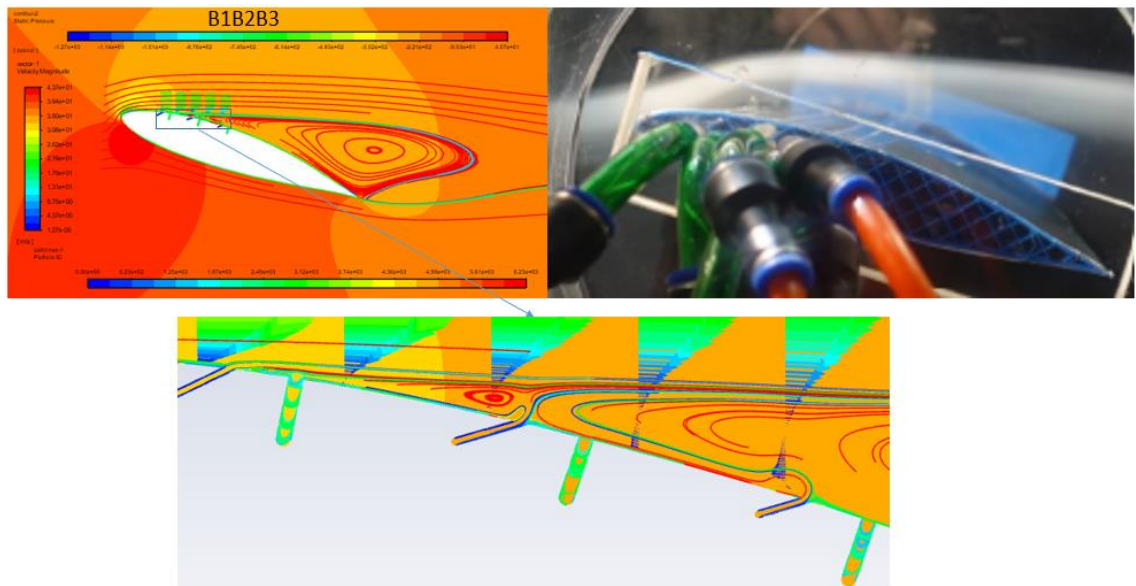
Figure C-6: Flow visualisations around the aerofoil model of AFC B1B2B3
techniques as per Figure C-3

Appendix D

D-1 Blade element and momentum theory

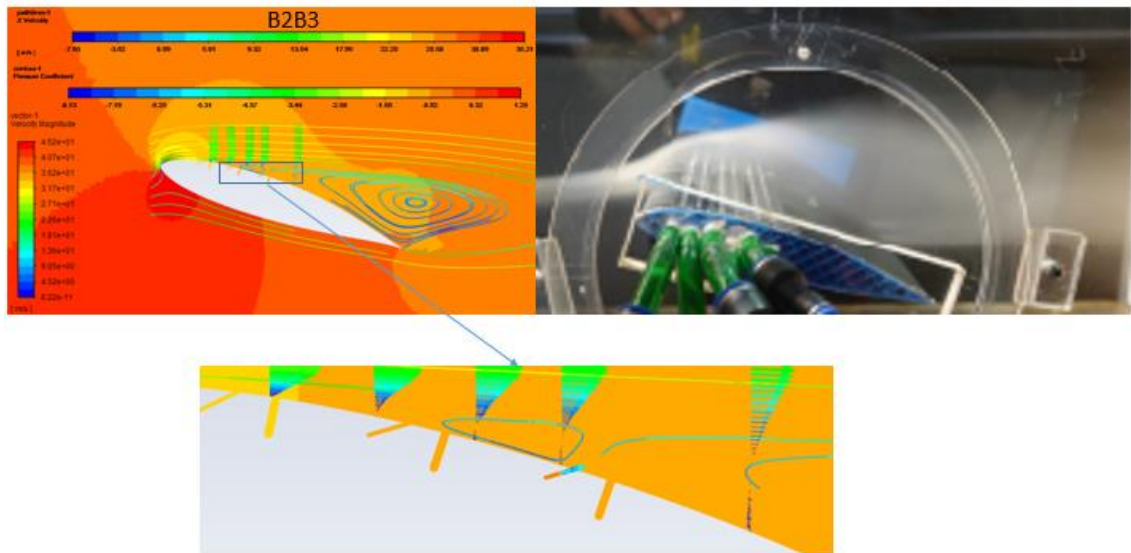Blade element and momentum is a combination of blade element theory (BET) and the momentum theory (Actuator disc theory) the details of which can be found in (Burton et al., 2011).

Blade Element Momentum (BEM) theory is widely used in wind turbine applications. Rankine initially examined the establishment of aerodynamic theories to predict wind turbine performance and then expanded by Froude using Actuator disk theory (Sun et al., 2016).

Two main factors are influencing the formation of aerodynamic forces. These are the distribution of pressure and the shear forces. Pressure forces act perpendicular to the surface, and shear forces affect with the surface tangentially.

According to blade element theory (BET), the wind turbine blade should be divided into several sections as a 2D aerofoil in order to predict the aerodynamic forces. So each section should be treated individually (Ali, 2014).

The blade root aerofoil profile requires a greater thickness (like S823 aerofoil) than the blade tip (like S822 aerofoil). A thinner aerofoil is required for the blade tip to mitigate drag and blade losses (Buhl, 2012).

The boundary layer slows down the flow, transferring momentum in the transverse direction, thus creating lift on each side of the aerofoil (Figure D-1). A net lift force is created because the curvature of the aerofoil causes greater momentum transfer on the upper side than on the lower side. There is a drag in the viscous flow (laminar or turbulent) because a boundary layer is created by the slowing of the flow, which creates a drag force. There is no drag force in the inviscid flow, but there is no lift force either. Designers strive to reduce drag force and increase the lift force to improve aerofoil performance. (Johnson, 2006).
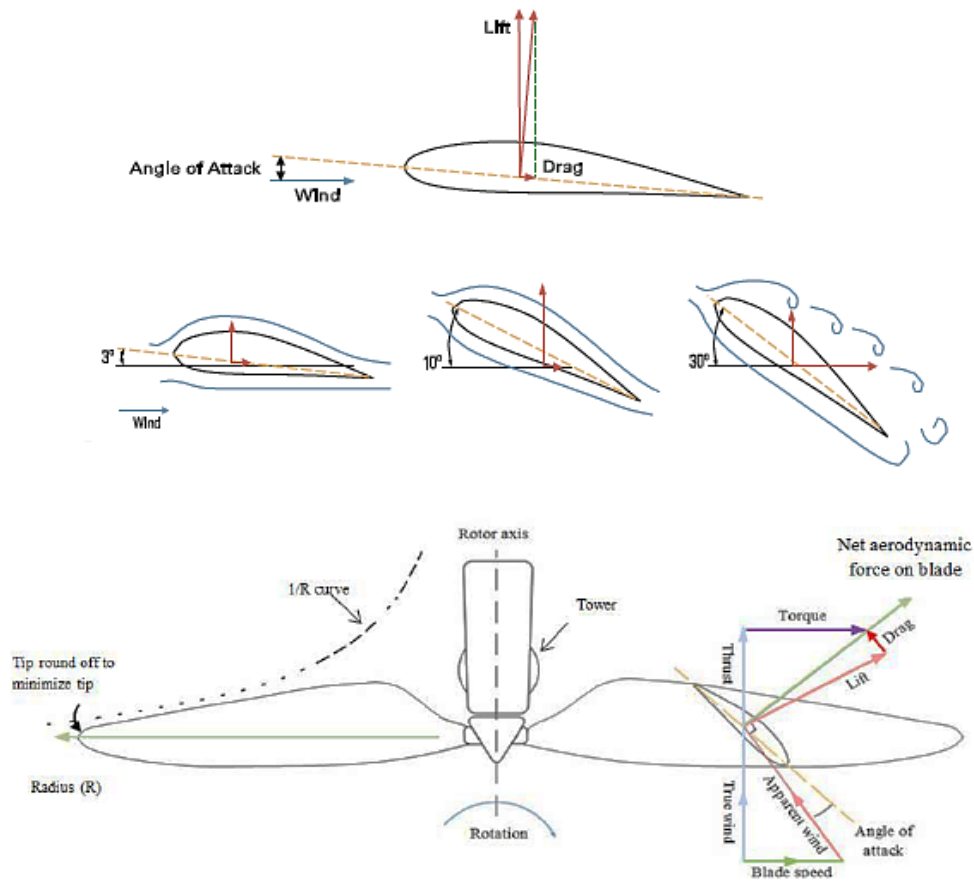
Figure D-1: The aerodynamic forces and angle of attack on a wind turbine blade.

Shkara (2014)

D-2 The velocity and force diagram acting on the aerofoil

The velocity and force diagram was established on the base of Blade Element Momentum theory. Figure D-2 shows the velocity and force diagram acting on the aerofoil. The lift force (L) is perpendicular to the relative wind direction (W), and the drag force is in the direction of the relative wind. So, the lift and drag forces are divided into two components, 'perpendicular' and 'parallel' to the undisturbed wind direction (V_1).

1) Velocity Diagram

Lift and drag coefficients are non-dimensional parameters. Those parameters vary with the velocity and angle of attack. Based on Figure D-2, there are two velocities; the first is in the direction of the undisturbed velocity, called the axial velocity (V_A), and the

second is perpendicular to it called the tangential velocity (V_T). Mathematically, these velocities can be expressed by:

$$V_A = V_1(1 - a) \dots\dots\dots\dots \text{D-1}$$

$$V_T = r\Omega(1 + a') \dots\dots\dots \text{D-2}$$

Where: a and a' are the axial and tangential induction factors respectively, and Ω is the
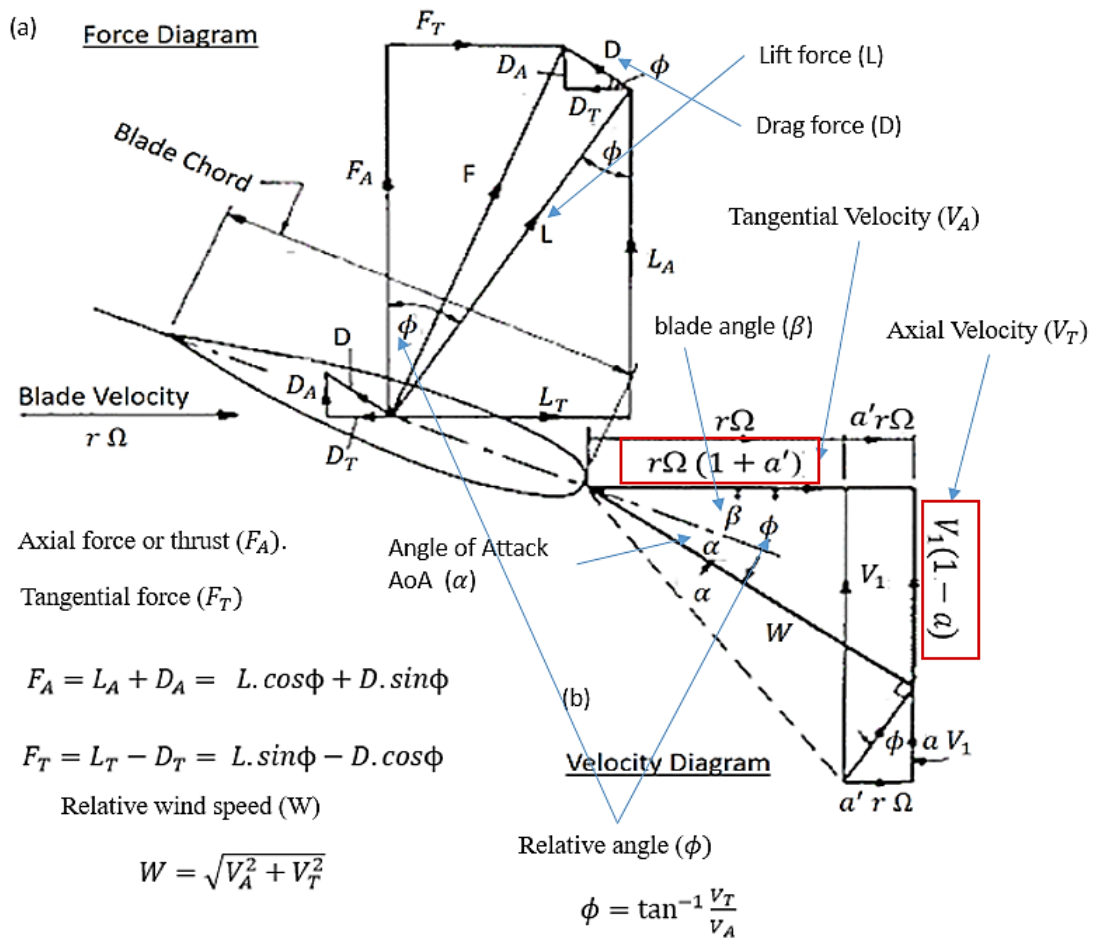
Figure D-2: The force and velocity diagram of the aerofoil (Shepherd, 1984)

The two velocities will then combine to produce relative wind speed (W) and the relative angle (ϕ) with the rotation plane (Shkara, 2014). So the relative wind velocity can be calculated as follows:

$$W = \sqrt{V_A^2 + V_T^2} \dots\dots\dots\dots \text{D-3}$$

144

The angle between the relative velocity vector (W) and the plane of rotation of the rotor is called the relative angle (ϕ) and can be expressed as:

$$\phi = \tan^{-1}\frac{V_T}{V_A} \ldots\ldots\ldots\ldots \text{D-4}$$

The angle between the chord line (the line connecting the leading edge and trailing edge of the aerofoil) and the plane of rotation is called the twits angle(β). It is a static angle. The angle between the chord line and relative wind speed is called the angle of attack(α). It is a dynamic angle. (Johnson, 2006).

The following formula can represent the relationship between these angles:

$$\phi = \alpha + \beta \ldots\ldots\ldots\ldots \text{D-5}$$

2) Force diagram

The vertical components of the lift (L_A) and drag (D_A) forces will unite to form the axial force or thrust (F_A). While the horizontal components ($L_T \ and \ D_T$) combine to form the tangential force (F_T) that causes torque this, in turn, causes the wind turbine to rotate. The thrust will be used by designers to ensure the construction of a wind turbine tower capable of withstanding those forces (Johnson (2006). The axial and tangential forces can be expressed as:

$$F_A = L_A + D_A = L.cos\phi + D.sin\phi \ldots\ldots\ldots \text{D-6}$$

$$F_T = L_T - D_T = L.sin\phi - D.cos\phi \qquad \ldots\ldots\ldots \text{D-7}$$

Both lift and drag forces depend on air density (ρ), the area (A) and the square of (V_1) in addition to lift and drag coefficients. So the lift and drag can be expressed as (Ali, 2014) :

$$L = 0.5 \ \rho \ V_1^2 A \ C_L \ldots\ldots\ldots\ldots \text{D-8}$$

$$D = 0.5 \ \rho \ V_1^2 A \ C_D \ldots\ldots\ldots\ldots \text{D-9}$$

Where: $C_L \ and \ C_D$ represent the lift and drag coefficients.

Appendix E

E-1 A computer program to predict wind turbine performance

A computer program was written in Matlab to predict the performance of low Reynolds number small horizontal axis wind turbine. The following parameters were found through this process:

The chord line and twist angle of the aerofoils versus normalised radius r/R were illustrated in Figure D-2.

The analysis of horizontal axis wind turbine performance can be performed through the combination of the momentum analysis (Blade momentum theory) of the rotor and the aerodynamic characteristics from blade element analysis (Blade Element Theory). Figure 2-11 shows both the axial and tangential forces and the velocity diagram. So the axial and tangential forces can be expressed as follows (Mahmood and Abbas, 2011):

From momentum analysis or BMT:

Axial force, $dF_{A,mom} = 4\pi\rho V_1^2(1-a)a\, r\, dr$ ----------------------- D-1

Torque, $dQ_{,mom} = 4\pi\rho V_1\Omega(1-a)a'r^3 dr$ ---------------------- D-2

And from blade element analysis:

Axial force,

$dF_{A,bl} = 0.5\,\rho W^2 C_A\, C\, B\, dr$ ---------------------- D-3

Torque,

$dQ_{,bl} = 0.5\,\rho W^2 C_T r\, C\, B\, dr$ ---------------------- D-4

The rotor solidity $\sigma = \dfrac{BC}{2\pi r}$ ------------------------- D-5

E-2 Blade parameters

In order to determine the blade parameters, a chord line (the line in the aerofoil between the leading and trailing edges), and a twist angle (the angle between the plane rotation and chord line), must be calculated along the length of the blade. So several parameters should be prepared as input data as follows (Figure E-1-a). The rated wind speed (V_r) is the speed at which the maximum power of the wind turbine used is achieved; the number of rotor blades (B); rotor Radius (R); design tip speed ratio (λ_d); the optimal angle of attack (α_{opt}), which is the angle at which the lift-to-drag rate is as high as possible; design Lift Coefficient (C_{Ld}) which is the value of lift coefficient at the optimum angle of attack; and Kinematic Viscosity (v). Moreover, for each blade's section, the following parameters (Mahmood and Abbas, 2011) should be calculated:

Local design TSR $\lambda_{rd} = \lambda_d * \dfrac{r}{R}$ ---------------------- D-6

Design Relative angle $\phi_d = \dfrac{2}{3}\tan^{-1}\dfrac{1}{\lambda_{rd}}$ ---------------------- D-7

Blade Twist angle $\beta = \phi_d - \alpha_{opt}$ ---------------------- D-8

Blade Chord $C = 8.\,\pi.\,r.\dfrac{(1-\cos(\phi))}{B.\,C_{LD}}$ ---------------------- D-9

The angle of attack of the aerofoil profile has been changed substantially from degree to degree and to cover all possibilities of attack angles, as shown in Figure E-1-b. So it was required to determine the Induction factors (a and a'). The iteration process was implemented regarding those factors. The steps of this process were illustrated in Figure E-1-c. According to Table 1-1 in Chapter one; the blade was divided into two parts. The NERL S823 aerofoil was used for the first experiment, which was represented in the blade from root to mid-blade while the second section was represented from mid-blade to tip for the NREL S822 aerofoil.

E-3 The process to establish the power coefficient

In Figure E-1-b, the angle of attack (α) is varied systematically, from degree to degree for both the NREL S822 and NREL S823 aerofoils. Also, the axial and tangential

interference factors and a' calculations were implemented. In the iteration process that intends to find the axial and tangential factors (a and a'), the initial values of (a and a') were defined as (0 and 0.01), respectively (Shkara, 2014).

The following steps are followed sequentially to calculate the thrust and tangential coefficients C$_A$ and C$_T$ (Bavanish and Thyagarajan, 2013):

The thrust coefficients $C_A = C_L cos\phi + C_D sin\phi$ ------------------ D-10

The tangential coefficient $C_T = C_L sin\phi - C_D cos\phi$ ------------------ D-11

By pairing equations (3-1) with (3-3) and equations (3-2) with (3-4), the axial and tangential factors can be calculated respectively (Le GouriÉRÈS, 1982, Le Gourieres, 1982). So,

Axial induction factor(a): $G = \dfrac{a}{1+a} = \dfrac{C_A \sigma}{4 \sin^2 \phi}$ ------------------ D-12

Tangential induction factor (a'): $E = \dfrac{a'}{1+a'} = \dfrac{C_T \sigma}{4 \sin \phi cos\phi}$ ------------------ D-13

According to Figure 2-11 in Chapter 2, the following two equations can be derived as illustrated in Figure E-1-c.

So, to calculate the relative velocity: $W = \dfrac{V_1(1-a)}{sin\phi}$ ------------------ D-14

Calculate Tip speed ratio: TSR (λ) from $cot\phi = \lambda \dfrac{r}{R} \dfrac{(1+a')}{(1-a)}$ ------------------ D-15

Reynolds number (Re) can be expressed as $Re = \dfrac{WC}{\nu}$ ------------------ D-16

The torque coefficient can be derived from the following equation:

$$C_q = \frac{Q}{0.5\, \rho\, A\, V^2 R}$$ ------------------ D-17

By conducting integration on equation 3-1 and considering equation 3-17, we can get:

$$C_q = \int_0^1 8\lambda_r a'(1-a)\left(\frac{r}{R}\right)^2 d\frac{r}{R}$$ ---------------- D-18

Now from equations 3-13 and 3-15,

$$C_q = 8 \int_0^1 (1-a)^2 \, E \, cot(\phi) \left(\frac{r}{R}\right)^2 d\frac{r}{R} \qquad \text{--------------- D-19}$$

So, the local torque coefficient (m_r) from:

$$m_r = 4(1-a)^2 E \left(\frac{r}{R}\right)^2 cot\phi \qquad \text{--------------- D-20}$$

The pressure difference between suction (upper) and pressure (lower) surfaces of the aerofoil causes the flow to move from the high-pressure zone to the low-pressure zone. This leads to the generation of swirls in the blade's tip area which subsequently turns into a wake, causing a loss in wind turbine power output (Ali, 2014) (Sun et al., 2016). Rohrbach, Worobel, Goldstein and Prandtl studied the reduction of efficiency of the wind turbine. So The Prandtl relation can be expressed as Le GouriÉRÈS (1982) :(Darwish et al., 2019)
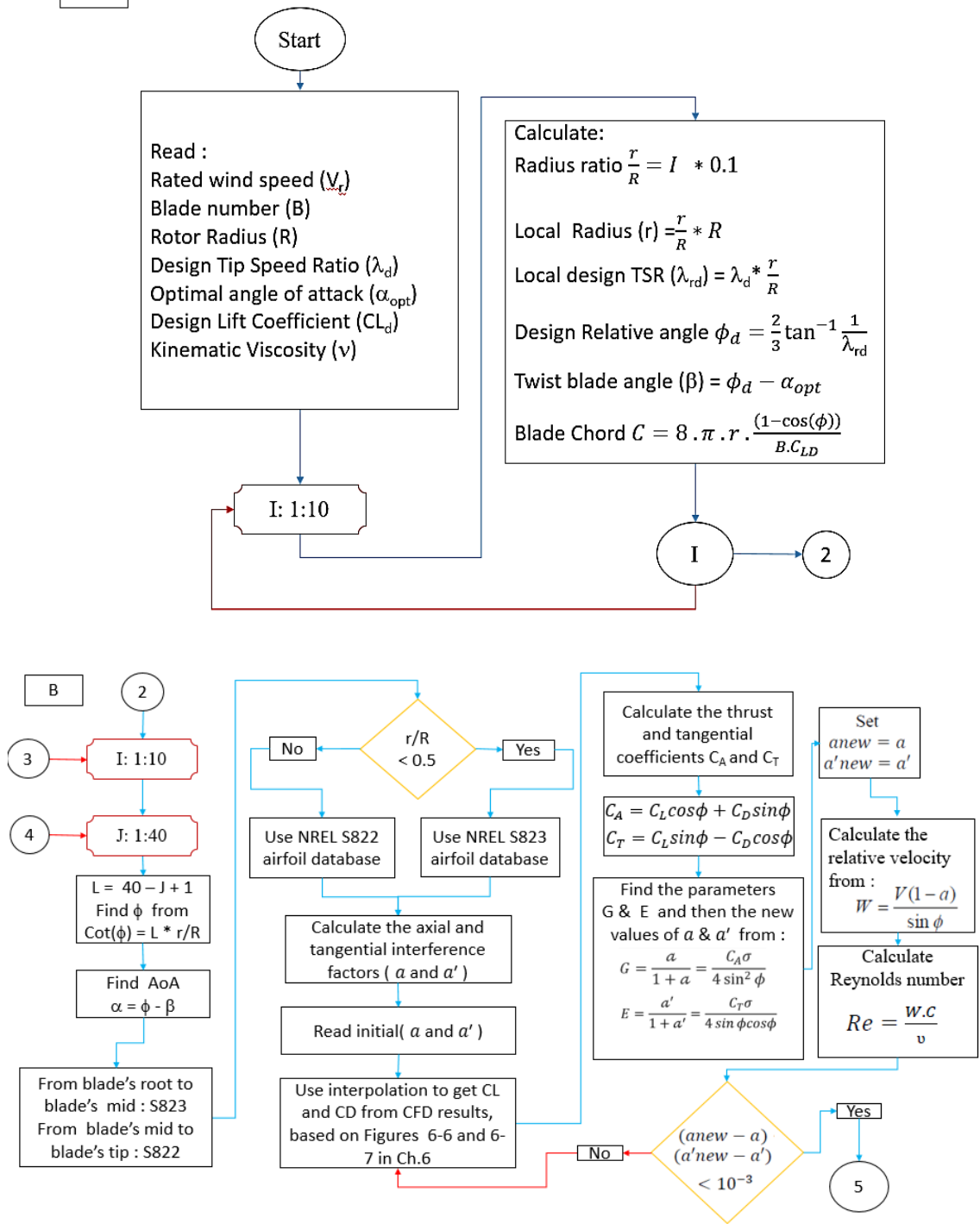
$$\eta_b = \left(1 - \frac{0.93}{B\sqrt{\lambda^2+0.445}}\right)^2 \qquad \text{--------------- D-21}$$

Calculate torque coefficient C_q from: $C_q = 2 \int_0^1 m_r \eta_b d\frac{r}{R}$ \qquad -------- D-22

Calculate power coefficient C_p from: $C_p = C_q.\lambda$ \qquad --------------- D-23

a	HAWT performance prediction (power coefficient C_P)

Start

Read :
Rated wind speed (V_r)
Blade number (B)
Rotor Radius (R)
Design Tip Speed Ratio (λ_d)
Optimal angle of attack (α_{opt})
Design Lift Coefficient (CL_d)
Kinematic Viscosity (ν)

Calculate:
Radius ratio $\frac{r}{R} = I * 0.1$

Local Radius (r) $= \frac{r}{R} * R$

Local design TSR (λ_{rd}) $= \lambda_d * \frac{r}{R}$

Design Relative angle $\phi_d = \frac{2}{3}\tan^{-1}\frac{1}{\lambda_{rd}}$

Twist blade angle (β) $= \phi_d - \alpha_{opt}$

Blade Chord $C = 8.\pi.r.\frac{(1-\cos(\phi))}{B.C_{LD}}$

I: 1:10

I → 2

| B | 2 |

3 → I: 1:10

4 → J: 1:40

L = 40 − J + 1
Find ϕ from
$\cot(\phi) = L * r/R$

Find AoA
$\alpha = \phi - \beta$

From blade's root to
blade's mid : S823
From blade's mid to
blade's tip : S822

r/R < 0.5 — No / Yes

Use NREL S822 airfoil database

Use NREL S823 airfoil database

Calculate the axial and tangential interference factors (a and a')

Read initial(a and a')

Use interpolation to get CL and CD from CFD results, based on Figures 6-6 and 6-7 in Ch.6

Calculate the thrust and tangential coefficients C_A and C_T

$C_A = C_L\cos\phi + C_D\sin\phi$
$C_T = C_L\sin\phi - C_D\cos\phi$

Find the parameters G & E and then the new values of a & a' from :

$G = \frac{a}{1+a} = \frac{C_A\sigma}{4\sin^2\phi}$

$E = \frac{a'}{1+a'} = \frac{C_T\sigma}{4\sin\phi\cos\phi}$

Set
$anew = a$
$a'new = a'$

Calculate the relative velocity from :
$W = \frac{V(1-a)}{\sin\phi}$

Calculate Reynolds number
$Re = \frac{w.c}{\upsilon}$

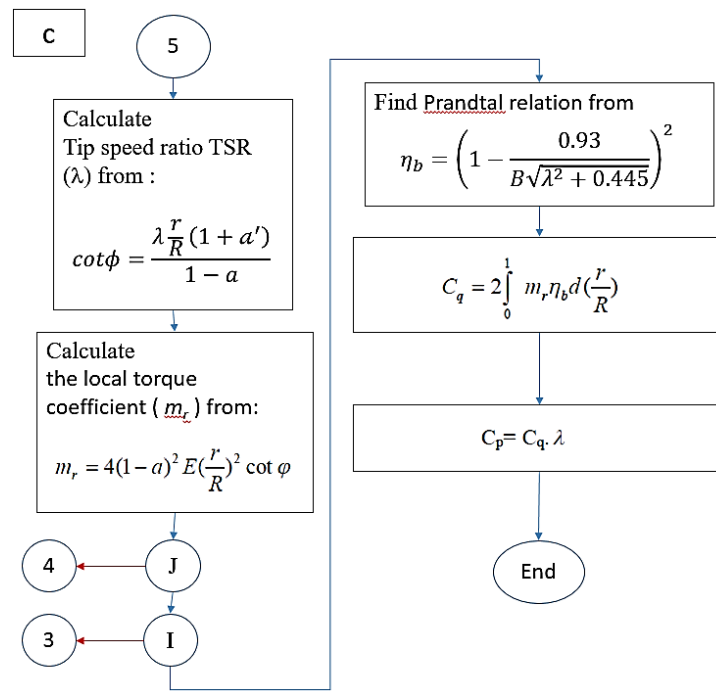$\frac{(anew - a)}{(a'new - a')} < 10^{-3}$ — No / Yes

5

150

Figure E-1: Flow chart for wind turbine performance prediction

Appendix F

F-1   The selected wind turbine specifications

The selected actual wind turbine power was represented in Figure F-1. The information of the selected wind turbine has a rated wind speed (Vr) of 12 m/s and rotor Radius (R) of 5m.

Technical information

POWER		Unit
1) Rated power	25	kW
2) Rated wind speed	12	m/s
3) Cut-in wind speed	3	m/s
4) Cut-out wind speed	None	m/s
5) Maximum wind speed the turbine can withstand	216	Km/h
DIMENSIONS		
6) Rotor weight (+ generator)	620	kg
7) Rotor diameter	10	m
8) Rotor height (for VAWT only)		m
9) Swept area	78,6	m²
10) Height of the mast	18/24/32	m
OTHER INFORMATION		
11) Maximum rpm	140	At rated wind speed
12) Gear box type	none – direct drive	
13) Brake system	Optional remote control (blades stalling)	
14) Number of blades	2	
15) Blades material	Composite fiber glass	
16) Output voltage	400	V
17) Minimum operation temperature	- 40	°C
18) Maximum operation temperature	+ 50	°C
19) Acoustic levels at a distance of 20 m ? at nacelle ? (wind = 5 m/s)	65	DB
20) Lifetime	25	Years
21) Is the machine self-starting	Yes	
22) Use of an asynchronous generator	No	
23) Yaw control system	Wind vane	
24) Upwind or downwind	Upwind turbine	

Calculated power curve

Wind speed (m/s)	Power (kW)
1	0
2	0
3	0.5
4	1
5	2
6	3.5
7	5.5
8	8.2
9	11.7
10	16
11	21
12	25
13	25
14	25
15	25

Power curve:

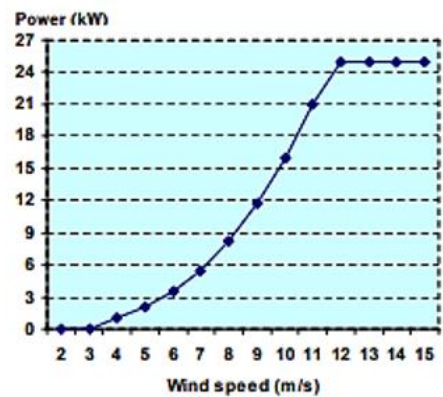

Figure F-1: data from the actual small HAWT used in this project

Appendix G

G-1 Changing parameters design of wind turbine rotor

In Table G-1, the design parameters to investigate the power coefficient were listed.

Table G-1: The design parameters to investigate the power coefficient

Design tip speed ratio λ_d	Reynolds number (Re)	Number of Blades (B)	Figure's numbering of Figure G-1
6.1	Re 1.83E+05	2	a

		3	b
	Re 5.14E+05	2	c
		3	d
4.9	Re 1.83E+05	2	e
		3	f
	Re 5.14E+05	2	g
		3	h

In general, when a wind turbine utilises three blades, it performs more efficiently than with two blades. There is an improvement in the performance of the turbine as a result of using three blades. IF the improvement is only slight, this will then increase the manufacturing costs of the wind turbine and the maintenance procedures. Having said that, if the goal is solely to improve turbine performance at any cost, then three blades are preferable. Nevertheless, when the goal is purely economic benefit, then running the turbine with two blades would be preferable. In engineering and technical terms, two blades are better than three.

At low Re, (Figure G-1-a and Figure G-1-b), the improvement in turbine performance is evident, but after $= 8$, the power coefficient value is lower than the base case. However, at high Re (Figure G-1-c and Figure G-1-d), although there was no significant improvement, it did not drop below the baseline.
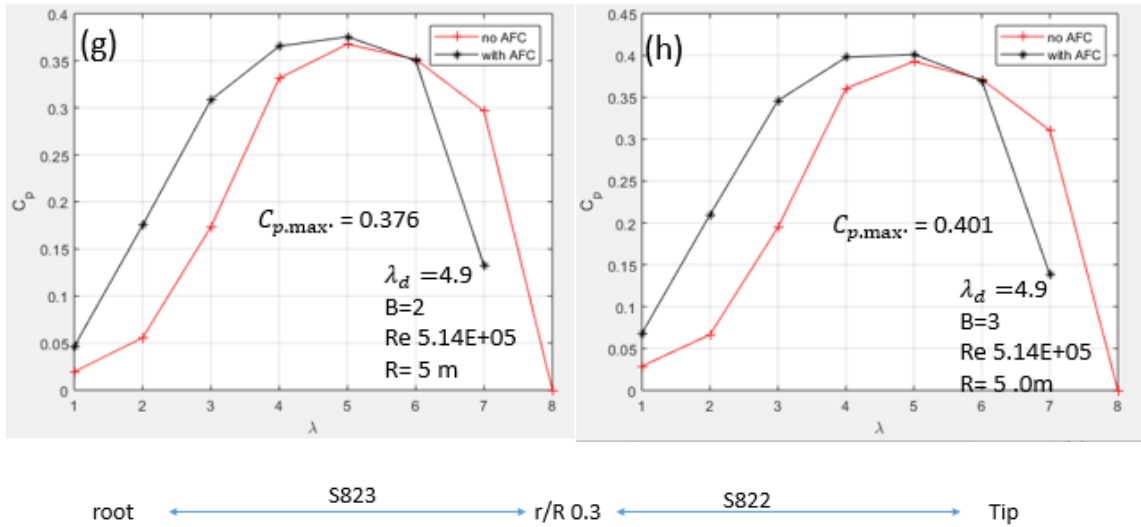
155
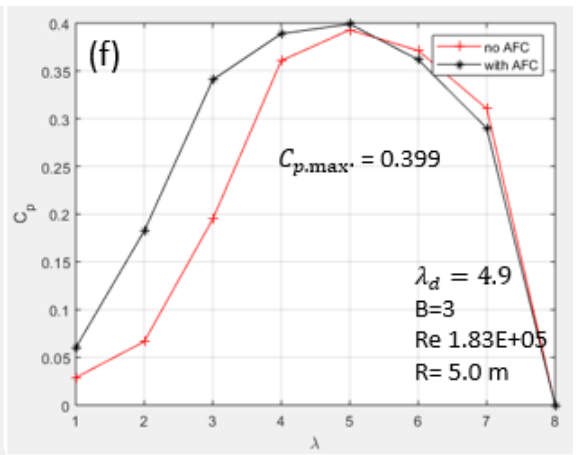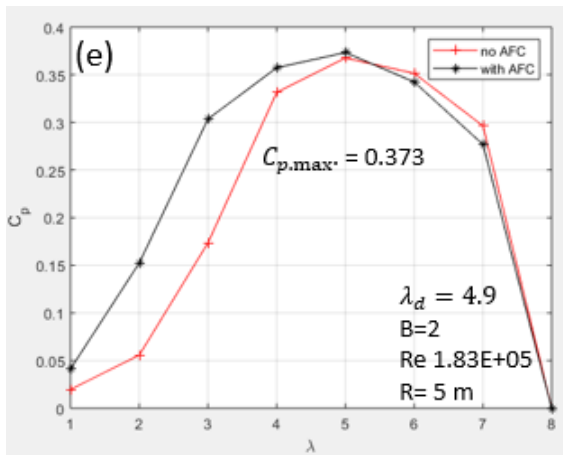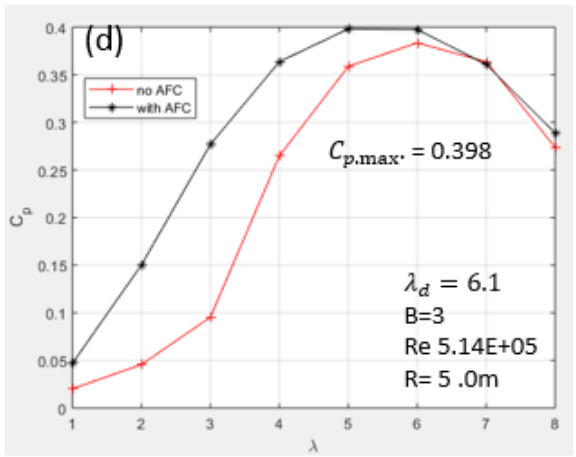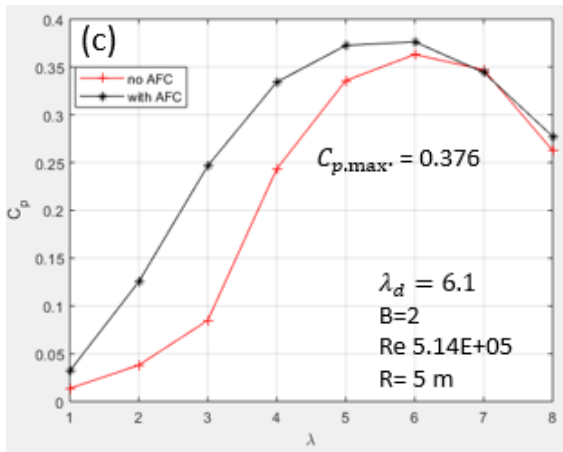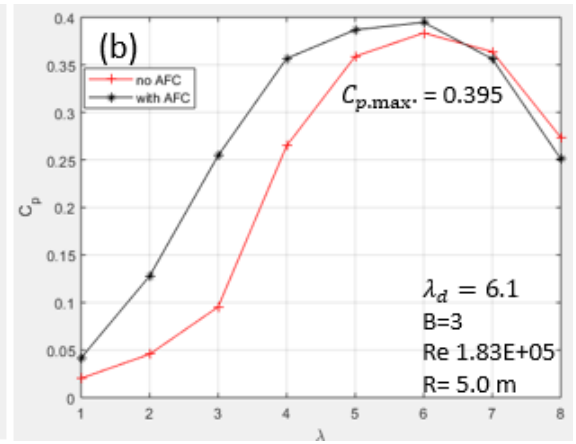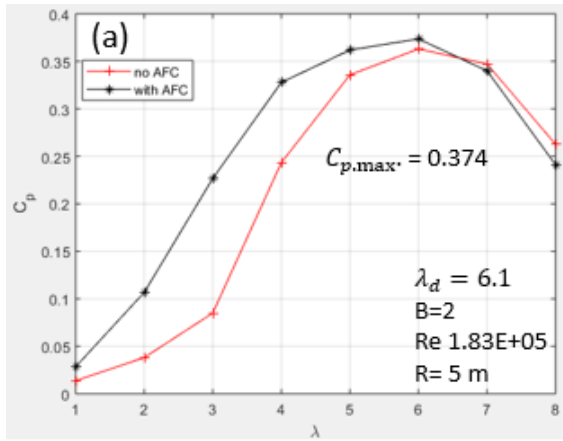
Figure G-1: The power coefficient with/without the AFC for Reynolds numbers 1.83E+05 and 5.14E+05, when design tip speed ratios equal to 6.1 and 4.9 and when the number of blades is 2 and 3.

The maximum power coefficients with AFC are represented in Figure G-2. Despite additional design and installation costs, the performance of a wind turbine with three blades exceeds that of a wind turbine with two blades. Moreover, the use of design tip ratio with a value of 4.9 provides acceptable results compared with the case of 6.1. In the case of Figure G-2-d and Figure G-2-h, the maximum power coefficients with AFC are the same (0.4), but without AFC, Figure G-2-h is preferable because a vacuum pump for suction will be required. Therefore, these additional costs need to be considered in finding the annual energy production.
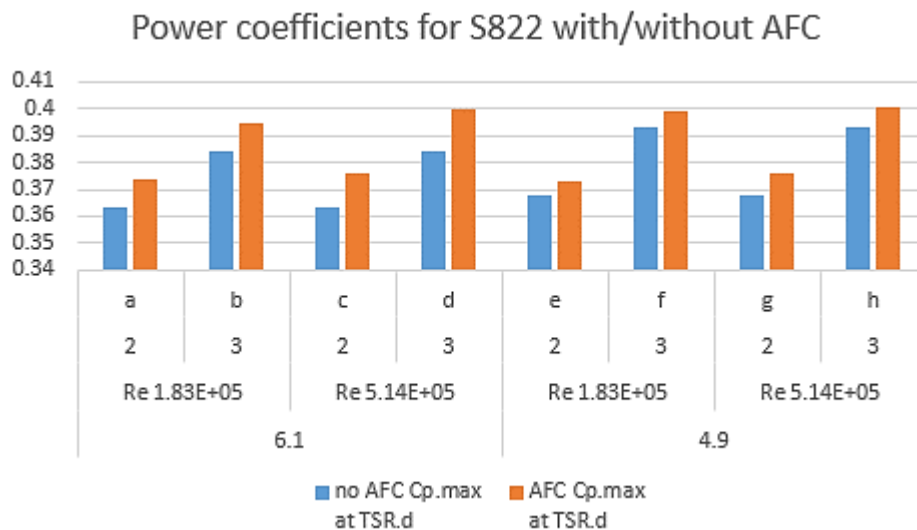
Figure G-2: The maximum power coefficients before/after AFC (S1) with their improvement percentages for two/three blades, lowest/highest tested Reynolds number, and design tip speed ratio of 4.5 and 6.1.

So, for the selected best case, the maximum power coefficient for the wind turbine after conducting AFC was 0.388 and 0.401 for tested Reynolds numbers. The output power versus the blade rotational speed for multi-available wind speed and tested Reynolds numbers were shown in Figure G-3
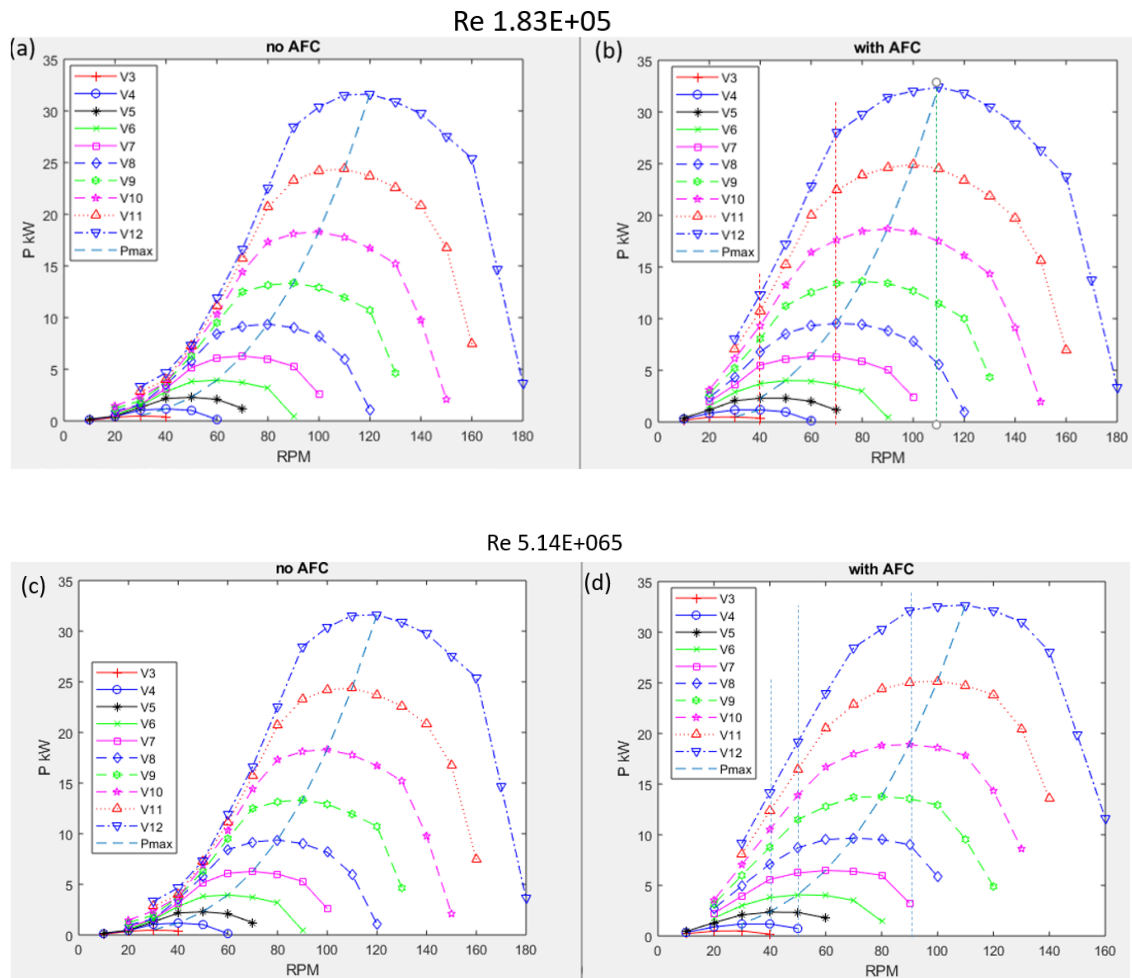

Figure G-3: Wind turbine power without (a and c) and with (b and d) AFC versus rotational blade speed with multi wind speeds; the vertical dashed lines represent selected blade rotational speeds; the dashed curve marked 'Pmax' represents the maximum power at any wind speed.

Appendix H

H-1 Weibull distribution

Weibull distribution is best suited to describe the probability of wind speed being available, and it is imperative to determine the power factor (Darwish et al., 2019). Two parameters, the shape (K_w) and scale (C_w m/s), characterize the Weibull distribution (Johnson, 2006). These parameters are essential for selecting locations for wind turbine installation. Besides, they give a good description of the probability of availability of annual wind speeds. Shape and scale parameters for selected regions in Australia were represented in Figure H-1. These values were used to find the Capacity Factor (CF) for the operation of the wind turbine in the selected sites.

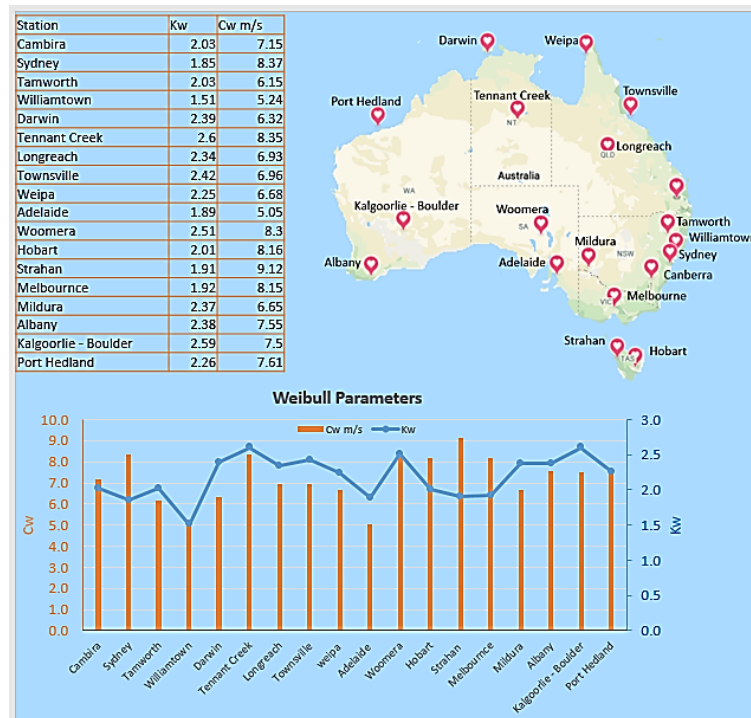| Station	Kw	Cw m/s
Cambira	2.03	7.15
Sydney	1.85	8.37
Tamworth	2.03	6.15
Williamtown	1.51	5.24
Darwin	2.39	6.32
Tennant Creek	2.6	8.35
Longreach	2.34	6.93
Townsville	2.42	6.96
Weipa	2.25	6.68
Adelaide	1.89	5.05
Woomera	2.51	8.3
Hobart	2.01	8.16
Strahan	1.91	9.12
Melbournce	1.92	8.15
Mildura	2.37	6.65
Albany	2.38	7.55
Kalgoorlie - Boulder	2.59	7.5
Port Hedland	2.26	7.61

Figure H-1: The Weibull Parameter values for multi-sites around Australia.

H-2 Mean wind speed for regions in Australia

Mean wind speed is the average available wind speed in a region. According to the Bureau of Meteorology (BOM) wind speed availability data (Table H-1), the mean speeds for several regions in Australia were used in the calculation of capacity factor. The mean wind speeds in Australia (Figure H-2) range from 4 m/s to 8 m/s. There are

some regions with lower wind speeds than this, where the mean speed in between two regions lies between 4 and 5.5 m/s.

Table H-1: Mean wind speeds and Weibull parameters for sites in Australia (BOM). Where, V_{mean} is the mean wind speed; k_w is the shape parameter and C_w is the scale parameter.

Station	V_{mean}* (m/s)	Weibull Parameters*	
		K_w	C_w (m/s)
Canberra [1]	6.2	2.03	7.15
Sydney [2]	7.5	1.85	8.37
Tamworth [2]	5.32	2.03	6.15
Williamstown [2]	4.7	1.51	5.24
Darwin [3]	5.5	2.39	6.32
Tennant Creek [3]	7.3	2.60	8.35
Longreach [4]	6.01	2.34	6.93
Townsville [4]	6	2.42	6.96
Weipa [4]	5.81	2.25	6.68
Adelaide [5]	4.3	1.89	5.05
Woomera [5]	7.3	2.51	8.30

Hobart [6]	7.1	2.01	8.16
Strahan [6]	8	1.91	9.12
Melbourne [7]	7.1	1.91	8.15
Mildura [7]	5.8	2.37	6.65
Albany [8]	6.6	2.38	7.55
Kalgoorlie – Boulder [8]	6.6	2.59	7.50
Port Hedland [8]	6.6	2.26	7.61

[1]Capital of Australia ; [2]City in New South Wales; [3]City in Northern Territory; [4] City in Queensland;

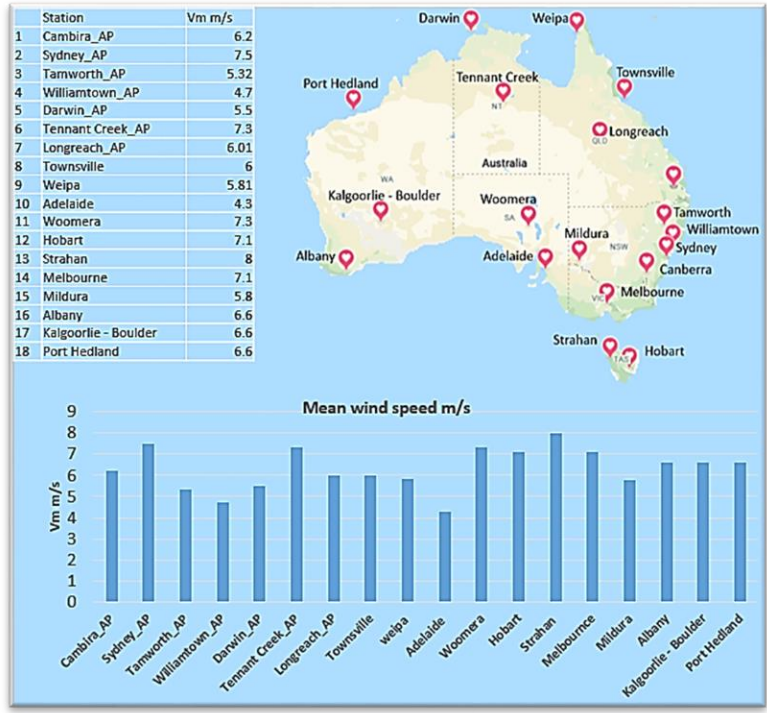[5] City in South Australia; [6] City in Tasmania; [7]City in Victoria; [8]City in Western Australia.

Figure H-2: The mean wind speed for multi-sites around Australia

H-3 Capacity Factor and annual energy production
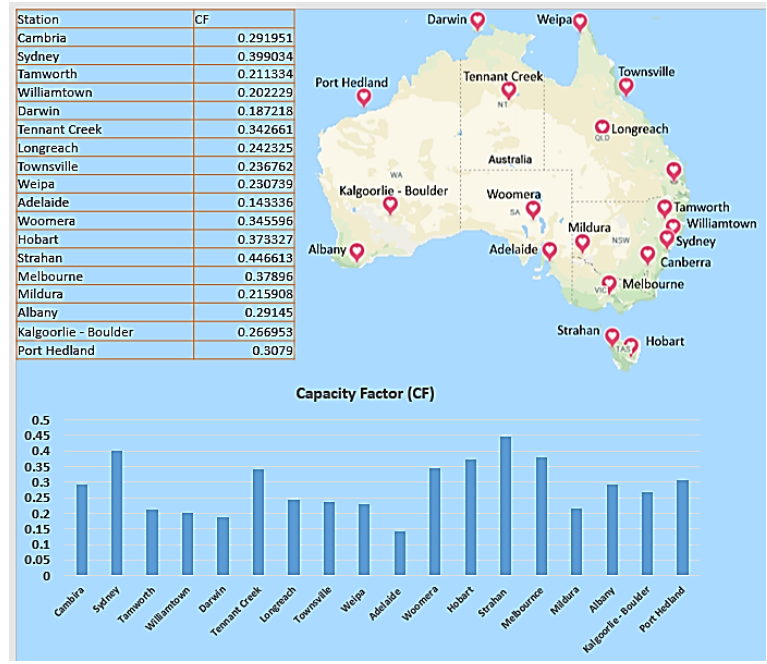
The values of CF were presented in Figure H-3

Figure H-3: The capacity factor (CF) for low wind speed sites around Australia.

161

LIST OF PUBLICATIONS

1 DARWISH, A. S., SHAABAN, S., MARSILLAC, E. & MAHMOOD, N. M., 2019. A methodology for improving wind energy production in low wind speed regions, with a case study application in Iraq. Computers & Industrial Engineering, 127, 89-102.

2 Nazar Aldabash[1], Dr Andrew Wandel[1], Prof Abdul Salam Darwish[2], Dr Jayantha Epaarachchi[1], 2021, Numerical and experimental investigation of the Flow Separation over NREL's S822 Aerofoil and its Control by Suction and Blowing, *Renewable Energy and Environmental Sustainability . 6,5(2021)*

3 Nazar Aldabash[1], Dr Andrew Wandel[1], Prof Abdul Salam Darwish[2], Dr Jayantha Epaarachchi[1], 2020, The effect of boundary layer separation on aerodynamic characteristics of a small WT blade aerofoil section, *Renewable Energy and Environmental Sustainability. (Under preparation)*

4 Nazar Aldabash[1], Dr Mohammed Khudair Abbas[2], Prof Abdul Salam Darwish[3], Dr Jayantha Epaarachchi[1], Andrew Wandel[1], *2020,* Numerical prediction method for the horizontal axis wind turbine-developed theoretical approach., *Renewable Energy and Environmental Sustainability. (Under preparation)*

5 Nazar Aldabash[1], Dr Ahmed Razzaq Hasan Al-Manea[2], Dr Andrew Wandel[1], Dr Jayantha Epaarachchi[1], Prof Abdul Salam Darwish[3], 2020, Study the influence of suction and blowing techniques velocity on airfoil performance, *Renewable Energy and Environmental Sustainability. (Under preparation)*